NONLINEAR ACCELERATION SENSITIVITY AND FREQUENCY TEMPERATURE BEHAVIOR OF QUARTZ CRYSTALS

By

JIAN FENG CHEN

A Dissertation submitted to the

Graduate School – New Brunswick

Rutgers, The State University of New Jersey

In partial fulfillment of the requirements

For the degree of

Doctor of Philosophy

Graduate Program in Civil and Environmental Engineering

Written under the direction of

Yook-Kong Yong

And approved by

____

____

____

____

New Brunswick, New Jersey

October 2016

ABSTRACT OF THE DISSERTATION

Nonlinear Acceleration Sensitivity and Frequency

Temperature Behavior of Quartz Crystal

By JIAN FENG CHEN

Dissertation Director: Yook-Kong Yong

Quartz, composted of Silicon and Oxygen (Silicon Dioxide SiO_2), has been the material of choice for stable resonators in wide applications of modern electronics. Due to decrease in the size of modern electronic devices, the nonlinearities of piezoelectric materials become more pronounced. Extensive study of the nonlinear behaviors of piezoelectric material is required. Three dimensional FEM modes are developed to calculate the effect of nonlinearities on the thickness shear mode resonant frequency. The intrinsic nonlinearities affecting the quartz resonators at high frequencies are acceleration sensitivity, force-frequency effect, and frequency-temperature behavior.

A detailed study of the acceleration sensitivity of a rectangular *AT*-cut quartz plate is presented. For *AT*-cut quartz resonators with the crystal digonal *X*-axis perpendicular to plate *X*-axis, the in-plane acceleration sensitivity is found to be negligible compared to the out-of-plane (*Y*-axis) acceleration sensitivity. When the crystal digonal *X*-axis is parallel to plate *X*-axis, the *Y*-axis acceleration sensitivity is rectified. A DC bias field with an appropriate DC voltage could potentially yield a reduction of acceleration sensitivity in *Y*-axis direction of about two orders of magnitude.

The behaviors of vibrating crystal plates under the action of external forces in fundamental mode and third overtone mode are studied. The plates were respectively

subjected to diametrical compression forces and flexural bending in different configurations. Finite element models were developed using theory of small deformation superposed on finite initial deformation in Lagrangian formulation. The model results showed consistent trend with the experimental results by Fletcher and Mingins et al.

The electrode stresses can be used to improve the frequency-temperature (f-T) behavior of ultra-high frequency (UHF) quartz resonators. The use of chromium-aluminum electrodes yields improved f-T behavior compared to the case where aluminum electrodes are used alone. The UHF quartz resonators must be treated as composite plates of quartz and electrode film since the ratio of electrode thickness to quartz plate thickness is significant. The quartz-aluminum composite plate rotates the f-T curve clockwise while the quartz-chromium composite plate rotates the f-T curve counter-clockwise.

Dedication

I dedicated this dissertation to my parents ***Xiucong Chen,Qiufang Dong***

and my lovely wife ***Laina Yeung*** *for their constant support and unconditional love.*

I love you all dearly.

Acknowledgements

This dissertation could never be accomplished without help and supports from my family and friends. First, I would like to express my sincere appreciation to my advisor Dr. Yook-Kong Yong for his constant guidance throughout my doctoral studies. His passion for truth and rigorous attitude motivated me in both academic and personal aspects of my life. I would also like to express my gratitude to my committee members Dr. Perumalsamy N. Balaguru, Dr. Mitsunori Denda, and Dr. Husam Najm for their valuable advises and encouragement throughout my research and their valuable times in reviewing this dissertation.

My appreciation goes to my lab mates Gobong Choi and Xiangnan Pang, for always listening and giving me words of encouragement when I needed them. I would also like to give my appreciation to my friends Guangji Xu, Jiaqi Chen, Alaa Ali, Han Sun, Jiandong Meng, and Sunny Wong for their encouragement and mental supports during my doctoral studies.

Most importantly, I would like to thank my parents Xiucong Chen, my dad and Qiufang Dong my mom, whom have sacrificed their lives for me and my sister Xia Chen and provided unconditional love and care for both of us. I would not have made this far without them. Thank you all for your earnest encouragement and devoted supports.

Lastly, I want to devote my appreciation to my lovely wife, Laina Yeung. Thank you for you sacrifices, love and encouragement. It is nearly impossible for me to complete this research work without your accompany.

Table of Contents

List of Tables

List of Figures

Chapter 1 Introduction

1.1 Classification of Acoustic Waves and Devices

A wave can be described as a disturbance that travels through a medium from one location to another. There are different types of waves that can be categorized as mechanical waves or non-mechanical waves. Mechanical waves are defined as waves which required medium for propagation. The propagation of waves takes place because of elasticity and inertial property of medium. Non-mechanical waves do not require any medium for propagation such as electromagnetic wave. In vacuum, electromagnetic wave travel with light velocity unlike mechanical wave where wave velocity depends on material medium.

In solid material, there are two basic types of mechanical waves shown in Figure 1.1 The first type of wave is a longitudinal wave also known as compression wave, in which the displacement is parallel to the direction of wave propagation. This wave is similar to sound wave in air, though the physics is rather different. The velocity of the wave depends on the material medium usually in the range of 5000 to 10000 m/s [1]. The second basic type of wave is the shear wave also known as transverse wave, in which the displacement is perpendicular to the direction of wave propagation. The velocity of shear wave is generally slower in the range of 3000 to 6000m/s [1]. In general, wave motion can be resolved into longitudinal and shear component. Seismic wave that travels through the earth during earthquake can have combination of P-wave (longitudinal wave) and S-wave (shear wave) known as Rayleigh wave. The principle operation of microwave acoustic devices utilizes mechanical or acoustic wave as the sensing mechanism. As the wave propagates through or on the surface of the material, any changes to the characteristic of the propagation affect the velocity and the amplitude of wave which can then be correlated to the corresponding physical quantity that is being measured.

Longitudianl waves	Shear waves
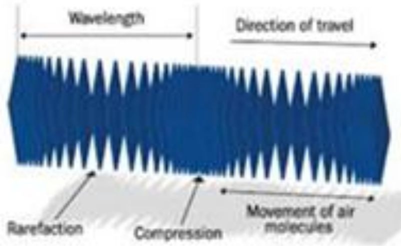	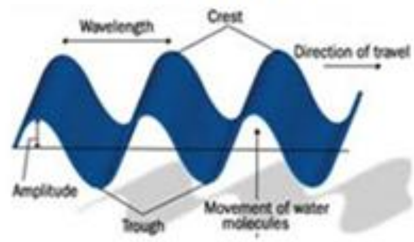
Particles in the medium vibrate parallel to the direction of propagation of the wave.	The particles of the medium vibrate perpendicular to the direction propagation of the wave.
The wave travels in the form of condensations and rarefactions.	The wave travels in the form of crests and troughs.
One condensation and a rarefaction constitute one wave.	One crest and one trough constitute one wave.
This cannot be polarized.	This wave can be polarized.

Figure 1.1: Types of mechanical wave.

Microwave acoustic devices use two different technologies depending on how the acoustic wave propagates through the piezoelectric material: Surface Acoustic Wave (SAW) and Bulk Acoustic Wave (BAW) devices. Figure 1.2 shows the schematic view of SAW and BAW resonators.

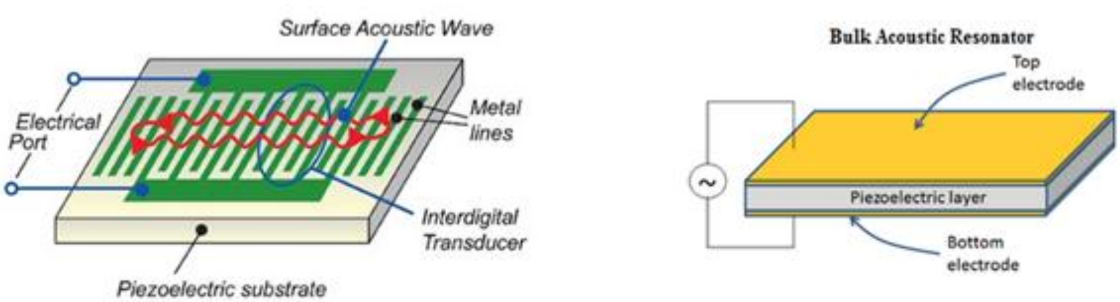

Figure 1.2: Schematic view of SAW resonator and BAW resonator.

For SAW devices, surface acoustic waves are excited by interdigital transducers (IDT) and propagate on the surface of the piezoelectric substrate [2, 3]. These are often known as Rayleigh waves due to both longitudinal and shear component of wave motion that decreases exponentially in amplitude as distance from the surface increases. The SAW waves are strongly confined, with about 90% of the energy propagating within one wavelength from the surface. SAW resonators are limited in their achievable operating frequency due to the separation of each finger in the IDT and the limit is around 2.5 GHz. Moreover, SAW devices are generally manufactured using Lithium Tantalate ($LiTaO_3$) or Lithium Niobate ($LiNbO_3$) crystal substrate [4], which are not compatible with the standard integrated circuits (IC) technology process.

For BAW devices, waves propagate through the bulk in the thickness direction and the frequency of operation depends on the thickness of piezoelectric substrate [5, 6, 7]. The operating frequency of BAW resonator is limited to around 10 GHz [8]; this is an approximate limit, although some of works found in the literature have mention application above 5 GHz [9, 10]. The commonly used piezoelectric materials for BAW devices are quartz (α-SiO_2), aluminum nitride (AlN) [11] and zinc oxide (ZnO) [12]. BAW resonators are compatible with standard integrated circuits technology process, which resulted in more compact and smaller size devices at low cost. The quality factor (Q) in BAW resonators is much higher than SAW resonators as demonstrated in [13]. Lastly, BAW resonators have a significant advantage over SAW that they have high power handling capability, therefore less dependence of the resonant frequencies with temperature under high-power conditions. Table 1.1 summarizes the main characteristics of SAW and BAW technologies. Both SAW and BAW have specific strengths and limitations, and in the most of the cases they complement each other instead compete against each other.

	SAW	BAW
Frequency range	up to 2.5 GHz	up to 10 GHz
Power Handling	$\sim$ 31 dBm	$\sim$ 36 dBm
Temperature Coefficient of Frequency (TCF)	-45 ppm/°C	-20 ppm/°C
Quality factor	$\sim$ 700	$\sim$ 2000
Compatibility with IC process	No	Yes

Table 1.1: Comparison of SAW and BAW technology [14].

1.2 Applications of SAW and BAW Devices

The use of microwave acoustic devices for different applications begins in the early 1960's at Bell Telephone Laboratories [15], most of the devices developed were amplifiers and oscillators at low frequencies around 100 MHz. The rapid revolution in microelectronics has been the driver in the recent evolution of microwave acoustic. Applications of microwave acoustic devices include wireless local area network (WLAN), Bluetooth, multimedia, global positioning systems (GPS), cellular mobile systems, satellite communications, and other military applications. The applications space for SAW and BAW where the technology cross over occurs as SAW moves to temperature compensated SAW (TC-SAW) and on to BAW devices as shown in Figure 1.3. BAW is preferred in high frequency and power applications due to its ability to satisfy the requirement of high performance devices while SAW is limited to applications at around 2.5 GHz due to low power handling capability and greater dependence of the resonant frequencies with temperature.

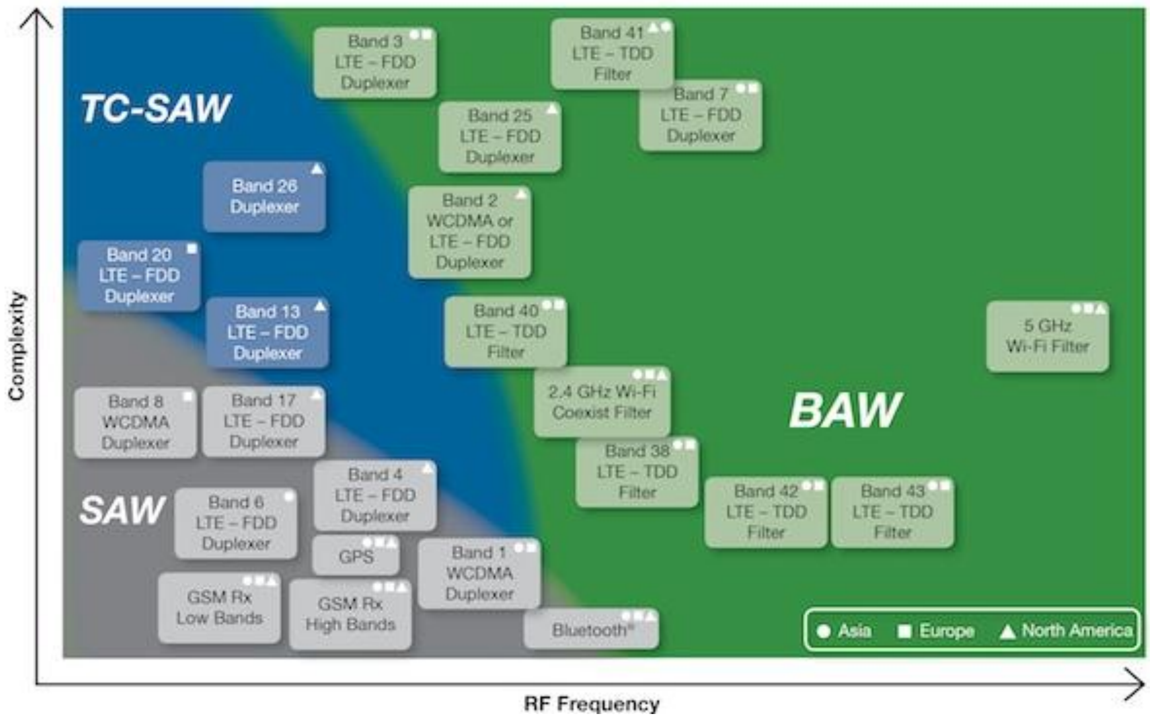

Figure 1.3: The applications space for SAW and BAW [16].

The demand for SAW devices has led to commercial market producing multi-million SAW devices every month. Specific SAW applications include convolvers, duplexers, filters and delay lines for the mobile telecommunications. Highlights of SAW based device applications are given in Table 1.2. On the other hand, BAW applications include resonators in precision clock oscillators, front-end GPS filters, and thin-film solidly mounted resonator (SMR) [1]. From the above, it is clear that telecommunication industry is largest user of microwave acoustic devices. There are some emerging applications for acoustic wave devices as sensors in automotive applications (torque and tire pressure sensor), medical applications (biosensors) and industrial and commercial applications (temperature and vapor chemical sensors). Figure 1.4 illustrates different types of acoustic wave sensor. These acoustic sensors are sensitive to acceleration, temperature, vibration and shocks. This thesis therefore focuses mainly on the acceleration sensitivity, force-frequency effect, and frequency-temperature behavior of BAW resonator.

Device	Applications
Medium loss SAW filter, (nondispersive):	IF filtering. Clock recovery. Nyquist filters. MSK modulation.
SAW delay line:	Path length equalizers. Altimeters. Pressure and temperature sensors. Tunable oscillators. Recirculating storage.
Fixed-tap delay line:	Pulse compression radar. Barker and quadraphase coding. Radar return simulation.
Programmable transversal filter:	Adaptive filtering for spread spectrum. Matched filtering. Channel equalization. Radar simulator.
SAW Comb filter:	Multiplexers. Multimode oscillators. Counters.
Low-loss SAW filter:	VHF/UHF front-end filtering. Mobile and cellular radio. Antenna duplexer.
SAW resonator:	Precision filters and fixed oscillators.

Table 1.2: Representative applications of SAW devices [17].

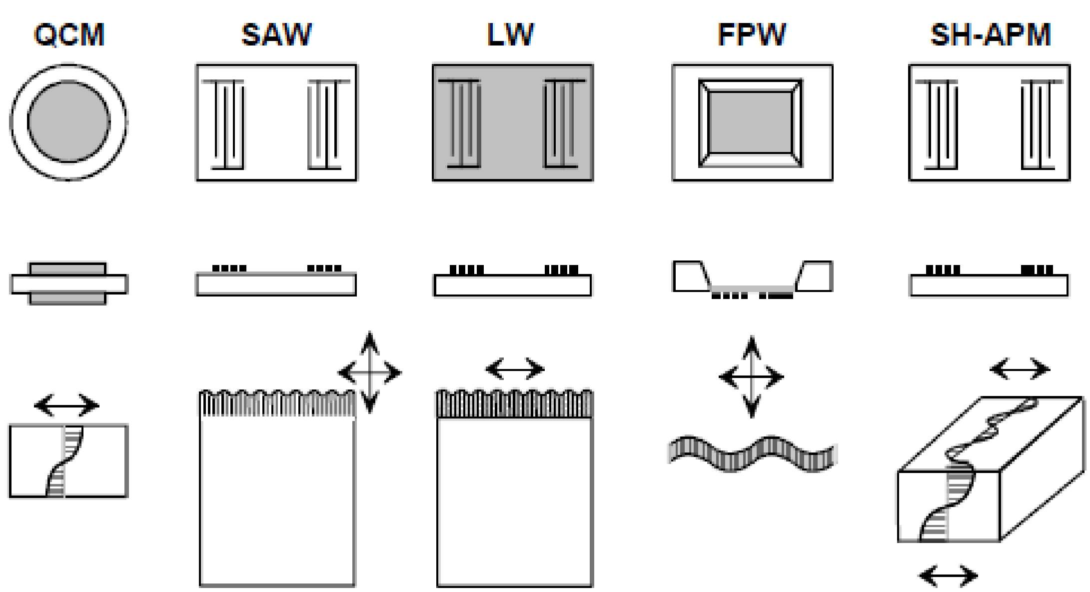

Figure 1.4: Different types of acoustic wave sensors [18].

1.3 General Overview of Quartz (BAW) Resonator

BAW resonator usually consists of a piezoelectric material sandwiched between two conducting electrode films and the resonator is precisely dimensioned and oriented with respect to the crystallographic axes. The basic principle of operation for a piezoelectric crystal resonator is a traveling wave combined with confinement structure to produce a standing wave whose frequency is determined jointly by the velocity of the traveling wave and the dimension of the confinement structure. The most commonly used piezoelectric material is quartz crystal which dates back as far as World War I, where sonar systems used quartz crystal to generate sound beams to detect under water objects. Because quartz is piezoelectric, an electric charge develops in the materials as a result of an applied mechanical stress, and this effect converts a mechanical stress in a crystal to a voltage and vice versa. This property is known as piezoelectricity. The direct piezoelectric effect and the inverse piezoelectric effect are shown in Figure 1.5. The word piezo-electricity takes its name from the Greek piezein “to press”, which literally means pressure electricity [19]. The direct piezoelectric effect was discovered by the Curie brother in 1880 and the piezoelectric effect is the key to the operation and theory behind BAW resonators.

For many years quartz has been the material of choice for satisfying needs in precise frequency control applications such as automotive, aerospace, telecommunications and consumer electronics. Compared to other piezoelectric resonators such as mechanical resonators, ceramic resonators and single crystal material, quartz resonator has proved to be superior by having a unique combination of properties. It is piezoelectric and has low intrinsic losses, which results in a quartz resonator having extremely high quality factor

(Q). The high Q allows its vibration to be driven with very little electrical power thus provides long operating life. The material properties of quartz resonator are extremely stable and highly repeatable. It is abundant in nature and easy to grow in large quantities at low cost. These unique combinations of properties have make quartz the most sought material in designing and manufacturing ultra-stable high frequency resonators.

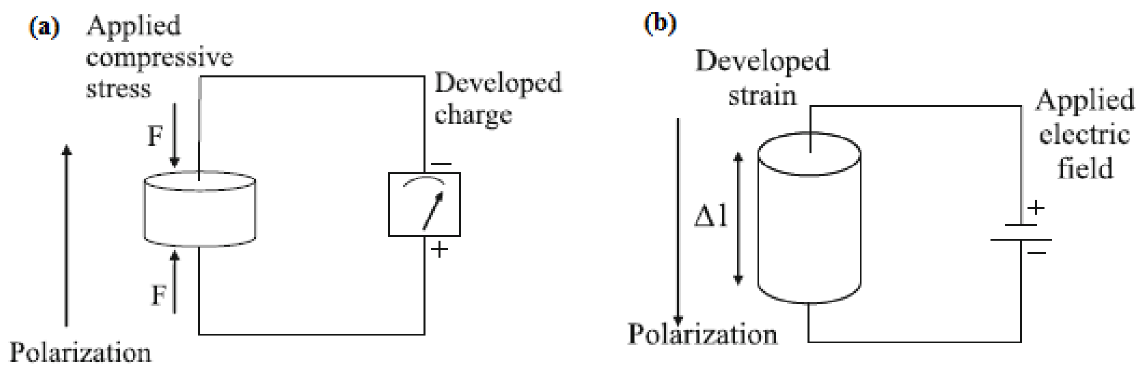

Figure 1.5: (a) Direct piezo-effect, (b) Inverse piezo-effect.

1.4 Literature Reviews

Quartz resonators are an indispensable component of modern electronics, they are used to generate frequencies to control and manage all communication system. They serve as GHz range passband filters allowing the appropriate range of frequencies to receive and transmit its communication signals and blocking out the unwanted frequencies. In high precision frequency controlled devices, the resonator should be stable in the order of parts per million. The performance of resonator is ultimately determined by the frequency stability of the resonator under force effect, temperature stability and acceleration. In this section, temperature stability and acceleration sensitivity of resonator are reviewed.

1.4.1 Temperature Stability

When a resonator is subject to temperature variation, the changes of resonator include: thermal expansion of the material, material elastic property, and dimensional change. All these changes will cause resonance frequency of the device to shift. The study of temperature stability has become an important aspect for the application of the resonators. There are two types of frequency-temperature behavior proposed by Ballato and Vig [20]. The first type is static frequency-temperature behavior in which heat exchange is slow enough so the resonator is in thermal equilibrium, the effects of temperature gradients is negligible (Isothermal changes). The second type is the dynamic frequency-temperature behavior in which the resonator is not in thermal equilibrium, the temperature surrounding produces thermal gradients where heat flows to or from active area of the resonator. This usually occurs during warm-up period where there is significant thermal transient effect in the resonator.

The static thermal behavior due to temperature influence is introduced by temperature coefficient of elastic constants and thermal expansion coefficients. The temperature coefficient of frequency ($Tf^{(n)}$) was measured by Bechmann and Ballato [21] using various orientations and thickness modes of double rotated quartz plates. Using the known relation between the temperature coefficient of stiffness ($Tc_{\lambda\mu}^{(n)}$) and the temperature coefficient of frequency, Bechmann and Ballato [22] derived the temperature coefficient of stiffness of alpha-quartz. Figure 1.6 shows the frequency-temperature behaviors of various type of cut obtained by Bechmann and Ballato using the newly calculated values of temperature coefficients of stiffness of alpha quartz. Sinha and Tiersten [23] computed the temperature derivative of the fundamental elastic constant using temperature coefficient of stiffness. Later, Lee and Yong derived linear equations of motion for small vibrations superposed on thermally induced deformation by steady and uniform temperature changes from the nonlinear field equations of thermoelasticity in Lagrangian formulation. From the solutions of these equations, they were able to calculate the temperature derivative of elastic stiffness and effective 2^{nd} and 3^{rd} temperature derivative of elastic stiffness. The frequency-temperature behaviors obtained using this theory is in very good agreement with experimental results.

In this dissertation, finite element analysis is used to study static frequency-temperature behavior of quartz resonators using different angles of cut of the crystal plates with respect to the crystallographic axes. A small change in the angle of cut can significantly change the frequency-temperature characteristics. Moreover, the stresses of the electrodes can also affect the frequency-temperature characteristics of crystal. By using different electrodes material in composite layer can help improve the frequency-temperature characteristics.

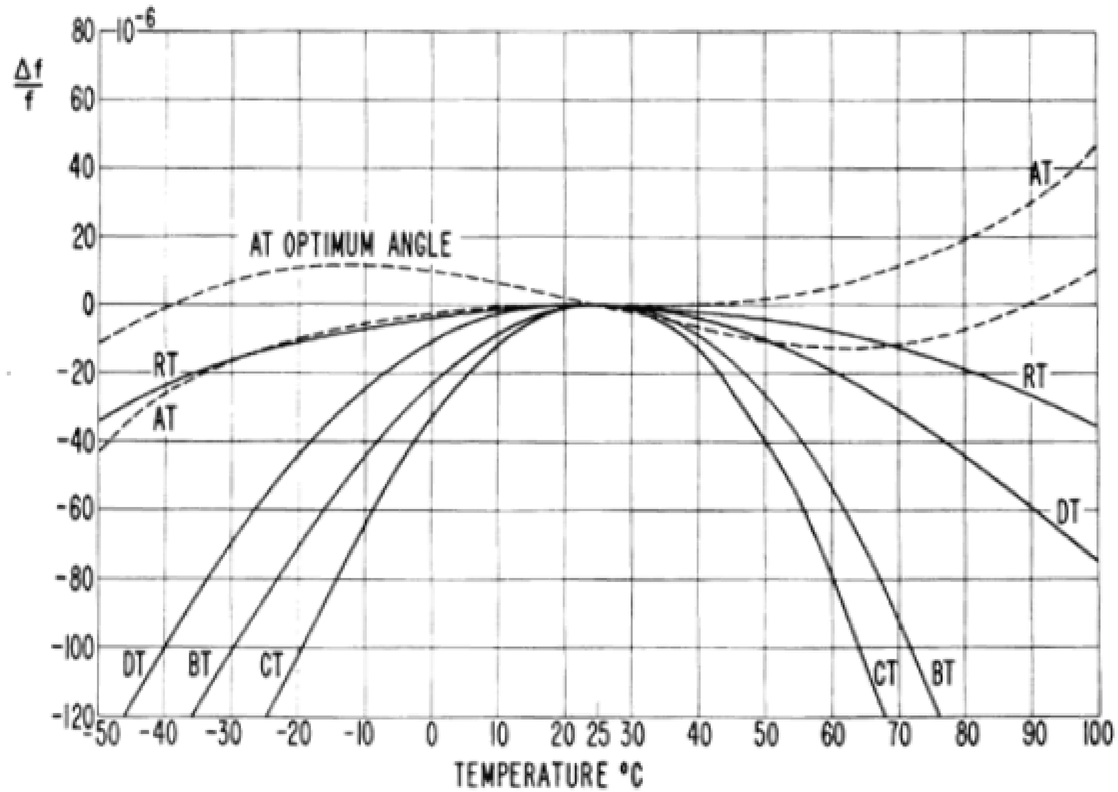

Figure 1.6: Frequency temperature behaviors of various types of cuts [24].

1.4.2 Acceleration Sensitivity

When a piezoelectric quartz crystal is subjected to external force or vibration, the resulting quasi-static stresses and strain on the crystal cause the resonant frequency to shift. Frequency shift in acceleration occurs primarily as result of resonator deformation because the nonlinear elastic behavior changes the acoustic velocity. Since the frequency of resonator is function of acoustic velocity and the dimensions of the quartz plate, the forces change the frequency.

The study of acceleration sensitivity is closely related with force-frequency effect which was first reported by Bottom [25]. The first attempt at an analytical solution to the force-frequency effect was by Mingins, Barcus and Perry in 1962 [26, 27]. They use a perturbation technique with linear elastic coefficients. In 1973, Lee, Wang, and Markenscoff [28, 29] calculated the force-frequency coefficient (Ratajski Coefficient) as function of azimuth using general theory of incremental elastic deformation superposed on finite initial deformation. In 1978, Janiaud, Nissim and Gagnepain [30] obtained analytic solution for the biasing stress in singly and doubly rotated plate subject to diametrical forces. Those results allow them to calculate the in-plane acceleration sensitivity.

Under acceleration, the body forces in the quartz plate are balanced by reaction forces from the mounting structure. Lee and Wu [31, 32, 33] extended the work to consider resonators with three and four point mounts and to study the influence of support configurations on the acceleration sensitivity. In addition to the above, there is an ongoing effort by Lee and Tang [34, 35] to use finite element analysis to accurately model the acceleration effects. There are several papers that reported experimental results on the force frequency effect [26, 36, 37] and the effects of bending moments [27, 38]. The results agree fairly well with the theoretical analyses.

Since the driving factor behind acceleration induced frequency shift is the deformation of resonator as it reacts against its mounting structure. The efforts to reduce the sensitivity of individual resonators under the effect of acceleration have been emphasized on the support structure. Lukaszek and Ballato [39] proposed a plate geometry that would assure the proper support configuration to reduce the force-frequency effect. Besson, Gagnepain, Janiaud and Valdois [40] proposed a support structure that insured symmetry with the median plane of the resonator plate. The lack of progress to reduce the acceleration sensitivity below 10^{-10}/g level has resulted in several new compensation techniques. Ganepain and Wall [41] used the passive method of mechanically arranging two resonators such that the components of the acceleration normal to the plates were antiparallel. Ballato suggested a method for compensation using a resonator pair made of enantiomorphs. Przyjemski [42], Emmons [43], and Rosati [44] used an active method, where they sense the acceleration magnitude with an accelerometer then fed the signal into a tuning circuit in order to counter the acceleration-induced frequency changes. From the above, progress has been made in understanding the causes of acceleration sensitivity, but more work is needed to reduce the level of acceleration sensitivity.

In this dissertation, finite element analysis is used to study the acceleration sensitivity of quartz resonator subjected to In-Plane and Out of Plane body forces. We present a new method using edge electrodes in which a DC bias field is employed could potentially reduce the acceleration sensitivity in the *Y*-axis direction by about two orders of magnitude. Moreover, we studied the behavior of vibrating crystal plate under the action of external forces in fundamental mode and third overtone mode due to compressional forces and bending moments which would help to reduce force-frequency effect.

1.5 Research Motivations and Focus

Since the early 20th century, quartz sensors have been used to measure physical parameters such as temperature, pressure and acceleration. Because of their compact size and rugged characteristics, quartz resonator has been used for the majority of the last century and its capability has not been fully realized. The frequency instabilities of resonators due to temperature variation and external forces have been the utmost concern in high frequency controlled devices and the primary reason is because of the complex anisotropic and nonlinear nature of the quartz crystal. The nonlinear elastic constants are the source of the instabilities in crystal resonator such as acceleration sensitivity, the thermal expansion effect and the force-frequency effect. Frequency control and stability of these quartz resonators are one of the most important criteria in the design of resonators. The design of ultra-stable resonators are determined by various parameters such as the type of quartz cut, angle of the quartz cut, mode of operation and the dimensions of the quartz blank.

In this dissertation, an accurate three dimensional finite element method for the frequency behavior of quartz with respect to temperature, force, pressure, acceleration and electric fields are studied for applications to high stability resonators. The nonlinear materials properties are incorporated into the 3-D equations of linear piezoelectric with quasi-electrostatic approximation which include losses due to mechanical damping in the solid [45]. The goal of current work will establish a valuable tool to efficiently explore the insight into the modeling of nonlinear multi-physical phenomena.

1.6 Dissertation Outline

- Chapter 1 presents the difference between BAW and SAW technology as well as the application of these devices. Literature review of acceleration sensitivity and temperature stability.
- Chapter 2 consists of the derivation of the piezoelectric governing equations and constitutive equations. These equations are implemented in the

succeeding chapters to study the frequency-temperature behavior of quartz and the acceleration sensitivity in quartz resonators.

- Chapter 3 briefly introduces quartz crystallography with system of notation for the orientation of crystalline plates and Butterworth Van Dyke (BVD) equivalent circuit model.
- Chapter 4 evaluates the acceleration sensitivity in quartz resonators by implementing the incremental field equations and the use of DC bias effect to actively reduce acceleration sensitivity.
- Chapter 5 investigates the effect of external forces on the fundamental and third overtone of *AT*-cut and *SC*-cut crystal plates. Finite element modes are developed and the results are compared with experimental measured data.
- Chapter 6 presents the analysis of frequency-temperature behavior of quartz resonators. Finite element models for the temperature dependence of quartz resonators are developed with the use of electrode stresses for improving frequency-temperature behavior of quartz resonators.
- Chapter 7 presents conclusion of this study and possible future works.

Chapter 2 Theory of Piezoelectricity

2.1 Introduction

The first attempt to derive the theory of piezoelectricity was made by Voigt in 1910. The small vibrations of piezoelectric bodies are governed by the equations of the linear theory of piezoelectricity in which the quasi-static electric field is coupled to the dynamic mechanical motion. The piezoelectricity is the coupling phenomenon between electrical and mechanical behavior. The direct piezoelectric effect occurs when an applied stress produces an electric polarization. The inverse piezoelectric effect occurs when an applied electric field produces a strain. In linear piezoelectricity theory, the full electromagnetic equations are not usually needed. The quasi-electrostatic approximation is adequate because the phase velocity of acoustic wave is approximately five orders of magnitude less than the velocities of electromagnetic waves. Under these circumstances the magnetic effect can be shown to be negligible compared to electric effects. In general the linear theory of piezoelectricity has been the foundation for most of the analytical work carried out in the design and analysis of piezoelectric materials. In this chapter, we introduce the equations which describe electromechanical properties of piezoelectric material. The presentation is based on the IEEE standard of piezoelectricity [46] which is widely accepted as being a good representation of piezoelectric material properties.

2.2 Governing Equations of Piezoelectricity

The general mechanical equations of motion for a continuum satisfying balance of linear momentum are given as follow: (*Note: A comma followed by an index denotes partial* *derivative with respect to a space coordinate and an over-dot quantity denotes time derivative*)

Stress equations of motion:

$$T_{ij,i} + b_j = \rho \ddot{u}_j, \tag{2.1}$$

$$T_{ij} = T_{ji}, \tag{2.2}$$

where T_{ij} are the components of Cauchy stress tensor, and the stress tensor T_{ij} is symmetric, b_i are components of body forces, u_i are the components of displacement fields and ρ is the mass density of the material.

Displacement gradient:

$$u_{i,j} = \partial u_i / \partial x_j, \tag{2.3}$$

$$u_{i,j} = S_{ij} + \omega_{ij}, \tag{2.4}$$

Strain tensor:

$$S_{ij} = \frac{1}{2}\left(u_{i,j} + u_{j,i}\right), \tag{2.5}$$

Rotation tensor:

$$\omega_{ij} = \frac{1}{2}\left(u_{i,j} - u_{j,i}\right), \tag{2.6}$$

since $u_{i,j}$ is a second rank tensor with nine terms, we can decompose it into its symmetric and anti-symmetric parts. The symmetric part of displacement gradient determines the strain tensor S_{ij}. The strain is the deformation per unit length and hence a dimensionless quantity. The anti-symmetric part of displacement gradient determines the infinitesimal rigid body rotation tensor ω_{ij}.

The electromagnetic equations in a region with no charges and no currents are given as follow: (source-free $\rho_e = 0$ and $J = 0$)

Maxwell's equations:

$$\epsilon_{ijk} H_{k,j} = \dot{D}_i, \tag{2.7}$$

$$\epsilon_{ijk} E_{k,j} = -\dot{B}_i, \tag{2.8}$$

$$B_{i,i} = 0, \tag{2.9}$$

$$D_{i,i} = 0, \tag{2.10}$$

where D_i are the electric displacement components, B_i are the magnetic flux components, E_k are the electric field components, H_k are the magnetic field components, ϵ_{ijk} are the components of permutation tensor and:

$$D_i = \varepsilon_0 E_i + P_i, \tag{2.11}$$

$$B_i = \mu_0 H_i, \tag{2.12}$$

where P_i are the component of electric polarization vector, ε_0 and μ_0 are the permittivity and permeability of vacuum given by:

$$\varepsilon_0 = 8.854 \times 10^{-12}\ ({}^{F}/_{m}),$$

$$\mu_0 = 4\pi \times 10^{-7}\ ({}^{H}/_{m}).$$

As mention earlier the quasi-static approximation [47] is adequate because the velocity of the elastic waves is much smaller than the velocity of electromagnetic waves. Therefore the magnetic field due to the elastic wave is negligible, thus time derivative of the magnetic flux can be neglected without loss of accuracy and this leads to

$$\dot{B}_i = {}^{\partial B}/_{\partial t} \approx 0, \tag{2.13}$$

this means that the electric field E_k is derived from a scalar potential

$$E_k = -\varphi_{,k}. \tag{2.14}$$

The term φ denotes scalar potential. In quasi-static approximation, the Maxwell equations reduce to just the charge equation of electrostatics and electric field:

$$D_{i,i} = 0, \tag{2.15}$$

$$E_k = -\varphi_{,k}. \tag{2.16}$$

The solution of piezoelectric vibration problems involves the simultaneous solutions of mechanical equations (2.1) through (2.6) and the Maxwell equations (2.15) through (2.16). Therefore, a set of constitutive equations relating the quantities T_{ij}, S_{ij}, D_i and E_k is required.

2.3 Piezoelectric Constitutive Equations

The physics involved in piezoelectric theory may be regarded as coupling between Maxwell's equations of electromagnetism and elastic stress equations of motion. The coupling takes place through the piezoelectric constitutive equations. The general constitutive relations for piezoelectric continuum are developed from the first law of thermodynamics [48] [49].

For a general piezoelectric material, the total internal energy U is given by the sum of the mechanical and electrical work done in differential form:

$$\dot{U} = T_{ij}\dot{S}_{ij} + E_i\dot{D}_i, \tag{2.17}$$

where U is the internal energy, T_{ij} is the mechanical stress, S_{ij} is the strain, E_i is the electric field and D_i is the electric displacement and for the piezoelectric continuum. The electric enthalpy H is defined by:

$$H = U - E_iD_i. \tag{2.18}$$

Then differentiating with respect to time yields

$$\dot{H} = \dot{U} - E_i\dot{D}_i - \dot{E}_iD_i, \tag{2.19}$$

which with (2.17) yields

$$\dot{H} = T_{ij}\dot{S}_{ij} - \dot{E}_iD_i. \tag{2.20}$$

Equation (2.20) implies that the electric enthalpy is a thermodynamic potential in which the independent variables are the strain deformation S_{ij} and the electric field E_i, we assume

$$H = H(S_{ij}, E_i), \tag{2.21}$$

differentiating (2.21) with respect to time yields

$$\dot{H} = {}^{\partial H}/_{\partial S_{ij}}\, \dot{S}_{ij} + {}^{\partial H}/_{\partial E_i}\, \dot{E}_i, \tag{2.22}$$

and substituting from (2.20), we have

$$\left(T_{ij} - {}^{\partial H}/_{\partial S_{ij}}\right) \dot{S}_{ij} - \left(D_i + {}^{\partial H}/_{\partial E_i}\right) \dot{E}_i = 0. \tag{2.23}$$

Since equation (2.23) is an identity which must hold for arbitrary $\dot{S}_{ij}$ and $\dot{E}_i$ which are consistent with the condition $\dot{S}_{ij} = \dot{S}_{ji}$ and ${}^{\partial H}/_{\partial S_{ij}} = {}^{\partial H}/_{\partial S_{ji}}$, we have

$$T_{ij} = {}^{\partial H}/_{\partial S_{ij}}, \tag{2.24}$$

$$D_i = -\,{}^{\partial H}/_{\partial E_i}. \tag{2.25}$$

In linear piezoelectric theory, we construct a quadratic form of H:

$$H = \frac{1}{2} C^E_{ijkl} S_{ij} S_{kl} - e_{kij} E_k S_{ij} - \frac{1}{2} \varepsilon^S_{ij} E_i E_j, \tag{2.26}$$

$$C^E_{ijkl} = C^E_{ijlk} = C^E_{jikl} = C^E_{klij},$$

$$e_{kij} = e_{kji},$$

$$\varepsilon^S_{ij} = \varepsilon^S_{ji},$$

where C^E_{ijkl}, e_{kij} and ε^S_{ij} are second order elastic, piezoelectric, and dielectric constants respectively. In general there are 21 independent elastic constants, 18 independent piezoelectric constants, and 6 independent dielectric constants. From equations (2.24)-(2.26) we obtain the linear piezoelectric constitutive equations:

$$T_{ij} = C^{E}_{ijkl} S_{kl} - e_{kij} E_k, \tag{2.27}$$

$$D_i = e_{ikl} S_{kl} + \varepsilon^{S}_{ik} E_k. \tag{2.28}$$

Note that upon substituting equations (2.18) and (2.28) into equation (2.26) yields the stored energy function U:

$$U = \frac{1}{2} C^{E}_{ijkl} S_{ij} S_{kl} + \frac{1}{2} \varepsilon^{S}_{ij} E_i E_j. \tag{2.29}$$

The stress-charge form of piezoelectric constitutive equations (2.27) and (2.28) show coupling between electrical and mechanical quantities are implemented in finite element analysis. The nonlinear piezoelectric constitutive equations derived by Shiv P. Joshi [50] and Yasuo Cho [51] are rather complicated and lengthy. The details of derivation are not presented in this section. Interested readers should consult reference [50] for complete derivation of nonlinear piezoelectric constitutive equations. The alternative forms of linear and nonlinear constitutive equations are listed in Appendix A.

In order to write elastic and piezoelectric tensors in matrix form, the Piola-Voigt compact matrix notation can be employed. This compact notation replaces the subscripts of ij and kl by p and q according to Table 2.1. As shown in Table 2.1, i, j, k and l take the values from 1 to 3; but p and q take the values from 1 to 6. It should be noted that when the compact matrix notation is used, the transformation properties of the tensors become unclear. Hence, the tensor indices must be employed when coordinate transformations are to be made.

Einstein tensor notation	Voigt notation
ij* or *kl	***p* or *q***
11 (*xx*)	1
22 (*yy*)	2
33 (*zz*)	3
23 or 32 (*yz* or *zy*)	4
13 or 31 (*xz* or *zx*)	5
12 or 21 (*xy* or *yx*)	6

Table 2.1: Compact matrix notation.

2.4 Differential Equations of Piezoelectricity

The basic differential equation and boundary conditions governing the behavior of the linear piezoelectric continuum are developed from fundamental continuum concept. The differential equations of piezoelectricity can be derived using the constitutive equations along with stress equations of motion, the charge equation of electrostatics, strain displacement relations and the electric field-electric potential relations. The derivation is shown below.

Upon further substitution of equations (2.5) and (2.14) into equations (2.27) and (2.28), then equations (2.27) and (2.28) into equations (2.1) and (2.10) yields the differential equations for the linear piezoelectric continuum:

$$C^E_{ijkl}u_{k,li} + e_{kij}\varphi_{,ki} + b_j = \rho\ddot{u}_j, \tag{2.30}$$

$$e_{ikl}u_{k,li} + \varepsilon^S_{ik}\varphi_{,ki} = 0. \tag{2.31}$$

We now have a system of equations that can be solved with the proper mechanical and electrical boundary conditions which we have yet to determine.

At traction-free surface, we have

$$n_i T_{ij} = 0, \tag{2.32}$$

where n_i denotes the components of the unit normal to the surface.

At a displacement-free surface (fixed), we have

$$u_j = 0. \tag{2.33}$$

At an air-dielectric interface (unelectroded surface), we have

$$n_i D_i = 0. \tag{2.34}$$

For shorted electrodes (equal potential), we have

$$\varphi = 0. \tag{2.35}$$

These appropriate boundary conditions must be adjoined to the differential equations (2.30) and (2.31) of the linear piezoelectric continuum for a unique solution.

In an electrode region, the current I out of the upper electrode and into the lower electrode is given by:

$$I = \int_s n_i \dot{D}_i ds = \pm YV, \tag{2.36}$$

where the $\pm$ depends on the orientation of the coordinate axes, Y is the admittance and the voltage V is related to the potential difference given by:

$$V = \varphi(x = h) - \varphi(x = -h). \tag{2.37}$$

2.5 Variation Principle for a Nonlinear Piezoelectric Continuum

Since quartz is the primary interested piezoelectric material, and has low electromechanical coupling factor less than 10% for rotated Y-cuts. The third order piezoelectric constants, electrostrictive, and third order dielectric constants will no longer considered here because they appear negligible in the electroelastic effect. The fundamental variational equation of electro-elasticity is a generalization of the Hamilton's principle and can be deduced from the principle of virtual work. The variational principle for a piezoelectric continuum is derived using the principle of virtual work:

$$\delta \int_{t_0}^{t} L\, dt + \int_{t_0}^{t} \delta W\, dt = 0, \tag{2.38}$$

where t is the time, L is the Largrangian which contains all physical information concerning the system and δW is the work done by surface traction, surface charge and body force through varied displacement.

Considered a piezoelectric body subject to prescribe surface tractions p, surface charge σ, and body force b. The virtual work per unit area done by the prescribed surface tractions in a small virtual displacement of the surface is $p_k\ \delta u_k$. The electrical analog of the virtual work per unit area done by the prescribed surface charge q in a small variation of electrical potential is $-q\ \delta\varphi$. The virtual work per unit volume done by the body force through small virtual displacement is $b_k\ \delta u_k$. We will show that the variational principle presented here yields the nonlinear equations of piezoelectricity in Lagrangian forumulation.

The Lagrangian for this piezoelectric medium is defined by

$$L = \int_V (\tfrac{1}{2}\rho \dot{u}_k \dot{u}_k - H(S_{ij}, E_i))\, dV, \tag{2.39}$$

$$H(S_{ij}, E_i) = \tfrac{1}{2} C^E_{ijkl} S_{ij} S_{kl} + \tfrac{1}{6} C^E_{ijklmn} S_{ij} S_{kl} S_{mn} - e_{kij} E_k S_{ij} - \tfrac{1}{2} \varepsilon^S_{ij} E_i E_j, \tag{2.40}$$

where C^E_{ijklmn} is the third order elastic constants, and

$$\delta W = \int_S (p_k \delta u_k - q\delta\varphi)\, dS + \int_V b_k \delta u_k\, dV. \tag{2.41}$$

Hence, the variational principle takes the form

$$\delta \int_{t_0}^{t} dt \int_V (\tfrac{1}{2}\rho \dot{u}_k \dot{u}_k - H(S_{ij}, E_i))\, dV +$$

$$\int_{t_0}^{t} dt \int_S (p_k \delta u_k - q\delta\varphi)\, dS + \int_{t_0}^{t} dt \int_V b_k \delta u_k\, dV = 0, \tag{2.42}$$

where p_k and q are prescribed and all variations vanish at t_0 and t. From the relations:

$$S_{ij} = \frac{1}{2}\left(u_{i,j} + u_{j,i} + u_{i,k}u_{k,j}\right), \qquad E_i = -\varphi_{,i},$$

$$T_{ij} = {\partial H}/{\partial S_{ij}}, \qquad D_i = -{\partial H}/{\partial E_i}, \qquad {\partial}/{\partial t} \approx {d}/{dt},$$

we examined the expression (2.42) term by term.

First term:

$$\delta \int_{t_0}^{t} dt \int_V \frac{1}{2}\rho \dot{u}_k \dot{u}_k \, dV = \int_{t_0}^{t} dt \int_V \rho\, \dot{u}_k\, \delta\dot{u}_k\, dV$$

$$= \int_{t_0}^{t} dt\ \int_V ({\partial}/{\partial t}\,(\rho\dot{u}_k\, \delta u_k\, dV) - \rho\ddot{u}_k\, \delta u_k\, dV)$$

$$= -\int_{t_0}^{t} dt\ \int_V \rho\ddot{u}_k\, \delta u_k\, dV, \tag{2.43}$$

since δu_k is zero at t_0 and t.

Second term:

$$\delta \int_{t_0}^{t} dt \int_V H(S_{ij}, E_i)\ dV = \int_{t_0}^{t} dt\ \int_V ({\partial H}/{\partial S_{ij}}\, \delta S_{ij} + {\partial H}/{\partial E_i}\, \delta E_i)\, dV \tag{2.44}$$

and

$$\delta S_{ij} = \beta_{ki}\delta u_{k,j}, \qquad \delta E_i = -\delta\varphi_{,i},$$

where β_{ki} is the initial deformation gradient given by

$$\beta_{ki} = \delta_{ki} + u_{k,i}. \tag{2.45}$$

Rewrite expression (2.44) with the use of divergence theorem yield

$$\delta \int_{t_0}^{t} dt \int_V H\ dV = \int_{t_0}^{t} dt\ \int_V (T_{ij}\beta_{ki}\delta u_{k,j} + D_i\delta\varphi_{,i})\, dV$$

$$= \int_{t_0}^{t} dt\ \int_V (n_j T_{ij}\beta_{ki}\delta u_k + n_i\, D_i\delta\varphi)\, dS -$$

$$\int_{t_0}^{t} dt\ \int_V ((T_{ij}\beta_{kj})_i\delta u_k + D_{i,i}\delta\varphi)\, dV. \tag{2.46}$$

After substituting the expression (2.46) and (2.43) back into (2.42) and rearranging the terms we have

$$\delta \int_{t_0}^{t} dt \, [\int_V ((T_{ij}\beta_{kj})_i + b_k - \rho \ddot{u}_k)\delta u_k \, dV + \int_V D_{i,i}\delta\varphi \, dV +$$

$$\int_S (p_k - n_j T_{ij}\beta_{ki})\delta u_k \, dS - \int_S (q + n_j D_j)\delta\varphi \, dS] = 0. \quad (2.47)$$

Since (2.47) holds for arbitrary volume and surface, the volume and surface integral vanish separately. The nonlinear stress equations of motion and charge equations of electrostatics are obtained from (2.47) and the simplified version of nonlinear constitutive equations are obtained from (2.40) using (2.24) and (2.25).

Stress equations of motion:

$$(T_{ij} + T_{jk}u_{i,k})_{,i} + b_j = \rho \ddot{u}_j \quad \text{in } V, \quad (2.48)$$

$$p_k = n_j(T_{ij} + T_{jk}u_{i,k}) \quad on \quad S, \quad (2.49)$$

Charge equation of electrostatics:

$$D_{i,i} = 0 \quad \text{in } V, \quad (2.50)$$

$$q = -n_j D_j \quad on \quad S, \quad (2.51)$$

Constitutive equations:

$$T_{\boldsymbol{ij}} = C^E_{ijkl}S_{kl} + \frac{1}{2}C^E_{ijklmn}S_{kl}S_{mn} - e_{kij}E_k, \quad (2.52)$$

$$D_i = e_{ikl}S_{kl} + \varepsilon^S_{ik}E_k. \quad (2.53)$$

2.6 Summary of Equations

The general governing equations of linear and nonlinear piezoelectricity are listed in this section. These equations are implemented in COMSOL Multiphysics finite element analysis software to study the acceleration sensitivity, force frequency effect, and frequency-temperature behavior of quartz crystal in the succeeding chapters.

2.6.1 Linear Piezoelectricity

Strain-displacement relation:

$$S_{ij} = \frac{1}{2}\left(u_{i,j} + u_{j,i}\right), \tag{2.54}$$

Stress equations of motion:

$$T_{ij,i} + b_j = \rho\ddot{u}_j, \tag{2.55}$$

$$T_{ij} = T_{ji}, \tag{2.56}$$

Electric field-potential relation:

$$E_i = -\varphi_{,i}, \tag{2.57}$$

Charge equation of electrostatics:

$$D_{i,i} = 0, \tag{2.58}$$

Constitutive equations:

$$T_{ij} = C^E_{ijkl}S_{kl} - e_{kij}E_k, \tag{2.59}$$

$$D_i = e_{ikl}S_{kl} + \varepsilon^S_{ik}E_k. \tag{2.60}$$

2.6.2 Nonlinear Piezoelectricity

Strain-displacement relation:

$$S_{ij} = \frac{1}{2}\left(u_{i,j} + u_{j,i} + u_{i,k}u_{k,j}\right), \tag{2.61}$$

Stress equations of motion:

$$(T_{ij} + T_{jk}u_{i,k})_{,i} + b_j = \rho\ddot{u}_j, \tag{2.62}$$

$$T_{ij} = T_{ji}, \tag{2.63}$$

Electric field-potential relation:

$$E_i = -\varphi_{,i}, \tag{2.64}$$

Charge equation of electrostatics:

$$D_{i,i} = 0, \tag{2.65}$$

Constitutive equations:

$$T_{\boldsymbol{ij}} = C_{ijkl}^{E} S_{kl} - e_{kij} E_k + \frac{1}{2} C_{ijklmn}^{E} S_{kl} S_{mn} - \frac{1}{2} l_{klij} E_k E_l - e_{mijkl} E_m S_{kl}, \quad (2.66)$$

$$D_i = e_{ikl} S_{kl} + \varepsilon_{ik}^{S} E_k + \frac{1}{2} e_{ijklm} S_{jk} S_{lm} + \frac{1}{2} \varepsilon_{ijk}^{S} E_j E_k + l_{ijkl} E_j S_{kl}. \quad (2.67)$$

Chapter 3 Crystallography Applied to Piezoelectric Crystal

3.1 General

The purpose of this chapter is to relate the fundamental theory of piezoelectric solids using the theoretical concepts of continuum mechanics, as presented in Chapter 2, and the application of the equations to particular piezoelectric materials by a branch of science called crystallography. The guidelines are based on the IEEE standard of piezoelectricity published in 1987 [46] which are widely accepted as a good representation of piezoelectric material properties. Most piezoelectric materials of interest for technological applications are crystalline solids. These can be single crystals, either formed in nature or formed by synthetic processes. Since the theoretical principles developed in Chapter 2 are presented with the generality of tensor formulations, connection to the theory in Chapter 2 with real piezoelectric material is required as a first step in the definition of crystal axes within the different crystallographic point groups and the association of the crystal axes with Cartesian coordinate axes used in mathematical analysis.

3.2 Basic Terminology of Crystal Systems

The term crystal is applied to a solid in which the atoms are arranged in a single pattern repeated throughout the body. The atoms are arranged in a regular manner forming a body with specific geometrical characteristics. Each group of atoms in a crystal forms a virtual three-dimensional grid as bounded by a parallelepiped, and each parallelepiped regarded as one of the ultimate building blocks of the crystal. The crystal is formed by stacking the basic parallelepiped together without any spaces between them called a unit cell. The edges of a unit cell correspond to axes in a three-dimensional grid called a point lattice. Since the choice of a particular set of atoms to form a unit cell is arbitrary, it is evident that there is a wide range of choices in the shape and dimensions of the unit cell. In practice, the unit cell is selected which is most simply related to the actual crystal faces and X-ray reflections, and which has the symmetry of the crystal itself.

In crystallography the properties of a crystal are described in terms of the natural coordinate system. The symbols a, b, c, are used for this natural system; a_0, b_0, and c_0 refer to the dimensions of the unit cell along these axes In a cubic crystal, these axes are of equal length and mutually perpendicular, while in a triclinic crystal they are unequal lengths and no two axes are mutually perpendicular. The face of any crystal are all parallel to planes whose intercepts on the a, b, c axes are small multiples of unit distances or infinity so that their reciprocals, when multiplied by a small common factor are small integers or zero. These are the indices of the planes. In this nomenclature we have, for example, face [100], [010], [001], also called the a, b, c faces, respectively. In the orthorhombic, tetragonal and cubic systems, these faces are normal to the a, b, c axes. Even in the monoclinic and triclinic systems these faces contain respectively, the b and c, a and c, and a and b axes. As referred to the set of rectangular axes *X, Y, Z,* these indices are in general irrational except for cubic crystals.

Depending on their degrees of symmetry, crystals are commonly classified into seven systems: triclinic, monoclinic, orthorhombic, tetragonal, trigonal, hexagonal and cubic. The seven systems are divided into 32 point groups (classes) according to their symmetry with respect to a point given in Table 3.1. Of the 32 crystallographic point groups, those highlighted in magenta possess a center of inversion and are called centrosymmetric, while those highlighted in red possess no improper rotations are termed enantiomorphic. A third type highlighted in bold type is referred to as polar in which every symmetry operation leaves more than one point unmoved.

Crystal System	**32 Crystallographic Point Groups**						
Triclinic	**1**	$\bar{1}$					
Monoclinic	**2**	$\boldsymbol{m}$	$2/m$				
Orthorhombic	222	$\boldsymbol{mm2}$	mmm				
Tetragonal	**4**	$\bar{4}$	$4/m$	422	$\boldsymbol{4mm}$	$\bar{4}2m$	$4/mmm$
Trigonal	**3**	$\bar{3}$	32	$\boldsymbol{3m}$	$\bar{3}m$		
Hexagonal	**6**	$\bar{6}$	$6/m$	622	$\boldsymbol{6mm}$	$\bar{6}2m$	$6/mmm$
Cubic	23	$m\bar{3}$	432	$\bar{4}3m$	$m\bar{3}m$		

Table 3.1: Crystallographic point groups.

Out of 32 classes, 12 classes contain too high degree of symmetry to show piezoelectric properties, thus 20 classes can be piezoelectric. Every system contains at least one piezoelectric class. The symbols used for the 32 crystal class are those recommended by the International Union of Crystallography (also known as the Herman-Mauguin symbols). In this system, an axis of rotation is indicated by one of the number 1,2,3,4,6. The number indicates how many full rotations about the axis which is required to bring the crystal into an equivalent position in regard to its internal structural properties. The number 1 indicates no symmetry at all, since any structure must coincide after a complete rotation (360° rotation), while 2 indicates a two-fold axis of rotation.

When a rotation axis is followed by a slash and an m, then this mirror is perpendicular to the rotation axis. The point groups of the trigonal crystal system possess a three-fold axis, while those of the tetragonal and hexagonal crystal systems possess a four-fold and six-fold axis respectively. The cubic point groups all have multiple three-fold axes and the orthorhombic point groups have two-fold symmetry either 2 or m with respect to each of the *X, Y, Z,* directions of an orthogonal axis system. The monoclinic point groups are limited to two-fold symmetry with respect to a single axis direction and lastly, the triclinic point groups can only have an axis of order 1. A convenient summary of the 32 point groups with examples is given in Table 3.2.

Class	Materials	Compounds
$1 = C_1$	Kaolinite	$Al_2Si_2O_5(OH)_4$
$\bar{1} = C_i$	Copper sulfate	$CuSO_4 \cdot 5H_2O$
$2 = C_2$	Sucrose	$C_{12}H_{12}O_{11}$
$m = C_S$	Potassium nitrite	KNO_2
$2/m = C_{2h}$	Orthoclase	$KAlSi_3O_8$
$222 = D_2$	Iodic acid	HIO_3
$mm2 = C_{2V}$	Sodium nitrite	$NaNO_2$
$mmm = D_{2h}$	Forsterite	Mg_2SiO_4
$3 = C_3$	Nickel tellurate	Ni_3TeO_6
$\bar{3} = C_{3i}$	Ilmenite	$FeTiO_3$
$32 = D_3$	Low-quartz	SiO_2
$3m = C_{3V}$	Lithium niobate	$LiNbO_3$
$\bar{3}m = D_{3d}$	Corundum	Al_2O_3
$4 = C_4$	Iodosuccinimide	$C_4H_4INO_2$
$\bar{4} = S_4$	Boron phosphate	BPO_4
$4/m = C_{4h}$	Scheelite	$CaWO_4$
$422 = D_4$	Nickel sulfate	$NiSO_4 \cdot 6H_2O$
$4mm = C_{4V}$	Barium titanate	$BaTiO_3$
$\bar{4}2m = D_{2d}$	Potassium dihydrogen phosphate	KH_2PO_4
$4/mmm = D_{4h}$	Rutile	TiO_2
$6 = C_6$	Nepheline	$NaAlSiO_4$
$\bar{6} = C_{3h}$	Lead germanate	$Pb_5Ge_3O_{11}$
$6/m = C_{6h}$	Apatite	$Ca_5(PO_4)_3F$
$622 = D_6$	High-quartz	SiO_2
$6mm = C_{6V}$	Zincite	ZnO
$\bar{6}m2 = D_{3h}$	Benitoite	$BaTiSi_3O_9$
$6/mmm = D_{6h}$	Beryl	$Be_3Al_2Si_6O_{18}$
$23 = T$	Sodium chlorate	$NaClO_3$
$m3 = T_h$	Pyrite	FeS_2
$432 = O$	Manganese	β-Mn
$\bar{4}3m = T_d$	Zincblende	ZnS
$m3m = O_h$	Rocksalt	$NaCl$

Table 3.2: Examples of the 32 crystal classes [52].

3.3 The Trigonal Systems

The primary piezoelectric material of interest is this dissertation is quartz and it is member of class 32, trigonal-trapezohedral. Quartz has a three-fold rotational symmetry on the *c* axis and a two-fold rotational symmetry on another axis. The commonly used system for quartz is the Bravais-Miller system; this system has four axes coordinate system as shown in Figure 3.1. According to the Bravais-Miller axial system, there are three equivalent secondary axes a_1, a_2, and a_3, lying 120 degrees apart in a plane normal to c. These axes are chosen as being either parallel to a two-fold axis or perpendicular to a plane of symmetry, or if there are neither two-fold axes perpendicular to c nor planes of symmetry parallel to c, the a axes are chosen so as to give the smallest unit cell.

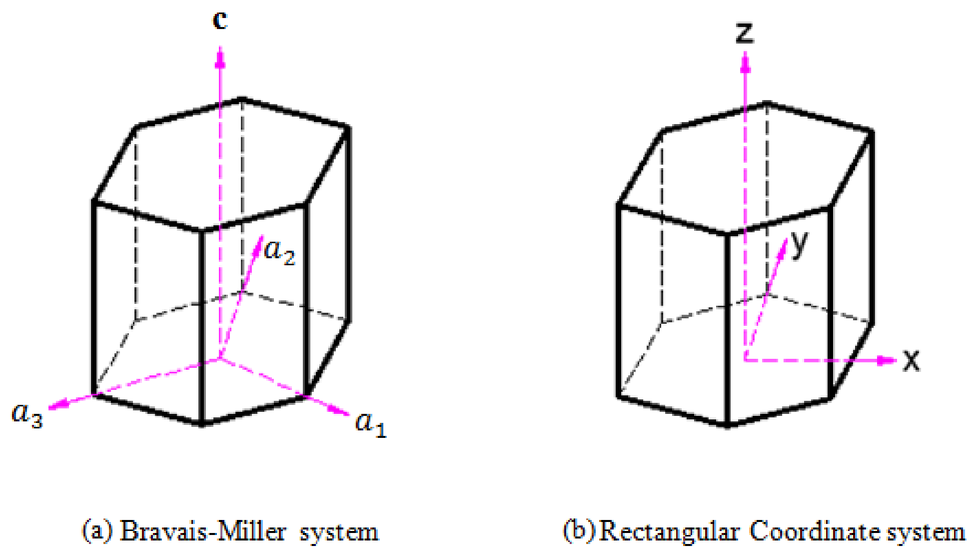

Figure 3.1: Bravais-Miller system of axis.

The Z axis is parallel to c. The X axis coincides in direction with any one of the a axes. The Y axis is perpendicular to both Z and X, so oriented to form a right handed system. Positive-sense rules for $+Z$, $+X$, and $+Y$ are listed in Table 3.3 for the trigonal and hexagonal crystals. To characterize a piezoelectric crystal, a set of piezoelectric constants is needed; and in order to clearly express them a sign convention is necessary for both the constants and the axis. There are two standards used in the literature: the IEEE 1978 standard and the IRE 1949 Standard, and the material properties take different forms within the two standards. The quartz material properties are commonly defined within the older 1949 IRE standard while other materials are usually defined using the 1978 IEEE standard. Crystallographic axes defined for quartz within the 1978 IEEE standard (solid lines) and 1949 standard (dashed lines). The conventions of this standard are shown in Figure 3.2 for right-handed and left-handed quartz. As a result, the signs of the material properties for both right-handed and left-handed quartz can change depending on the particular standard employed. Table 3.4 summaries the different signs that occur for the quartz material properties. Table 3.5 shows representative values of the constants in the elasto-piezo-dielectric matrices for right- and left-handed quartz in IEEE 1978 standard. A complete presentation of the elaso-piezo-dielectric matrix for all seven crystal and 32 point groups using Hermann-Mauguin's notation and Schoenflies's notation is shown in Table 3.6. The number of independent elastic constant range from 21 for triclinic crystal down to 3 for cubic crystal and the number of independent piezoelectric constant range from 18 down to zero for various point groups due to piezoelectric effect disappears for certain symmetry groups. The number of independent dielectric constant depends on the symmetry and range from 6 to 1 for various symmetry groups.

Class	+*Z*	+*X*	+*Y*
3	Positive d_{33}	Positive d_{11}	Form right-handed system
32	Arbitrary	Positive d_{11}	Form right-handed system
3*m*	Positive d_{33}	Form right-handed system	Positive d_{22}
6	Positive d_{33}	Arbitrary	Form right-handed system
	Form right-handed system	Positive d_{11}	Positive d_{22}
622	Arbitrary	Arbitrary	Form right-handed system
6*mm*	Positive d_{33}	Arbitrary	Form right-handed system
6*m*2	Arbitrary	Positive d_{11}	Form right-handed system

Table 3.3: Positive sense rules for *Z*, *X*, and *Y* for trigonal and hexagonal crystals [46].

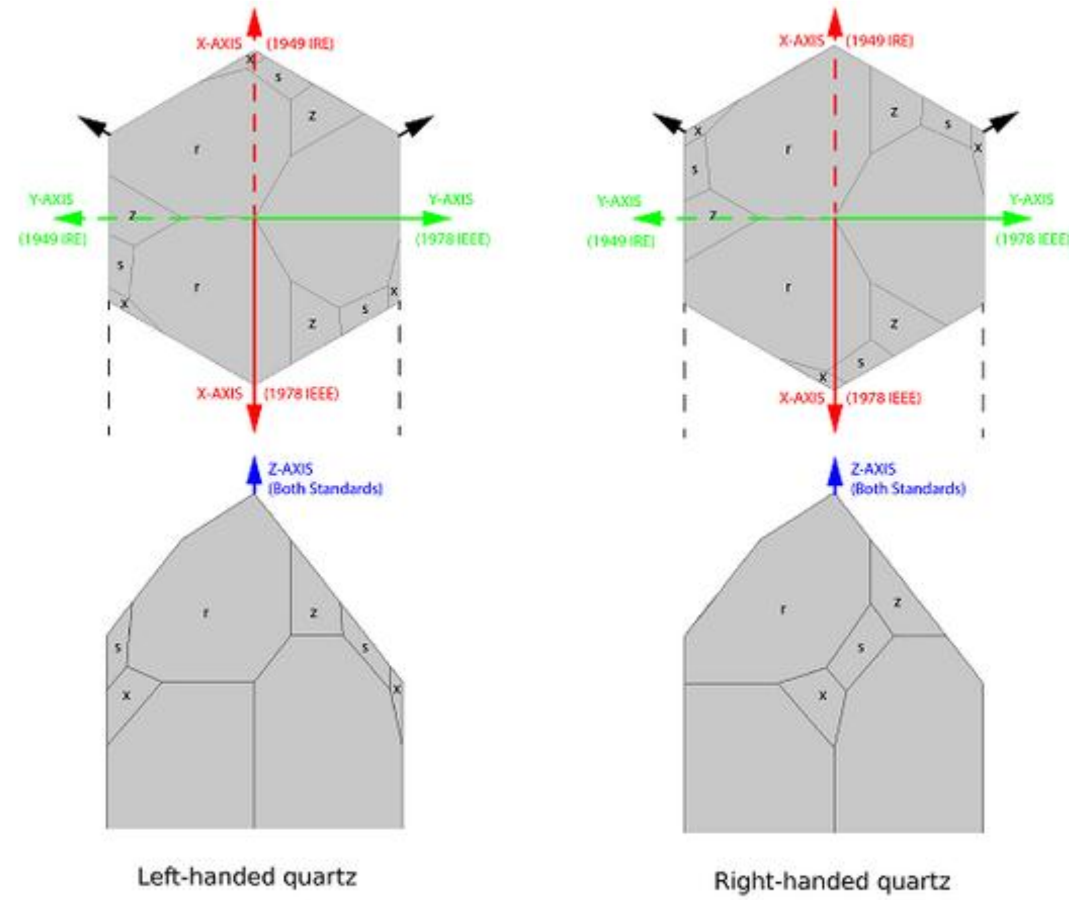

Figure 3.2: Left-handed and right handed quartz crystals [53].

	IRE 1949 Standard		IEEE 1978 Standard	
Material Property	Right-Handed Quartz	Left-Handed Quartz	Right-Handed Quartz	Left-Handed Quartz
s_{E14}	+	+	–	–
c_{E14}	–	–	+	+
d_{11}	–	+	+	–
d_{14}	–	+	–	+
e_{11}	–	+	+	–
e_{14}	+	–	+	–

Table 3.4: IRE 1949 standard and IEEE 1978 standard for right-handed and left-handed quartz [53].

General form of the matrices

$$\left(\begin{array}{c|c} c^E & e_t \\ \hline e & \epsilon^S \end{array}\right)$$

c^E in 10^9 Pa

e in 10^{-2} C/m^2

ϵ^S in 10^{-12} F/m

Right-handed quartz

$$\left(\begin{array}{cccccc|ccc}
86.74 & 6.99 & 11.91 & 17.91 & 0 & 0 & 17.1 & 0 & 0 \\
6.99 & 86.74 & 11.91 & -17.91 & 0 & 0 & -17.1 & 0 & 0 \\
11.91 & 11.91 & 107.2 & 0 & 0 & 0 & 0 & 0 & 0 \\
17.91 & -17.91 & 0 & 57.94 & 0 & 0 & 4.06 & 0 & 0 \\
0 & 0 & 0 & 0 & 57.94 & 17.91 & 0 & -4.06 & 0 \\
0 & 0 & 0 & 0 & 17.91 & 39.88 & 0 & -17.1 & 0 \\
\hline
17.1 & -17.1 & 0 & 4.06 & 0 & 0 & 39.21 & 0 & 0 \\
0 & 0 & 0 & 0 & -4.06 & -17.1 & 0 & 39.21 & 0 \\
0 & 0 & 0 & 0 & 0 & 0 & 0 & 0 & 41.03
\end{array}\right)$$

Left-handed quartz

$$\left(\begin{array}{cccccc|ccc}
86.74 & 6.99 & 11.91 & 17.91 & 0 & 0 & -17.1 & 0 & 0 \\
6.99 & 86.74 & 11.91 & -17.91 & 0 & 0 & 17.1 & 0 & 0 \\
11.91 & 11.91 & 107.2 & 0 & 0 & 0 & 0 & 0 & 0 \\
17.91 & -17.91 & 0 & 57.94 & 0 & 0 & -4.06 & 0 & 0 \\
0 & 0 & 0 & 0 & 57.94 & 17.91 & 0 & 4.06 & 0 \\
0 & 0 & 0 & 0 & 17.91 & 39.88 & 0 & 17.1 & 0 \\
\hline
-17.1 & 17.1 & 0 & -4.06 & 0 & 0 & 39.21 & 0 & 0 \\
0 & 0 & 0 & 0 & 4.06 & 17.1 & 0 & 39.21 & 0 \\
0 & 0 & 0 & 0 & 0 & 0 & 0 & 0 & 41.03
\end{array}\right)$$

Table 3.5: Elasto-piezo-dielectric matrices for right-handed and left-handed quartz IEEE 1978 standard [46]. (Errors in C_{55}, e_{24}, e_{25}, e_{26} have being corrected)

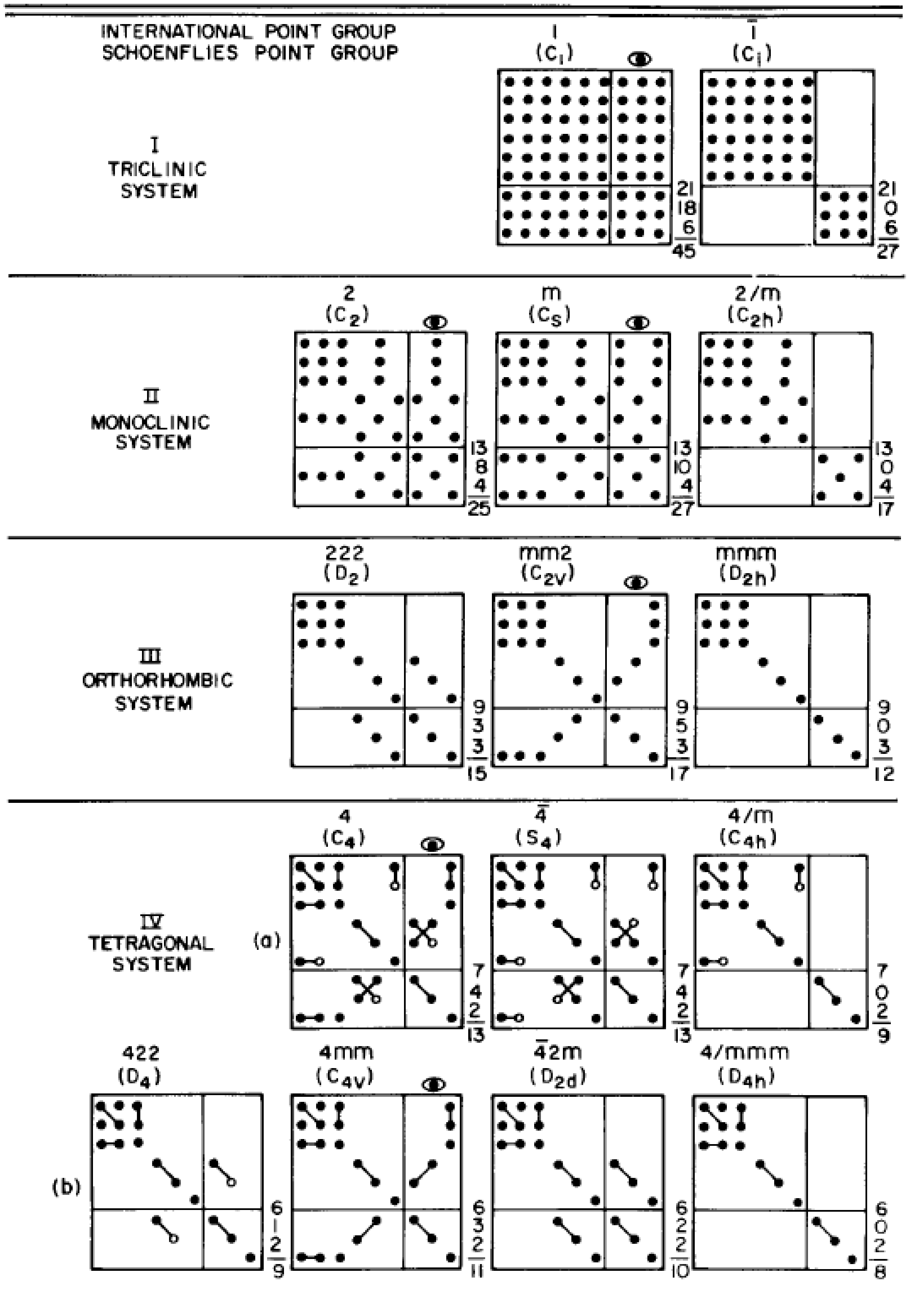
INTERNATIONAL POINT GROUP
SCHOENFLIES POINT GROUP
I
TRICLINIC
SYSTEM
1
(C_1)
$\bar{1}$
(C_i)
21
18
6
45
21
0
6
27
II
MONOCLINIC
SYSTEM
2
(C_2)
m
(C_s)
2/m
(C_{2h})
13
8
4
25
13
10
4
27
13
0
4
17
III
ORTHORHOMBIC
SYSTEM
222
(D_2)
mm2
(C_{2v})
mmm
(D_{2h})
9
3
3
15
9
5
3
17
9
0
3
12
IV
TETRAGONAL
SYSTEM
(a)
4
(C_4)
$\bar{4}$
(S_4)
4/m
(C_{4h})
7
4
2
13
7
4
2
13
7
0
2
9
(b)
422
(D_4)
4mm
(C_{4v})
$\bar{4}$2m
(D_{2d})
4/mmm
(D_{4h})
6
1
2
9
6
3
2
11
6
2
2
10
6
0
2
8

Continue;

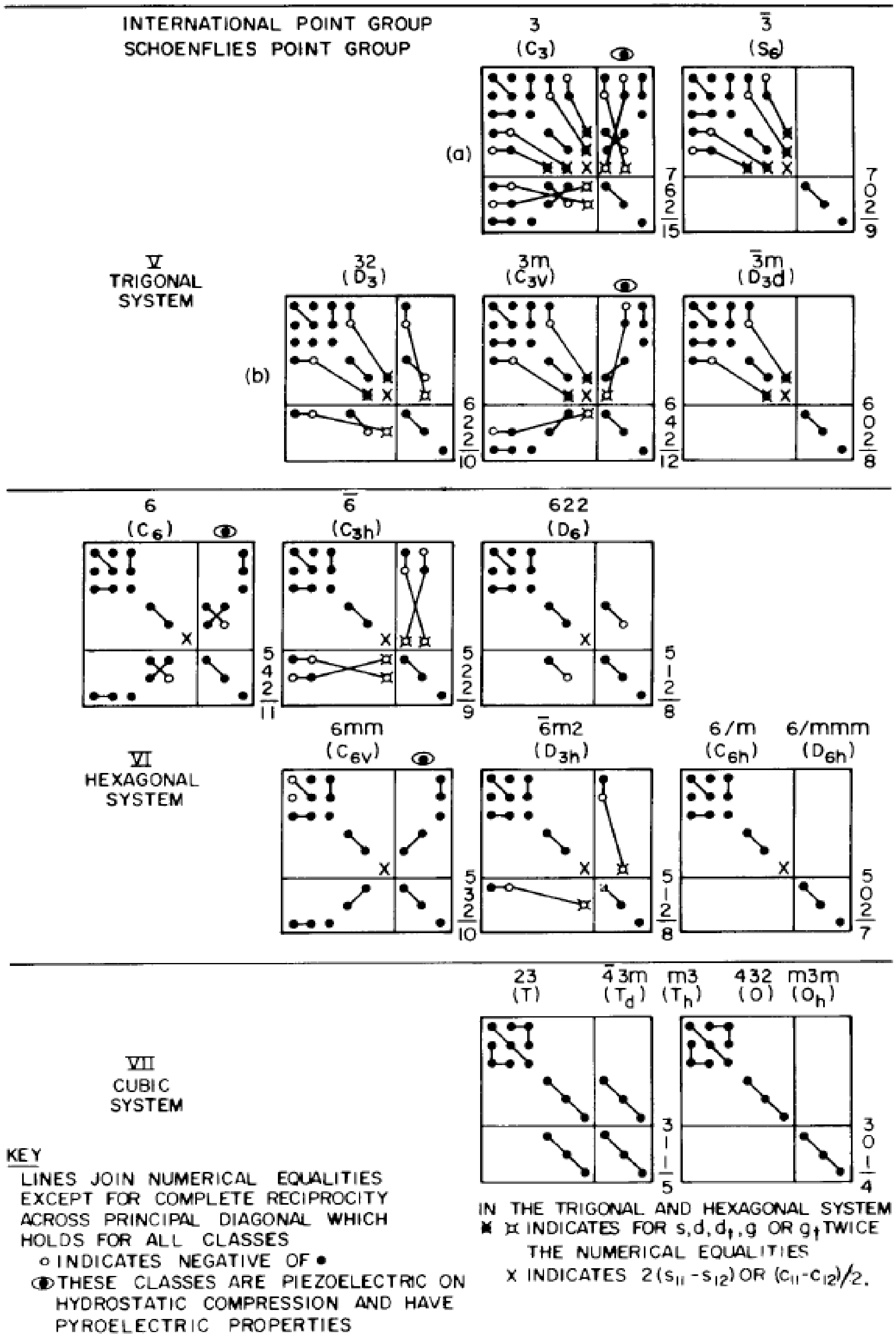

Table 3.6: Elasto-piezo-dielectric matrices for the 32 crystal classes [46].

3.4 Notation for the Orientation of Quartz Plates

A quartz crystal plate cut from a single-crystal staring material can have an arbitrary orientation relative to the three orthogonal crystal axes *X*, *Y*, and *Z*. The rotational symbol provides a method in which the plate of arbitrary orientation can be specified. The rotational symbol provides a starting reference for plates with thickness along *X*, *Y*, or *Z*, and then carries through successive rotations about coordinate axes, fixed in the reference plate, to reach the final orientation.

The orientation of the cut, with respect to the crystal axes, is specified by a series of rotations. The symbols l, w, and t denote the length, width and thickness of the plate. We use the notations l,w,t to denote the orthogonal coordinate axes fixed in the reference plate. The rotational symbol is defined by the convention that the first letter (*X*, *Y*, or *Z*) indicates the initial orientation of the thickness direction and the second letter (*X*, *Y*, or *Z*) indicates the initial orientation of the length direction. The remaining letters of the rotational symbol indicate the edge of the plate used as successive rotation axes. The third letter (l, w, or t) denotes which of the three orthogonal coordinate axes in the plate is the axis of the first rotation, the fourth letter (l, w, or t) is the axis of the second rotation, and the fifth letter (l, w, or t) the axis of third rotation. Consequently, if one rotation is needed to describe the final orientation of the plate, there are only three letters in the symbol, and if two rotations are needed, there are four letters in the symbol. Clearly, no more than five letters are ever needed to specify the most general orientation of a plate relative to the crystal axes by means of rotational symbol. The symbol is followed by a list of rotation angles Φ,Θ,Ψ, each angle corresponding to the successive rotation axes l, w, t. The specification of negative rotation angles consists of the magnitude of the angle preceded by a negative sign. An angle is positive if the rotation follows right handed rule. Thus an example of the rotation symbol for the most general type of rotation might be $(\mathrm{YX}lt)$ Φ/Ψ which means that initially the thickness and length of the plate are along the *Y* and *X* axes, respectively, the first rotation Φ= -51° is about l axis and the second rotation Ψ= -45° about t axis as shown in Figure 3.3.

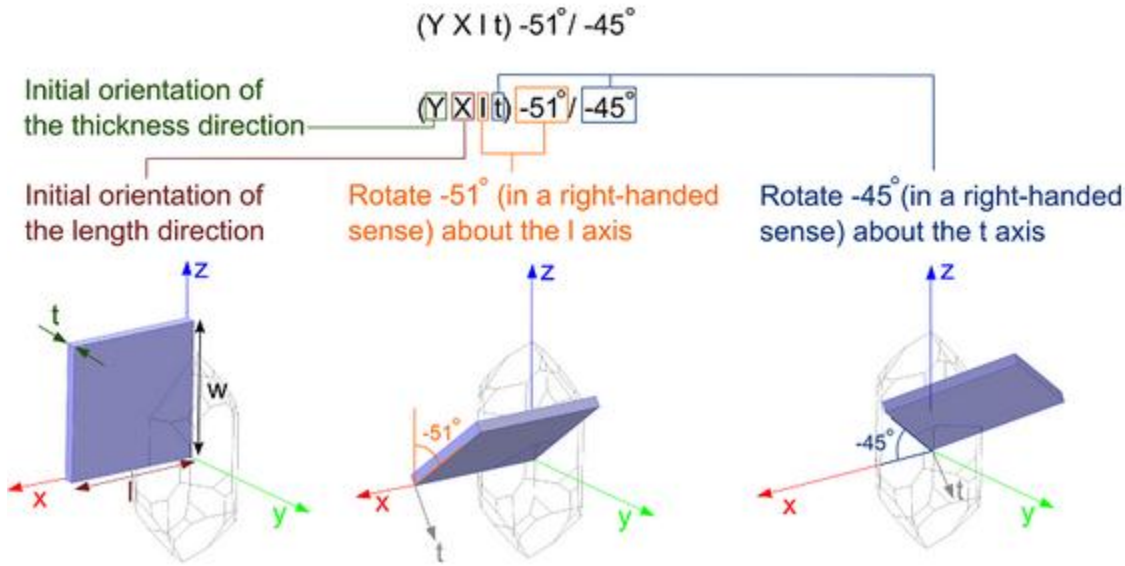

Figure 3.3: *GT*-cut quartz plate IEEE 1978 standard [53].

Most of the commonly used flexural and extensional mode quartz resonator may be obtained by a single rotation of the (*XY*) plate. The commonly used thickness-shear and face-shear mode (except the *SC*-cut) quartz resonator may be obtained by a single rotation of the (*YZ*) plate. Figures 3.4 and 3.5 show an example of a singly rotated *AT*-cut and *BT*-cut. For doubly rotated plate, the rotation symbol has four letters followed by two angles. Figure 3.6 shows an example of doubly rotated *SC*-cut quartz plate.

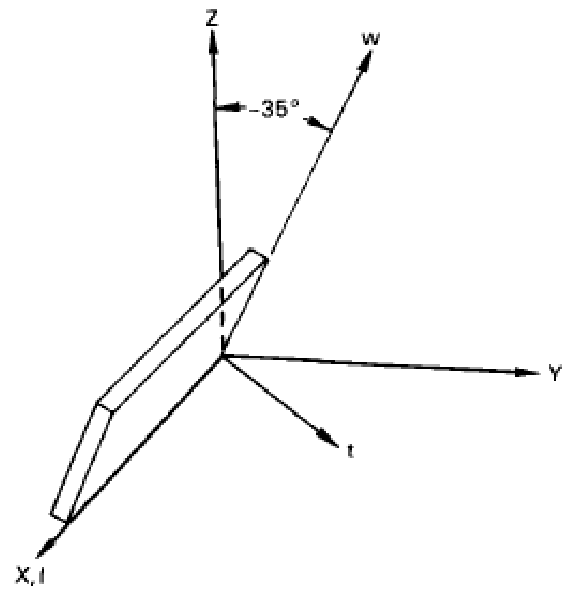

Figure 3.4: *AT*-cut quartz plate (YX*l*) -35˚ IEEE 1978 standard [46].

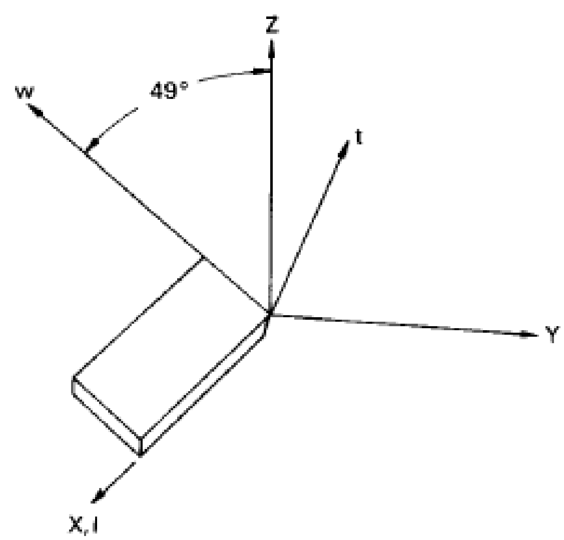

Figure 3.5: *BT*-cut quartz plate (YX*l*) 49˚ IEEE 1978 standard [46].

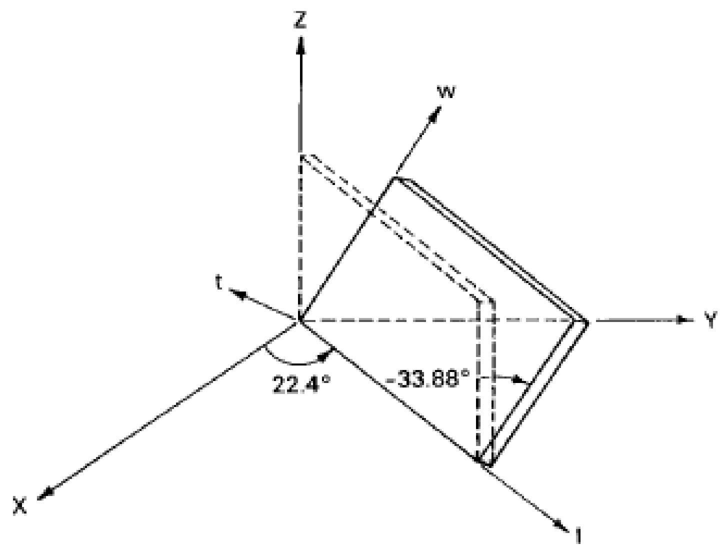

Figure 3.6: *SC*-cut quartz plate (YXwl) 22.4˚/ -33.88˚ IEEE 1978 standard [46].

3.5 Modes of Vibration

The vibration modes of the quartz crystal units are grouped into flexure, extension, face shear and thickness shear modes. The schematic of the vibration modes are shown in Figure 3.7. Properly oriented electrodes excite the desired mode of vibration, almost all quartz resonator use the thickness shear mode for high frequency applications. The fundamental frequency of thickness shear mode is inversely proportional to its thickness, the thinner the crystal; the higher the frequency is given by the expression:

$$f_n = {}^{nV}\!/_{2t} \qquad n = 1,3,5, \ldots. \tag{3.1}$$

where V is the wave speed and it is constant in a given medium, $2t$ is thickness of the plate. There are addition resonances at the 3rd, 5th etc. harmonic overtones whose frequencies are approximate but not exact odd multiples of the fundamental resonance frequency. In this dissertation, the thickness shear mode is the main mode of research that is used to study the nonlinear acceleration sensitivity and frequency-temperature behavior of quartz resonator.

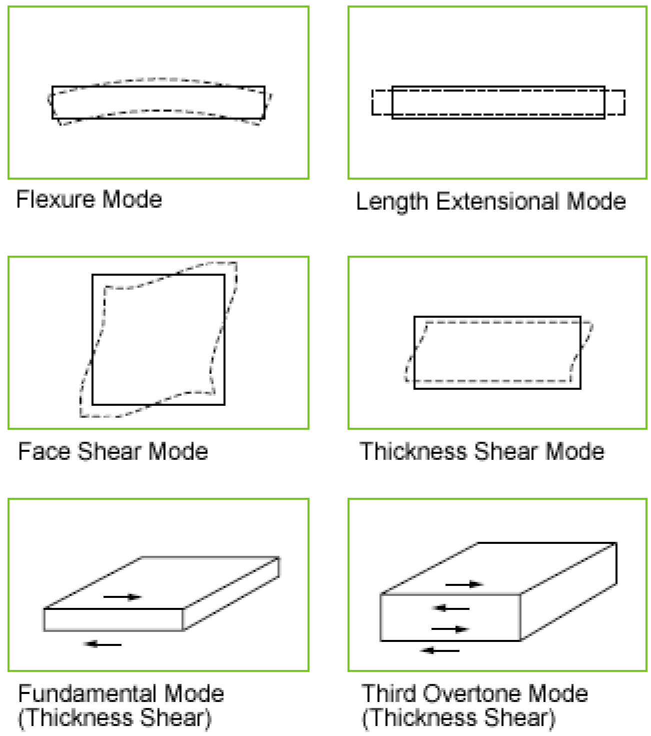

Figure 3.7: Modes of vibration of a quartz resonator.

3.6 Butterworth Van Dyke (BVD) Equivalent Circuit

The well-known Butterworth Van Dyke equivalent circuit used to represent a quartz resonator in the vicinity of the main mode of vibration is shown in Figure 3.8. The circuit is formed by two parallel branches: the static branch only contains capacitances C_0 represents the static capacitance of the electrodes. The motional branch C_1, L_1 and R_1 represent the electrical equivalent of the mechanically resonant mode. Here the motional inductance L_1 reflects the mass inertia, C_1 stands for elastic stiffness, and the resonance resistance R_1 describes the total damping of the resonance [54]. Away from the main mode there are other resonances that can be similarly represented by the parallel addition of motion arms.

C_0: The shunt capacitance of a crystal is due in part to the thickness of the wafer. This is the measure capacitance while not vibrating.

C_1: The motional capacitance of a crystal is determined by the stiffness of the quartz. As a general rule, if a fundamental design is used on an overtone, the C_1 will divide by the square of the overtone.

L_1: The motional inductance of the crystal is determined by the mechanical mass of quartz in motion. The L_1 and C_1 are related by Thomson's formula:

$$L_1 = {}^{1}/_{(4\pi^2 f^2 C_1)}. \quad (3.2)$$

R_1: The motional resistance of the crystal is determined by the internal loss of the mechanical vibrating system of the crystal.

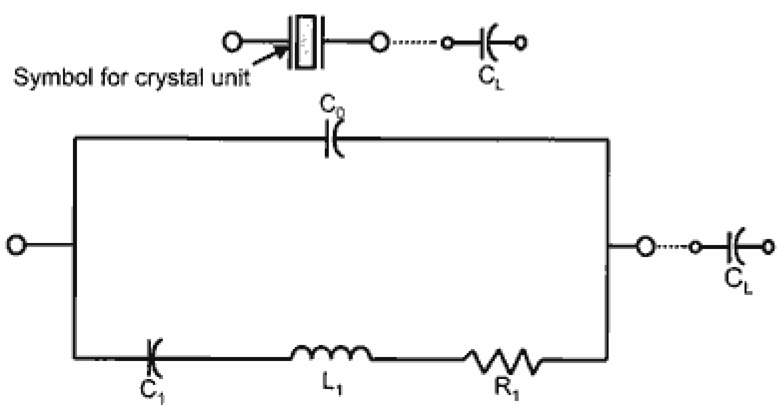

Figure 3.8: Butterworth Van Dyke equivalent circuit of piezoelectric resonator [55].

The BVD equivalent parameters are obtained from finite element eigenvalue analysis. The static capacitance C_0 is obtained from electrostatic analysis by applying 1 volt of DC voltage on the driving electrodes, and then the total surface charge accumulated on the driving electrode is the static capacitance C_0. The electrical parameters C_1, L_1 and R_1 can be obtained from the eigenvalue analysis.

ω_R: is the real part of resonance frequency.

ω_I: is the imaginary part of resonance frequency.

q: is the total surface charge.

E_{kin}: is the kinetic energy.

Q: is the quality factor.

Y: is the admittance of the equivalent circuit.

$$q = \left|\int_{electrode} D \, dA\right|, \tag{3.3}$$

$$E_{kin} = {\omega_R^2}/{2} \int_V \rho |u|^2 \, dV, \tag{3.4}$$

$$Q = {\omega_R}/{2\omega_I}, \tag{3.5}$$

$$C_1 = {q^2}/{E_{kin}}, \tag{3.6}$$

$$L_1 = {1}/{(\omega_R^2 C_1)}, \tag{3.7}$$

$$R_1 = {1}/{(\omega_R C_1 Q)}, \tag{3.8}$$

$$Y(\omega_R) = j\omega_R C_0 + {1}/{(R_1 + j\omega_R L_1 + 1/j\omega_R C_1)}. \tag{3.9}$$

The capacitance ratio C_0/C_1 is a measure of the inter-conversion between electrical energy and mechanical energy stored in the crystal, i.e. piezoelectric coupling factor k.

$$k^2 = {(n\pi)^2 \, C_1}/{8C_0} \qquad n = 1,3,5,\ldots \tag{3.10}$$

The piezoelectric coupling factor is about 8.8% for *AT*-cut and 4.99% for *SC*-cut. When a dc voltage is applied to the electrodes of a resonator, the capacitance ratio C_0/C_1 is a measure of the ratio of electrical energy stored in the capacitor formed by the electrodes to the energy stored elastically in the crystal due to the lattice strains produced by the piezoelectric effect.

The use of load capacitor C_L in series or parallel to the crystal shifts the working frequency of the crystal by an amount depending upon the value of C_L and the value C_0 and C_1. Figure 3.9 show the series and parallel connections respectively.

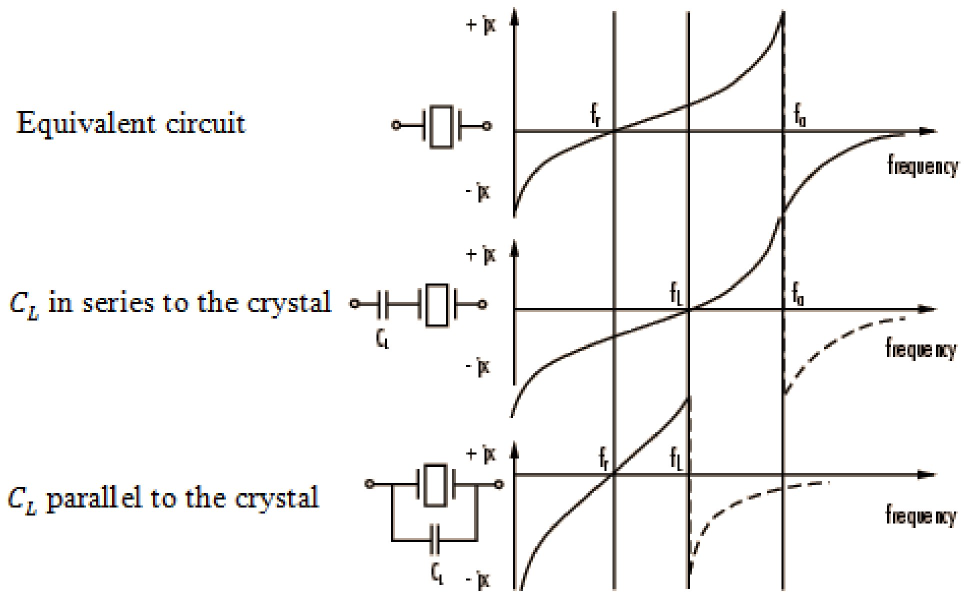

Figure 3.9: Series and parallel connection.

When C_L is in series to the crystal, f_a is not affected but f_r moves up to a frequency f_L. When C_L is parallel to the crystal, the resonance frequency f_r is not affected but the anti-resonance f_a shifts down to the frequency f_L. When a load capacitor is connected in series with the crystal, f_L can be obtained by:

$$f_L = f_r + f_r\left({}^{C_1}/_{2(C_0 + C_L)}\right), \tag{3.11}$$

$$^{\Delta f}/_{f_r} = {}^{C_1}/_{2(C_0 + C_L)}. \tag{3.12}$$

A load capacitor C_L changes not only the frequency, but also the frequency vs. temperature characteristic. Figure 3.10 shown the f vs. T characteristic of the same resonator with and without a C_L. The load capacitor rotates the f vs. T curve counter-clockwise. Table 3.7 shows the calculated equivalent circuit parameters for the 1 GHz *AT*-cut resonator.

Frequency (GHz)	1.048809
C_1 (F)	1.0876E-15
R_1 (Ω)	10.8394
C_0 (F)	2.0237E -13
L_1 (H)	2.1172E-5

Table 3.7: Equivalent circuit parameters for the 1 GHz *AT*-cut resonator.

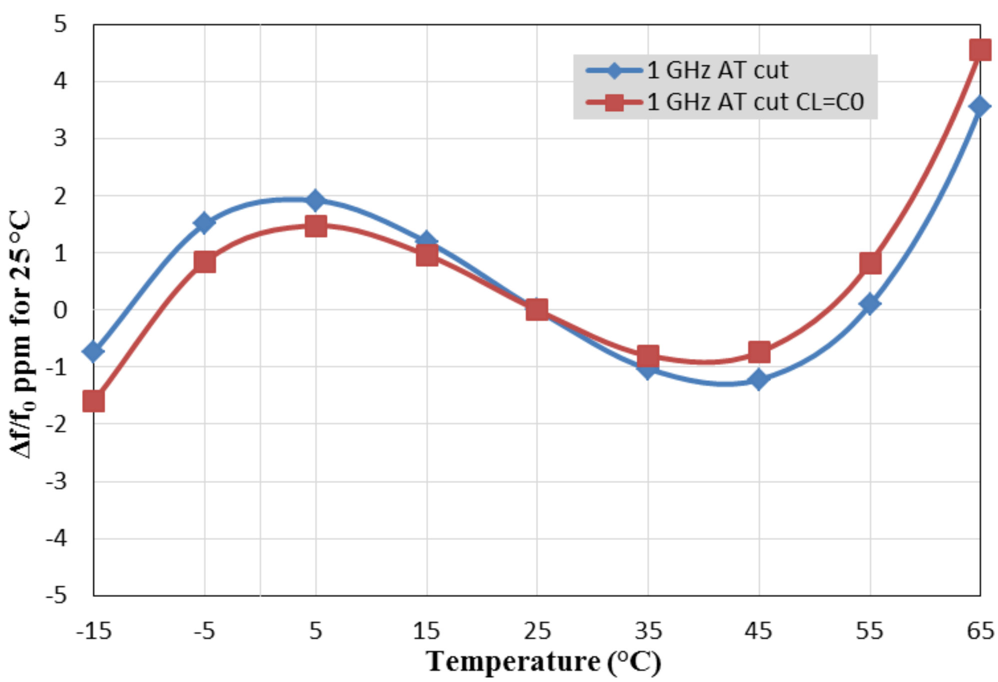

Figure 3.10: Effect of load capacitance on f vs. T for 1 GHz resonator.

Chapter 4 Acceleration Sensitivity in Quartz Resonators

4.1 Introduction

Acceleration sensitivity remains one of the most complicated and difficult problems faced by resonator designers, for example in sophisticated communication systems. Many modern communication systems operate on mobile platforms such as helicopters, unmanned air vehicles and fighter jets, and satellites. When quartz resonators operate on mobile platforms, the effects of vibration induced phase noise is typically greater than all the other noise sources. The quartz resonator then becomes the most acceleration sensitive component in frequency sources [56]. A reduction in acceleration sensitivity from 10^{-10}/g to 10^{-12}/g is needed in order to maintain purity of signals in modern communications and navigation systems [57].

Piezoelectric quartz resonators are high *Q* mechanical vibrators that operate at a specific resonant frequency. The resonant frequency is affected by certain external factors including external force fields, and acceleration that cause initial deformations of the crystal. When a piezoelectric quartz crystal is subjected to external fields such as gravitational fields, the resulting quasi-static stresses and strains on the crystal cause the natural resonant frequency to shift [58]. Frequency shift in acceleration occurs primarily as a result of resonator deformation due to constrained supports (ex. resonator cantilever mounted). The initial deformations distort the quartz plate and the nonlinear elastic behaviors change the acoustic wave velocity [59]. The frequency of a resonator is function of wave velocity and thickness of quartz plate, any small change on the plate dimensions or propagation of wave velocity in the anisotropic medium will cause a frequency shift.

In this chapter we (1) formulate the piezoelectric incremental equations for small deformations superposed on finite deformations; (2) verify the accuracy of the piezoelectric incremental equations using COMSOL FEA by comparing the results on the effects of a pair of diametrical forces on circular *AT*-cut quartz resonators with experimental data, (3) perform a detailed study of the cantilevered rectangular *AT*-cut quartz plate resonator to determine the factors that influence acceleration sensitivity and (4) propose using two pairs of electrodes along the plate edges in order to reduce bending and hence acceleration sensitivity. Our study is based on two UHF resonators at nominal frequencies of 500 MHz and 1 GHz respectively.

4.2 Equations of Piezoelectricity for Small Deformation Superposed on Finite Deformations

Piezoelectric equations for small deformations superposed on finite deformations are needed for the study of active reduction of acceleration sensitivity. The active reduction of acceleration sensitivity in quartz resonators uses electric fields to create countervailing forces on the quartz plate to reduce the initial strains caused by acceleration. The nonlinear piezoelectric equations derived in chapter 2 in Lagrangian formulation was employed at the final and initial state, respectively. The process of superposing small vibrations on acceleration-induced deformations due to body force in a crystal can be described by three consecutive states shown in Figure 4.1. By taking the difference of the field equations between the final state and the initial state, a set of piezoelectric incremental field equations for small vibrations superposed on initial deformations are obtained.

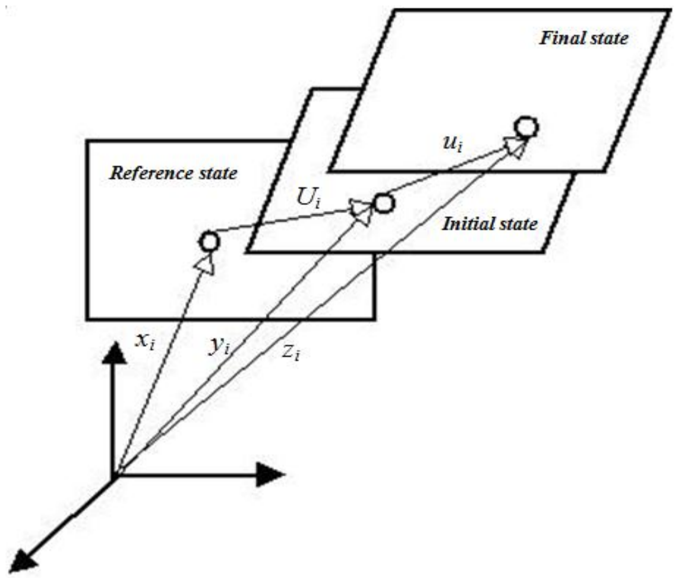

Figure 4.1: Position vector of a material point at reference, initial and final states.

1)*Reference State:*

The crystal is in an undeformed state in which material particles are stationary and experience no displacement, strain and stress. The crystal is also free of electric fields with reference to a rectangular Cartesian frame.

2) *Initial State*:

In this state the crystal is deformed under the action of body force and carries static electric fields (biasing fields). The position of the material particles are moved due to acceleration from x_i to y_i. The nonlinear equations of the initial state in Lagrangian formulation are as follow:

Initial displacements:

$$U_i = y_i - x_i, \tag{4.1}$$

Initial strains:

$$S_{ij} = \frac{1}{2}(U_{i,j} + U_{j,i} + U_{k,i}U_{k,j}), \tag{4.2}$$

Initial stresses (Piola Kirchhoff 2nd kind):

$$T_{ij} = C^E_{ijkl} S_{kl} + \tfrac{1}{2} C^E_{ijklmn} S_{kl} S_{mn} - e_{kij} E_k, \tag{4.3}$$

Initial electric displacements:

$$D_i = e_{ikl} S_{kl} + \varepsilon^S_{ik} E_k, \tag{4.4}$$

Initial stress equations of motion:

$$(T_{ij} + T_{jk} U_{i,k})_{,j} + \rho B_i = \rho \ddot{U}_i \quad \text{in } V, \tag{4.5}$$

Initial charge equations of motion:

$$D_{i,i} = 0 \quad \text{in } V, \tag{4.6}$$

where C^E_{ijkl} and C^E_{ijklmn} are second and third order elastic constants of quartz, e_{kij} is the piezoelectric constants, ε^S_{ik} is the electrical permittivity, E_k is the electric field, ρ is the mass density at reference room temperature and B_i is the body force.

3) *Final State*:

In this state the crystal is subjected to small incremental deformations and electric fields in addition to the initial deformations imposed in the initial state. The position of the material particles are further displaced from y_i to z_i. All the total fields in the final state are to be denoted by the "barred" quantities. The nonlinear equations for the final state in Lagrangian formulation are as follow:

Final displacements:

$$\bar{U} = z_i - x_i, \tag{4.7}$$

Final strains:

$$\bar{S}_{ij} = \tfrac{1}{2}(\bar{U}_{i,j} + \bar{U}_{j,i} + \bar{U}_{k,i} \bar{U}_{k,j}), \tag{4.8}$$

Final stresses (Piola-Kirchhoff 2nd kind):

$$\bar{T}_{ij} = C^E_{ijkl} \bar{S}_{kl} + \tfrac{1}{2} C^E_{ijklmn} \bar{S}_{kl} \bar{S}_{mn} - e_{kij} \bar{E}_k, \tag{4.9}$$

Final electric displacements:

$$\bar{D}_i = e_{ikl}\bar{S}_{kl} + \varepsilon^S_{ik}\bar{E}_k, \tag{4.10}$$

Final stress equations of motion:

$$(\bar{T}_{ij} + \bar{T}_{jk}\bar{U}_{i,k})_{,j} + \rho\bar{B}_i = \rho\ddot{\bar{U}}_i \quad \text{in } V, \tag{4.11}$$

Final charge equations of motion:

$$\bar{D}_{i,i} = 0 \quad \text{in } V. \tag{4.12}$$

Piezoelectric incremental field equations due to small amplitude vibrations are obtained by taking the difference between the final state and the initial state. They are shown in Table 4.1. This set of equations is linear when the initial state is known.

	Final (present state)	***Initial (initial state)***	***Incremental (difference)***
Displacement	$\bar{U}_i = z_i - x_i$	$U_i = y_i - x_i$	$u_i = \bar{U}_i - U_i$
Strain	$\bar{S}_{ij}$	S_{ij}	$s_{ij} = \bar{S}_{ij} - S_{ij}$
2nd PK. stress	$\bar{T}_{ij}$	T_{ij}	$t_{ij} = \bar{T}_{ij} - T_{ij}$
Body force	$\bar{B}_i$	B_i	$b_i = \bar{B}_i - B_i$
Electric field	$\bar{E}_k$	E_k	$e_k = \bar{E}_k - E_k$
Electric disp.	$\bar{D}_i$	D_i	$d_i = \bar{D}_i - D_i$

Table 4.1: Incremental piezoelectric equations.

Incremental displacements:

$$u_i = \bar{U}_i - U_i, \tag{4.13}$$

Incremental strains:

$$s_{ij} = \tfrac{1}{2}(u_{i,j} + u_{j,i} + U_{k,i}u_{k,j} + U_{k,j}u_{k,i}), \tag{4.14}$$

Incremental stresses:

$$t_{ij} = \left(C^E_{ijkl} + C^E_{ijklmn}S_{mn}\right)s_{kl} - e_{kij}e_k, \tag{4.15}$$

Incremental electric displacements:

$$d_i = e_{ikl}s_{kl} + \varepsilon_{ik}^S e_k, \tag{4.16}$$

Incremental stress equations of motion:

$$(t_{ij} + t_{jk}U_{i,k})_{,j} + \rho b_i = \rho \ddot{u}_i \ \text{ in } V, \tag{4.17}$$

Incremental charge equations of motion:

$$d_{i,i} = 0 \ \text{ in } V. \tag{4.18}$$

In equations (4.14) and (4.15), higher order terms $u_{k,i}\, u_{k,j}$ and $s_{kl}\, s_{mn}$ are neglected as compared to the first order term $u_{k,i}$ and s_{kl} for small amplitude vibrations. These equations are used to study the acceleration sensitivity of quartz crystal resonators.

A similar set of incremental piezoelectric equations by Tiersten, Yang [60], and others uses the Piola-Kirchhoff stress tensor of the first kind. Because the piezoelectric equations in COMSOL are defined in terms of Piola-Kirchhoff of the second kind, it was easier to implement the incremental piezoelectric equations in Piola-Kirchhoff of the second kind.

4.3 Comparison of Measured Data with 3-D Finite Element Model Using the Piezoelectric Incremental Equations

The accuracy and validation of the piezoelectric incremental field equations (Eqns. (4.13)-(4.18)) in Lagrangian formulation is established by comparing a 3-D finite element model (FEA) results with the experiment results by Ballato [37] and Mingins [26]. In reference [37], an *AT* cut circular disk of diameter *d* and thickness *2b*, is subjected to a pair of diametrical forces *F* at an angle ψ (azimuth angle) with the X_1-axis as shown in Figure 4.2.

The resonator plate dimensions modeled are from Fletcher and Douglas's experimental setup [38] with d = 12mm, centered silver electrodes of diameter 4mm with thickness giving a relative frequency change due to mass loading of 0.5% and ψ varying from 0 ° to 90 °. The relative magnitude of the mass loading is expressed in terms of the ratio R, which is the electrode mass per unit area to the mass per unit area of the resonator

$$R = {}^{\rho_e t_e}/_{\rho_s h}, \tag{4.19}$$

where ρ_e and t_e are the density and thickness of electrode, and ρ_s and h are the density and thickness of quartz plate. The fundamental thickness shear mode is considered. In FEA simulations, equivalent boundary conditions are used due to difficulty in achieving perfectly symmetric forces during meshing. The plate is fixed at one edge, with compressive force F on the opposite edge with prescribed displacements $u_y = u_z = 0$ shown in Figure 4.3. These equivalent boundary conditions have the same effects as the pair of diametrical compressive forces shown in Figure 4.2.

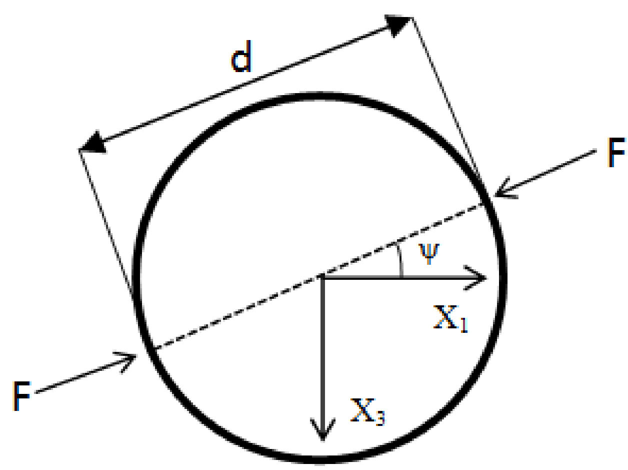

Figure 4.2: Experimental setup of circular disk subjected to diametrical forces [37].

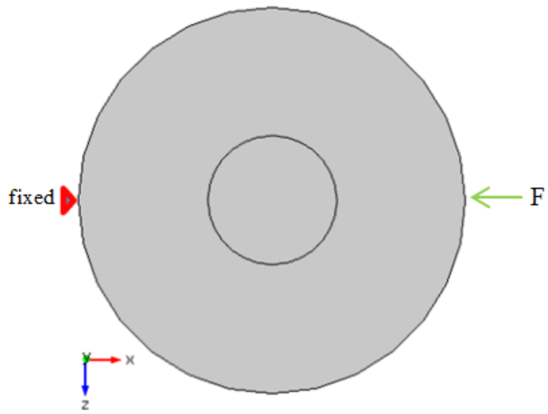

Figure 4.3: Finite element mode of *AT*-cut with diameter 12mm, thickness 0.1655mm, and electrode diameter 4mm, thickness 1045Å.

The results of frequency change were computed according to Ratajski's force sensitivity coefficient, K_f [61],

$$K_f = \left(\frac{\Delta f}{f_0} \times \frac{1}{F}\right)\frac{d}{f_0}. \tag{4.20}$$

The force sensitivity coefficient as a function of the azimuth angle ψ were computed using FEA for the Fletcher and Douglas [38] plate, and compared with the measured results of Ballato [37] and Mingins et al. [26]. The results are shown in Figures 4.4 and 4.6 for the *AT*-cut and *BT*-cut, respectively. In Figure 4.4 the solid blue line is the FEA model result which compares well with the measured results of [37].

In Figure 4.6, according to Ballato [37], the authors did not specify whether the measured results for the *BT*-cut plate were for the slow or fast shear mode shown in Figure 4.5 when the azimuth angle ψ was varied from 0^{o} to 90^{o}. Therefore we show our model results for both the slow shear mode (purple line) and fast shear mode (blue line). Our model results for the slow shear mode (purple line) compare well with the measured results for angles $\psi = 0^{o}$ to 70^{o}. From 70^{o} to 90^{o} the measured results fall between our model results for slow and fast shear modes. In summary, Figures 4.4 and 4.6 validate our FEA model that employs the piezoelectric incremental equations for small vibrations superposed on initial deformations.

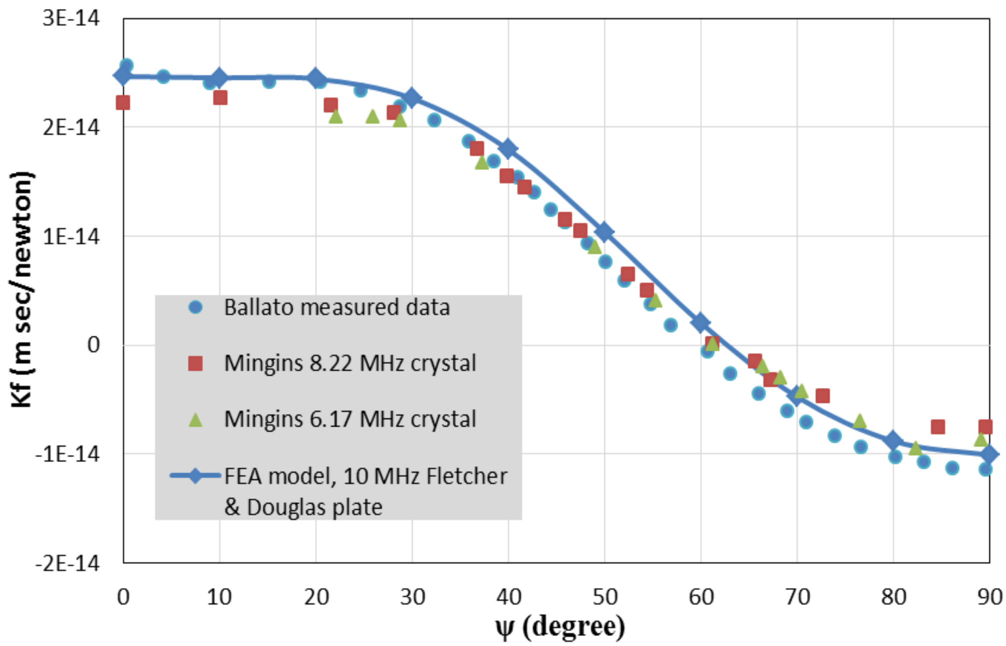

Figure 4.4: Comparison of force sensitivity coefficient K_f as a function of the azimuth angle ψ for *AT*-cut (θ= 35.25 °) with measured data by Ballato [37] and Mingins [26].

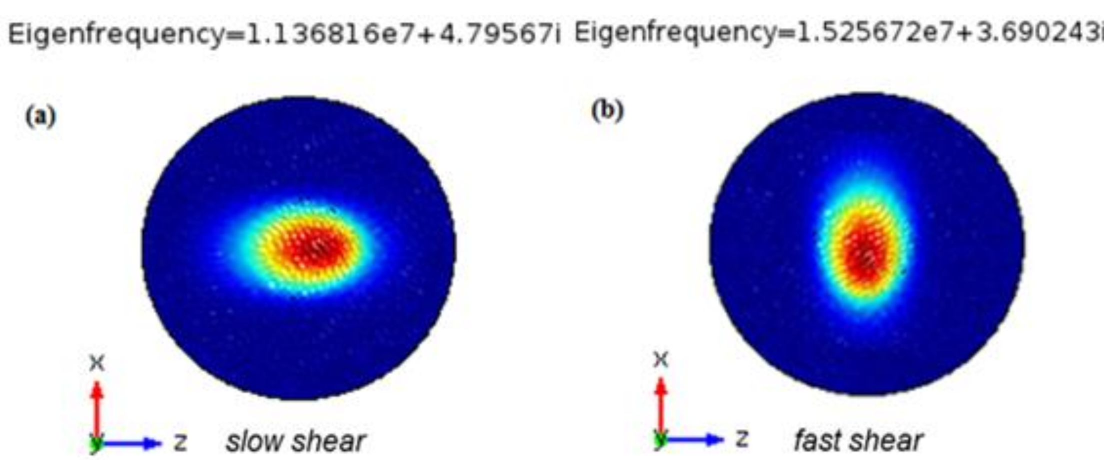

Figure 4.5: (a) *BT*-cut slow shear, (b) *BT*-cut fast shear.

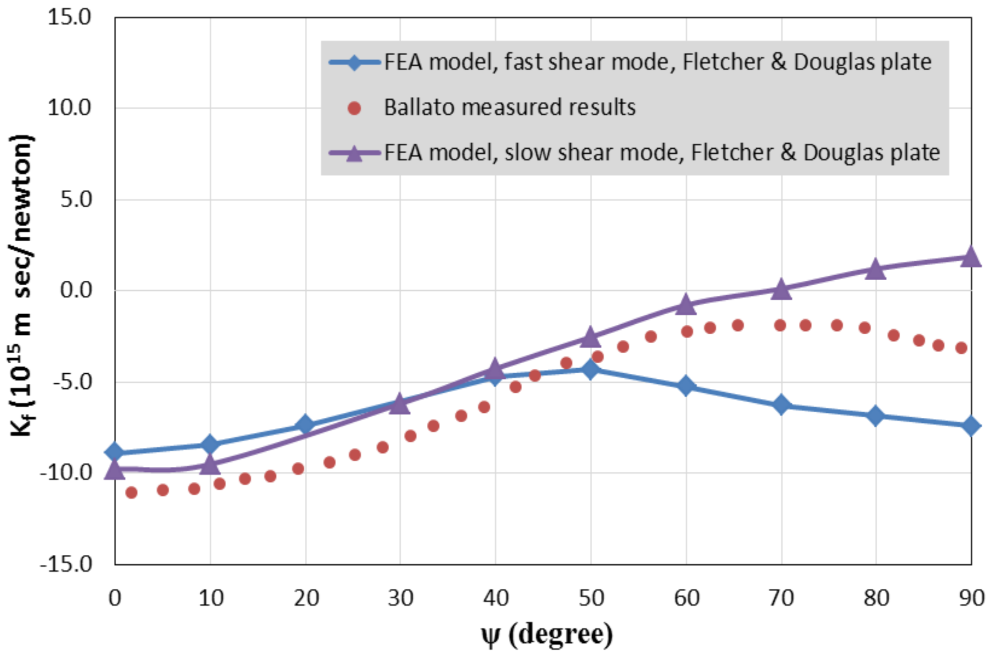

Figure 4.6: Comparison of force sensitivity coefficient K_f as a function of the azimuth angle ψ for *BT*-cut (θ= -49 °) with measured data by Ballato [37] .

4.4 The Acceleration Effect Due to Body Forces on Quartz Resonators

The use of finite element model has great flexibility in analyzing acceleration sensitivity due to body force. We study two rectangular *AT*-cut quartz resonators with frequencies of 1 GHz and 500 MHz respectively. Figure 4.7 shows a rectangular 1GHz *AT*-cut quartz plate resonator (*l*=235µm, *w*=105µm, *t*=1.5µm) with aluminum electrodes (150x50x0.04µm). The 500 MHz *AT* cut quartz plate resonator has plate dimensions *l*=470µm, *w*=210µm, *t*=3µm and aluminum electrode dimensions (300x100x0.08µm), maintaining the same aspect ratio (length to thickness and width ratios) as the 1 GHz resonator plate. The electrode is treated as added mass per unit area determined by the density of aluminum and thickness of the electrodes. Both resonators were cantilever mounted on one edge and subjected to g body force in the Y-axis direction and in the X-Z plane. Let define Γ as the acceleration sensitivity vector:

$$\Gamma = \sqrt{\Gamma_{Out}^2 + \Gamma_{In}^2}\,, \tag{4.21}$$

where Γ is the total acceleration sensitivity (per g), Γ_{Out} and Γ_{In} are respectively, the components of out-of-plane and in-plane acceleration sensitivity.

The fractional change of frequency $\Delta f/f_0$ is computed for the plate resonator as a function of the azimuth angles ψ_1 and ψ_2. The azimuth angle ψ_1 is the angle between the crystal digonal X-axis and plate X-axis, while the azimuth angle ψ_2 is the angle of the in-plane body force with the plate X-axis, as in Figure 4.7. The resonant mode used is the fundamental thickness shear mode shown in Figure 4.8.

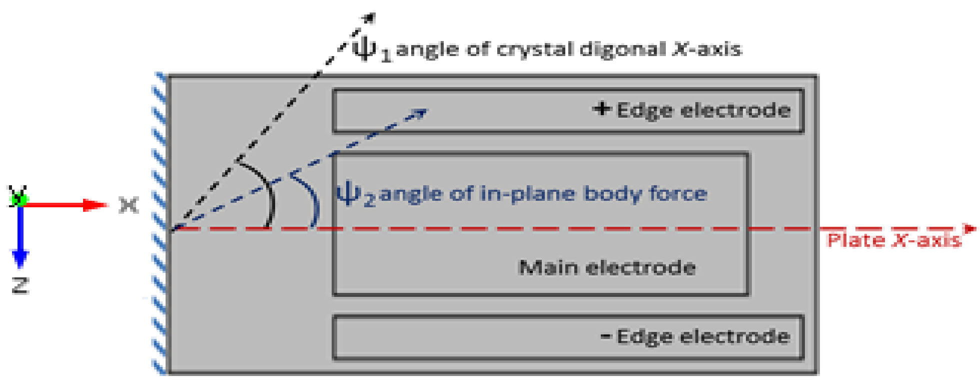

Figure 4.7: Rectangular 1 GHz AT-cut plate, cantilever mounted. ψ_1 is the angle of the crystal digonal X-axis with the plate X-axis. ψ_2 is the angle of the in-plane body force with the plate X-axis.

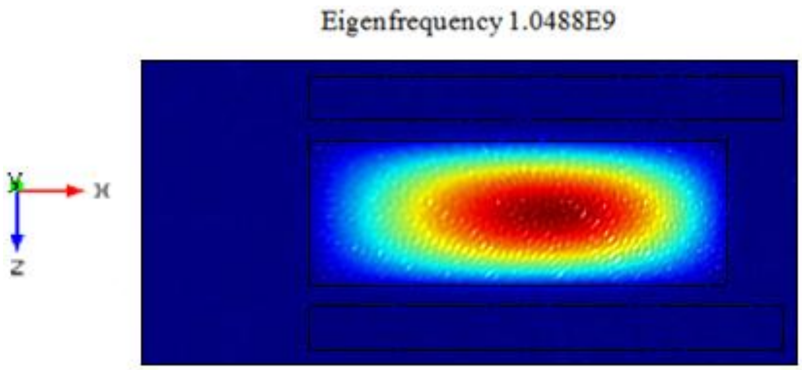

Figure 4.8: Fundamental thickness shear mode of 1 GHz *AT*-cut quartz plate, $f_0 = 1.0488$ GHz.

4.4.1 Effects of out-of-plane Body Force (g Body Force in the Y-axis direction)

To study the effects of g body force in the out-of-plane Y-axis direction, the fractional frequency change $\Delta f/f_0$ is computed for both positive and negative 1 g body force for the 1 GHz resonator (blue and red lines) and the 500 MHz resonator (green and purple lines) respectively in Figure 4.9. We observed that the acceleration sensitivity is 'rectified' when $\psi_1 = 0^o$ and 180^o, that is, $\Delta f/f_0$ was always positive regardless of the sign of the body force. The maximum acceleration sensitivity occurred at ψ_1 equal 90^o and 270^o. The magnitude of fractional change of frequency for the 500 MHz resonator is about twice as the 1 GHz resonator and this is in line with Kosinski's [62] finding that there is a net $\frac{1}{f}$ dependence of the acceleration sensitivity for plates with the same aspect ratios, that is, the higher the resonator frequency, the lower the acceleration sensitivity. Although Kosinski's finding has not been proved experimentally, our FEA simulations shown good agreement with his finding.

The acceleration sensitivity due to Y-axis g body force was further analyzed with respect to the magnitude and sign of the body force shown in Figures 4.10 and 4.11 for the 1 GHz and 500MHz plates respectively. When ψ_1 = 0^o the acceleration sensitivity is a nonlinear parabolic curve (blue line). As the angle ψ_1 is increased from 0^o to 45^o and 90^o, the acceleration sensitivity as a function of body force *g* becomes increasingly linear as shown by the red line (ψ_1 = 45^o) and green line (ψ_1 = 90^o) for both the 1 GHz and 500 MHz plates. This linear relationship between the acceleration sensitivity and the body force *g* at ψ_1 = 90^o is very useful for the practical application of a DC bias to reduce or control acceleration sensitivity.

Regarding ψ_1 dependence of active reduction of acceleration sensitivity, note that when ψ_1 = 0^o the acceleration sensitivity is rectified (blue curve) and therefore it is not possible to use active reduction of acceleration sensitivity because the plate is insensitive to the sign of the DC bias. Also for large body forces (>-30 *g* for the 1 GHz plate and >-20 *g* for the 500 MHz plate) the rectified acceleration sensitivity (ψ_1 = 0^o) is greater than the acceleration sensitivity for ψ_1 = 90^o.

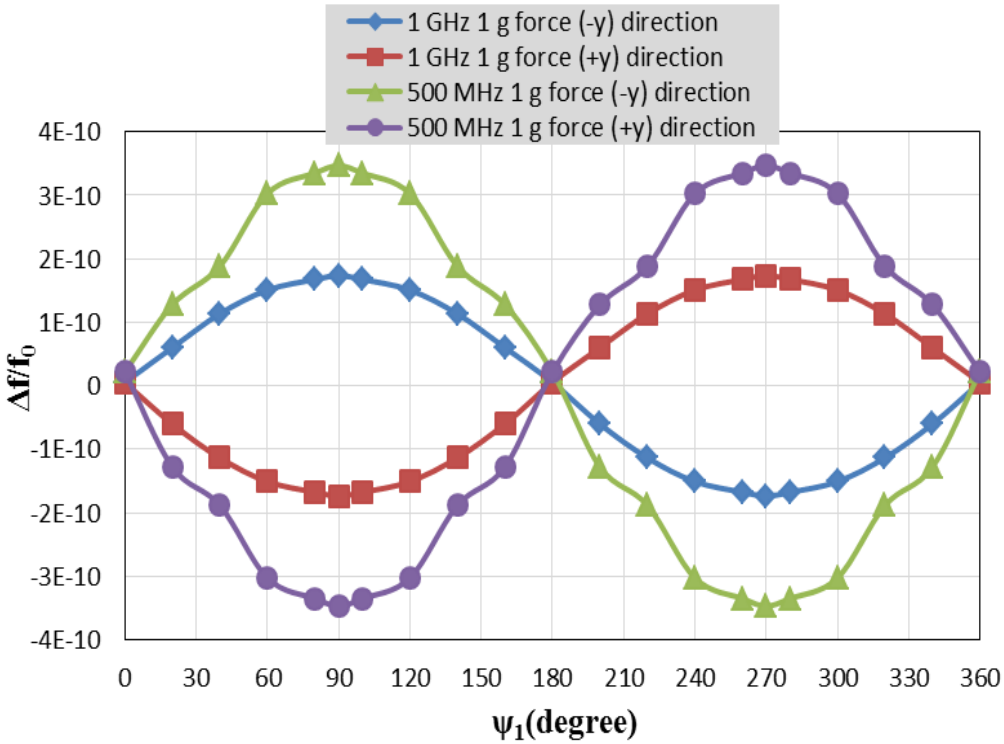

Figure 4.9: Frequency change as a function of azimuth angle ψ_1 for the 1 GHz and 500 MHz *AT*-cut rectangular plates for 1 *g* out-of-plane body force.

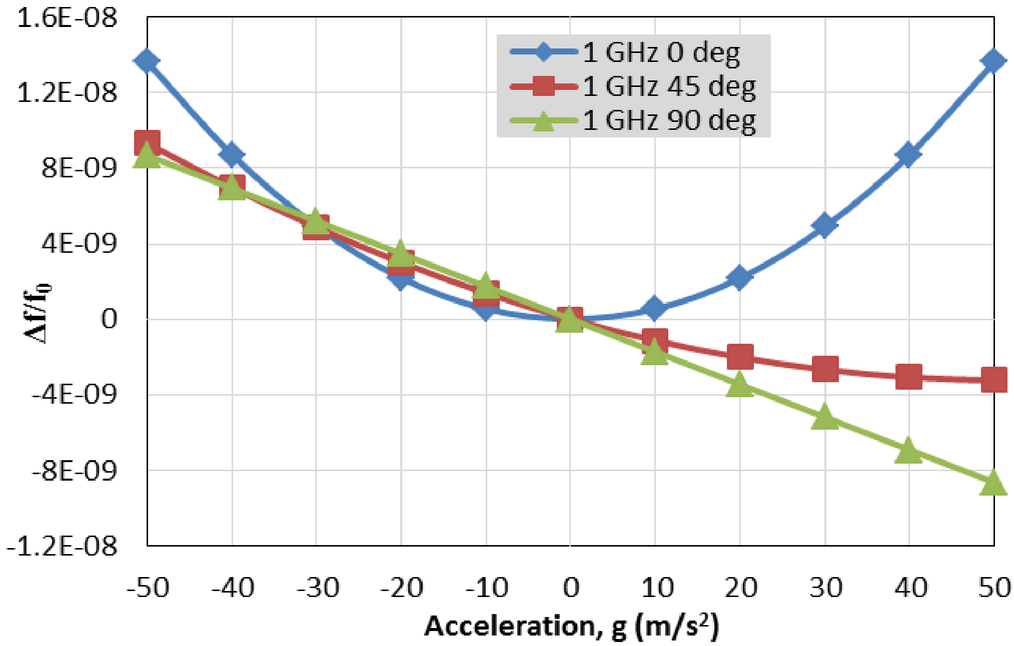

Figure 4.10: Fractional frequency change for the 1 GHz plate as a function of *g* acceleration for *AT*-cut rectangular plate at ψ_1 = 0, 45, and 90 degrees.

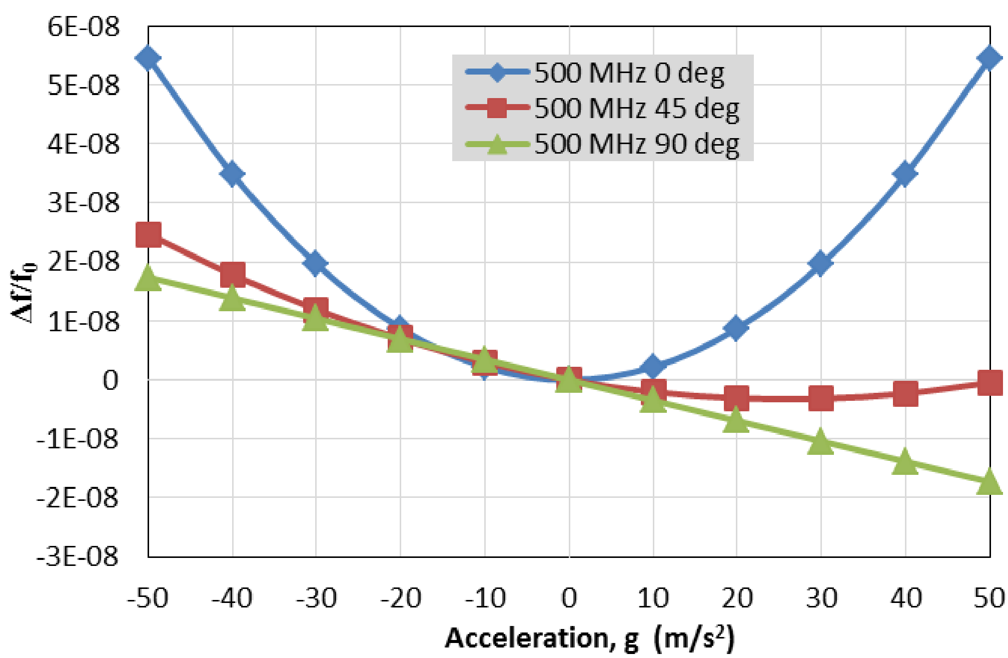

Figure 4.11: Fractional frequency change for the 500 MHz plate as a function of *g* acceleration for *AT*-cut rectangular plate at ψ_1 = 0, 45, and 90 degrees.

4.4.2 Effects of in-plane Body Force (*g* Body Force in the *X*-*Z* plane)

For the effects of *g* body force in the *X*-*Z* plane (in-plane body force), the azimuth angle ψ_2 is defined as the angle of the body force with respect to the plate *X*-axis. The fractional frequency change is computed when the quartz crystal *X*-axis (digonal axis) is parallel with the plate *X*-axis or at 90 degrees to the plate *X*-axis. The fractional change of frequency is computed for both positive and negative 1 *g* body force for the 1 GHz resonator (blue and red lines) and the 500 MHz resonator (green and purple lines) respectively in Figures 4.12 and 4.13. In Figure 4.12 where the crystal digonal *X*-axis is parallel to the plate *X*-axis ($\psi_1 = 0^o$), the body force *g* in the *X*-*Z* plane has negligible acceleration sensitivity at $\psi_2 = 90^o$ and 270^o. Again, the magnitude of fractional change of frequency for the 500 MHz resonator is twice the 1 GHz resonator. Remarkably in Figure 4.13 when the crystal digonal *X*-axis is at 90^o to the plate *X*-axis ($\psi_1 = 90^o$), the acceleration sensitivity decreased by about 1.5 orders of magnitude from Figure 4.12.

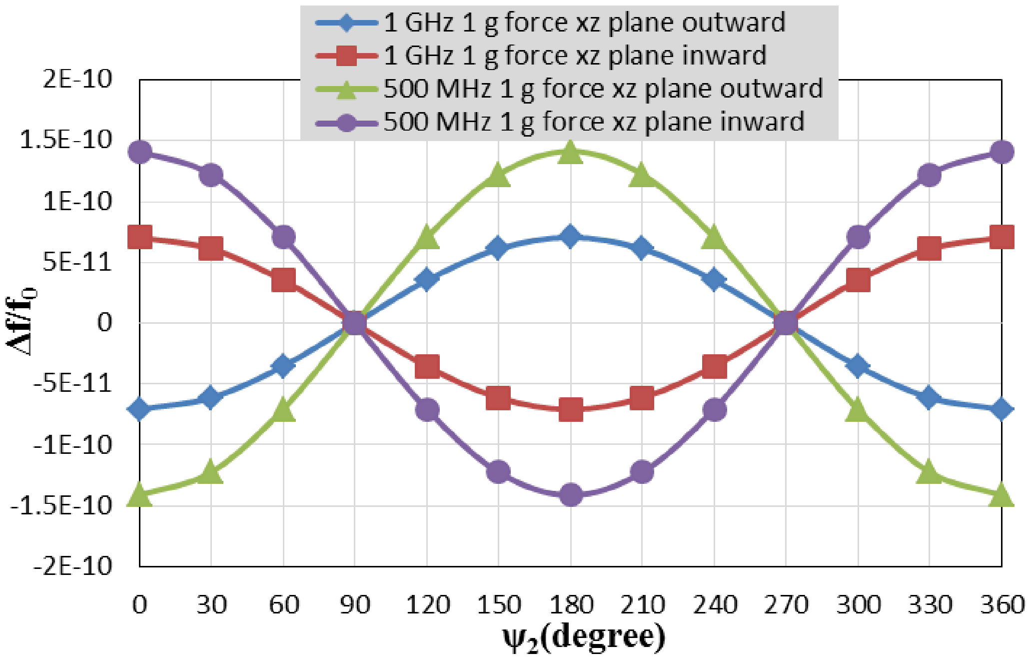

Figure 4.12: Fractional frequency change as a function of azimuth angle ψ_2 for the 1 GHz and 500 MHz *AT*-cut rectangular plates subjected to 1 *g* in-plane body force. (ψ_1 = 0°)

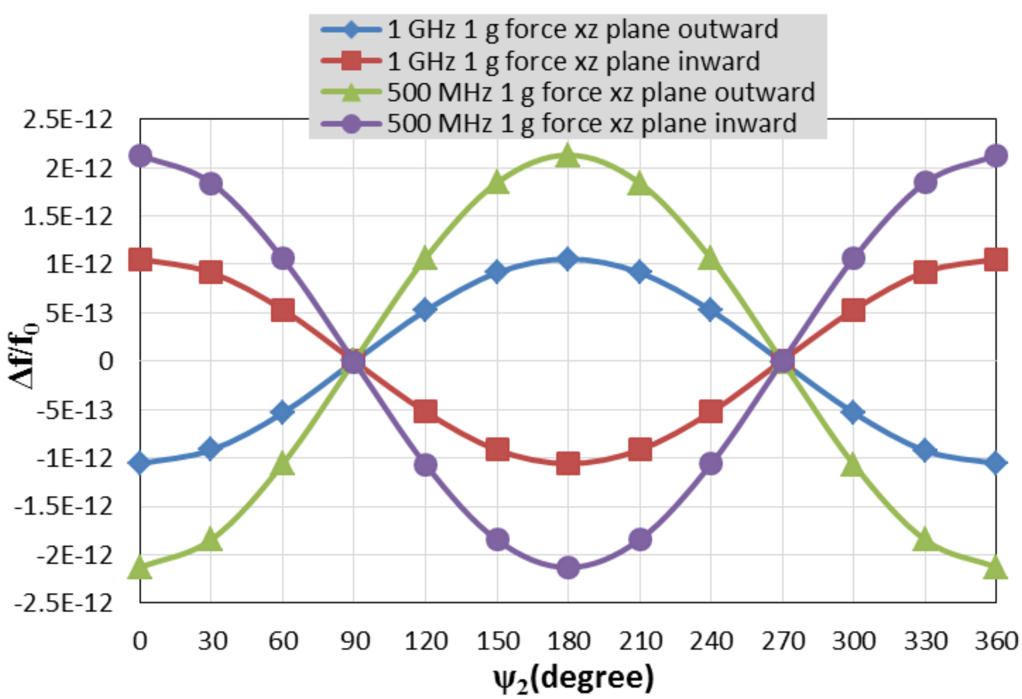

Figure 4.13: Fractional frequency change as a function of azimuth angle ψ_2 for the 1 GHz and 500 MHz *AT*-cut rectangular plates subjected to 1 *g* in-plane body force. (ψ_1 = 90°)

4.4.3 Effects of in-plane and out-of-plane Body Forces (Quartz Digonal *X*-axis is at 90^o to the Plate *X*-axis)

When the quartz resonator digonal *X*-axis is at 90^o to the plate *X*-axis, the resonator is practically insensitive to *g* body force in the *X-Z* plane while being highly sensitivity to the out-of-plane body force. This is shown in Figures 4.14 and 4.15 for the 1 GHz resonator and 500 MHz resonator respectively. We see in both figures that the in-plane acceleration sensitivity for both resonators were negligible compared to the out-of-plane acceleration sensitivity.

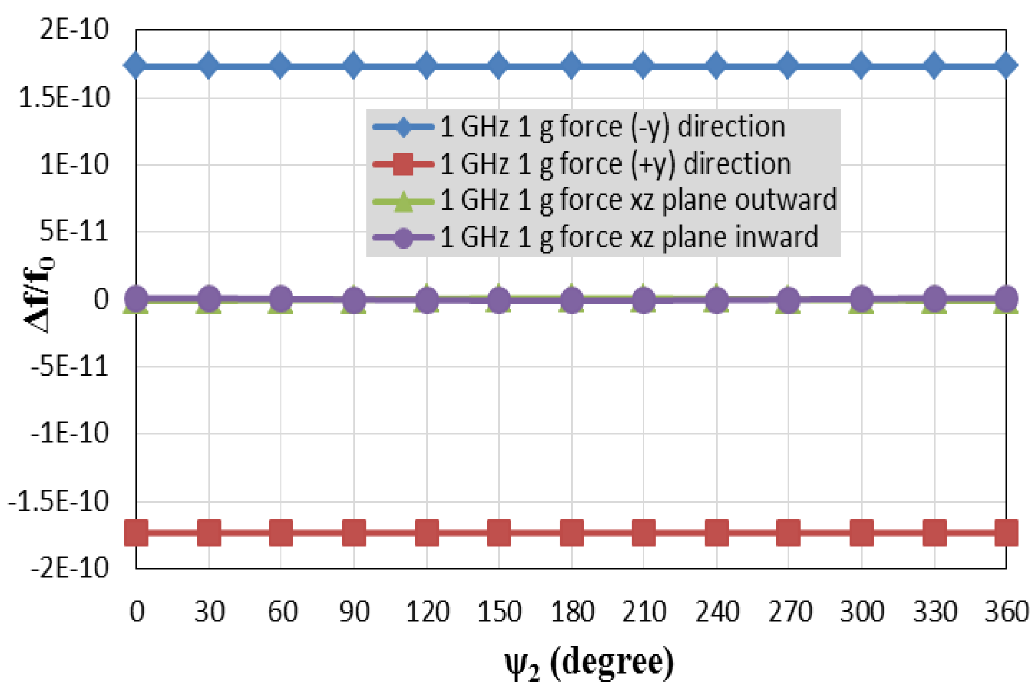

Figure 4.14: Fractional frequency change as a function of azimuth angle ψ_2 for the 1 GHz *AT*-cut rectangular plates subjected to both 1 *g* in-plane body force and 1 *g* out-of-plane body force. ($\psi_1 = 90°$)

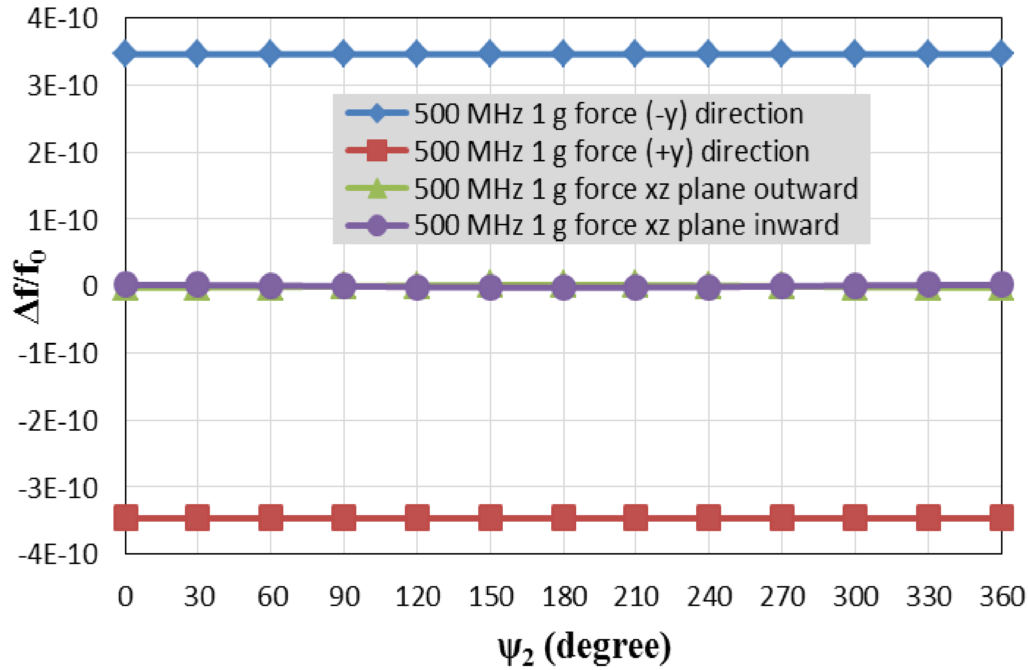

Figure 4.15: Fractional frequency change as a function of azimuth angle ψ_2 for the 500 MHz *AT*-cut rectangular plates subjected to both 1 *g* in-plane body force and 1 *g* out-of-plane body force. (ψ_1 = 90 °)

4.5 Acceleration Sensitivity Rectification in *AT*-cut Quartz Resonators

In our study of cantilever mounted resonators (1 GHz and 500 MHz) subjected to both positive and negative *g* body force in the *Y*-axis direction, we found that the acceleration sensitivity was rectified at $\psi_1 = 0^o$ and 180^o. The acceleration sensitivity is 'rectified' when the fractional change in frequency $\Delta f/f_0$ is always positive regardless of the sign of the body force.

The phenomenon of acceleration sensitivity rectification in an *AT* cut quartz resonator has never been fully discussed in previous literature on acceleration sensitivity of quartz resonators. Although the phenomenon has been observed in experiments, it has not received attention. As was noted in the previous section, the rectified acceleration sensitivity becomes the most dominant acceleration sensitivity for large g forces due to nonlinearity of the parabolic curve (blue curve in Figures 4.10 and 4.11). Therefore it is instructive that we understand this phenomenon.

The cause of rectification is the initial bending of the plate in the *X*-*Y* plane by an out-of-plane g body force in the *Y*-axis direction. The effect of rectification in a cantilever mounted plate at $\psi_1 = 0^{\circ}$ can be demonstrated with a relatively simple equation that was derived by Lee and Tang [63]. We employ the equation for thickness shear vibrations in an infinite plate subjected to homogeneous initial deformations. The fractional change of thickness shear frequency in an infinite plate subjected to initial deformations is:

$$\frac{\Delta f}{f_0} = \frac{1}{2}(\overline{D}_{11} - 1), \tag{4.22}$$

where

$$\overline{D}_{ij} = D_{ij}/C_{66} \qquad i,j = 1,2,3; \tag{4.23}$$

$$D_{ij} = \beta_{i1}\beta_{j1}C'_{66} + (\beta_{i1}\beta_{j2} + \beta_{i2}\beta_{j1})C'_{62} + \beta_{i2}\beta_{j2}C'_{22}$$
$$+(\beta_{i2}\beta_{j3} + \beta_{i3}\beta_{j2})C'_{24} + \beta_{i3}\beta_{j3}C'_{44} + (\beta_{i3}\beta_{j1} + \beta_{i1}\beta_{j3})C'_{46}. \tag{4.24}$$

Deformation gradient:

$$\beta_{ij} = \delta_{ij} + U_{i,j}, \tag{4.25}$$

Modified elastic constant:

$$C'_{pq} = C^E_{pq} + C^E_{pqr}E_r, \tag{4.26}$$

where δ_{ij} is the Kronecker delta, $U_{i,j}$ is the initial strain, C^E_{pq} the 2nd order linear elastic constant, C^E_{pqr} is the 3rd order nonlinear elastic constant and E_r is the initial strain tensor. Upon expanding $\overline{D}_{11}$ in (4.21) using (4.22) to (4.25), and neglecting small quantities of higher order terms, we obtain

$$\frac{\Delta f}{f_0} \approx \frac{1}{2}\left(2U_{1,1} + \frac{C_{66r}E_r}{C_{66}} + \frac{C_{22}}{C_{66}}U_{1,2}^2\right). \quad (4.27)$$

The first two terms on the right of (4.26) are linear initial strain while the third term is a nonlinear square of the initial bending strain $U_{1,2}$ of the plate in the *X*-*Y* plane due to the *g* body force in the direction of *Y*-axis. When the azimuth angle $\psi_1 = 0^o$, the fractional change of thickness shear frequency in (4.26) is dominated by the third term $\frac{C_{22}}{C_{66}}U_{1,2}^2$ in the expression on the right. Since the term $\frac{C_{22}}{C_{66}}U_{1,2}^2$ is always positive, the fractional change in frequency $\Delta f/f_0$ is always positive regardless of the sign of the body force, hence the acceleration sensitivity is '*rectified*', see the blue parabolic curves of Figures 4.10 and 4.11.

When the azimuth angle $\psi_1 = 90^o$, the fractional change of thickness shear frequency in (4.26) is linear and *not rectified* because the nonlinear term $\frac{C_{22}}{C_{66}}U_{1,2}^2$ on the right drops out due to lack of coupling of the thickness shear mode with the initial bending strain $U_{1,2}$ along the plate *X*-axis, see the green linear curves of Figures 4.10 and 4.11. When the azimuth angle $\psi_1 = 90^o$, Eq. (4.26) becomes linear:

$$\frac{\Delta f}{f_0} \approx \frac{1}{2}\left(2U_{3,3} + \frac{C_{44r}E_r}{C_{44}}\right) \qquad C_{44}\ at\ \psi_1 = 90° \text{ equals } C_{66}\ at\ \psi_1 = 0° \quad (4.28)$$

4.6 Experimental Results on Acceleration Sensitivity Rectification

Vibration tests were carried out using two different samples of *AT*-cut quartz plate resonators namely the S1 and the V4 resonator with the crystal digonal *X*-axis at 0 ° and 90 ° to the plate *X*-axis respectively. Since the sample resonators are limited, we only performed one test for each type of resonator to confirm the rectification of acceleration sensitivity in *AT*-cut quartz resonators. The resonators were cantilever mounted and subjected to 0.5 *g* sinusoidal vibration at 20 Hz in the *Y*-axis direction using a shaker shown in Figure 4.16. The shaking motion translates directly into phase noise for the system. The phase noise was measured using an Agilent E5052B Signal Source Analyzer. Figure 4.17 shows the phase noise for a resonator (S1, dimensions *l*=235µm, *w*=105µm, *t*=2µm) with the crystal digonal *X*-axis parallel to plate *X*-axis (ψ_1 = 0^o), while Figure 4.18 shows the phase noise for a resonator (V4, dimensions *l*=295µm, *w*=165µm, *t*=2µm) with crystal digonal *X*-axis at 90° to plate *X*-axis (ψ_1 = 90^o). In both cases the aluminum electrodes are of thickness 0.08µm. Although the resonators are not of identical design, measured data supports the developed theory.

Observe from Figure 4.17, the S1 resonator shows peaks in phase noise at offset frequency of 20 Hz and 40 Hz, and also at 60 Hz which represents power line feed through. The peak at 20 Hz is associated with the shaker excitation frequency. The presence of the peak at 40 Hz verifies that acceleration sensitivity of the S1 resonator is *rectified* when the crystal digonal *X*-axis is parallel to the plate *X*-axis (ψ_1 = 0^o). Figure 4.18, the larger V4 resonator again shows a peak in phase noise at offset frequency of 20 Hz due to the shaker excitation, however, there is no peak in phase noise at 40 Hz. This verifies that the acceleration sensitivity in the V4 resonator is *not rectified* when the crystal digonal *X*-axis was at 90° to the plate *X*-axis (ψ_1 = 90^o).

The above phase noise measurements validate our model results for acceleration sensitivity that is either rectified or not rectified depending on the angle of the crystal digonal *X*-axis with respect to the plate *X*-axis.

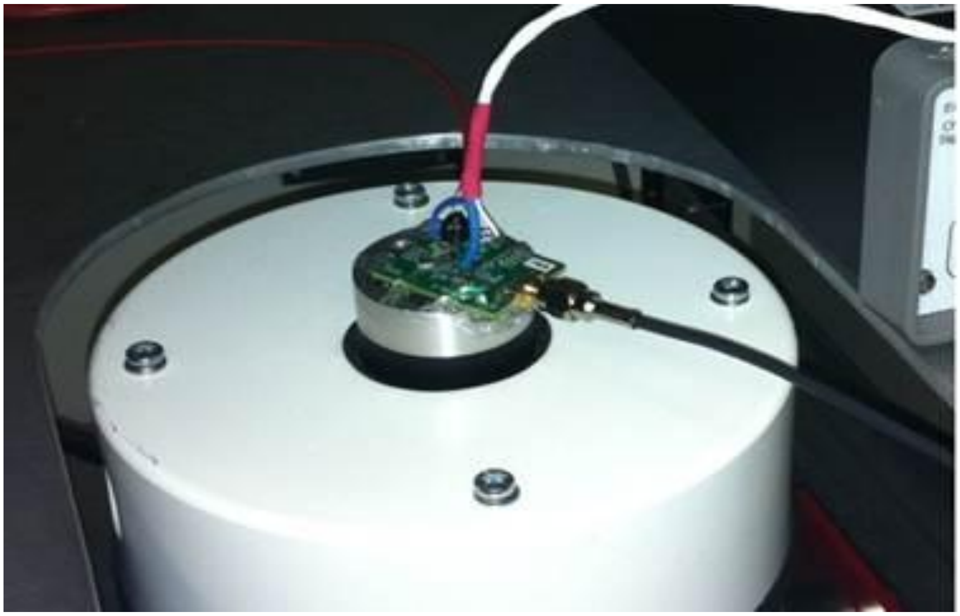

Figure 4.16: Resonator mounted on a shaker.

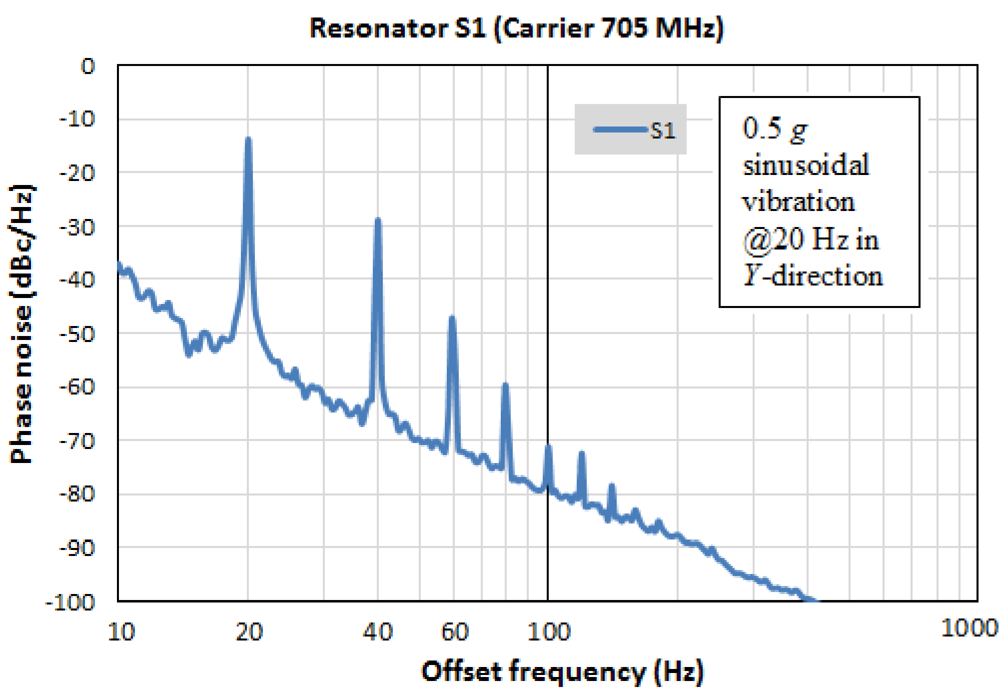

Figure 4.17: Phase noise of the S1 resonator ($\psi_1 = 0°$) with carrier frequency of 705 MHz.

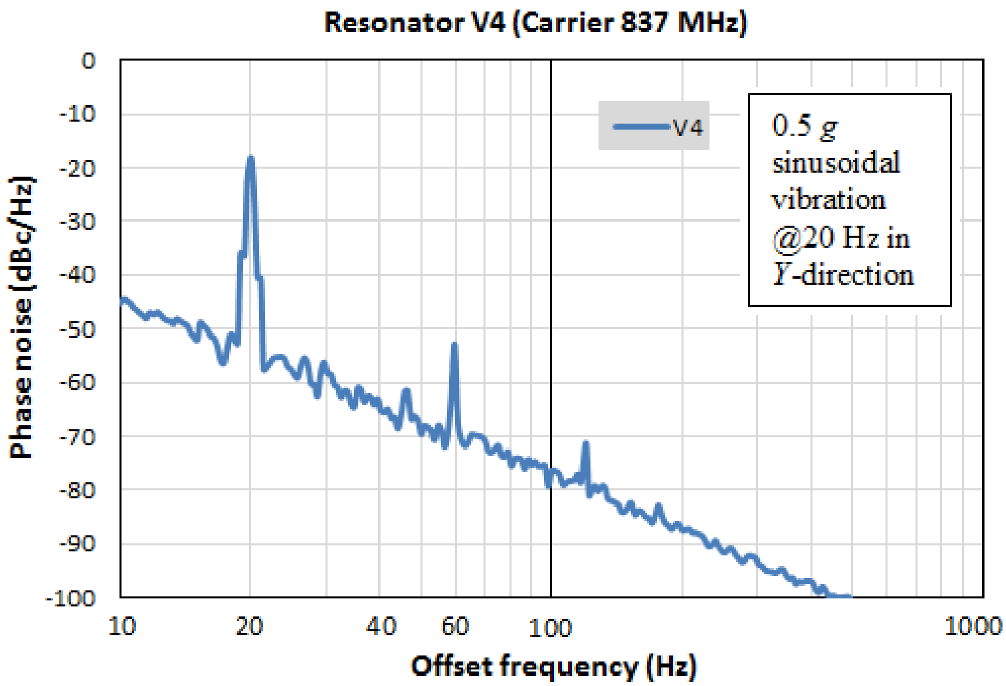

Figure 4.18: Phase noise of the V4 resonator ($\psi_1 = 90°$) with carrier frequency of 837 MHz.

4.7 Active Reduction of Acceleration Sensitivity by Two Pairs of Edge Electrodes

Our analyses of the 1 GHz and 500 MHz *AT*-cut plates have shown that when $\psi_1 = 90°$, the acceleration sensitivity is predominantly due to out-of-plane body forces in the *Y*-axis direction. We show in this section active reduction of the acceleration sensitivity for out-of-plane vibration. Active reduction of acceleration sensitivity due to in-plane forces is not needed because the in-plane body forces have minimal effects when $\psi_1 = 90°$.

A cantilever rectangular plate bends under a body force in the *Y*-axis direction. Figure 4.19 shows the deformed shape of the 1 GHz plate subjected to -1 *g* body force in the *Y*-axis direction. The bending deformation causes initial strains in the energy trapped area under the main electrodes that in turn causes fractional frequency change in the plate resonator.

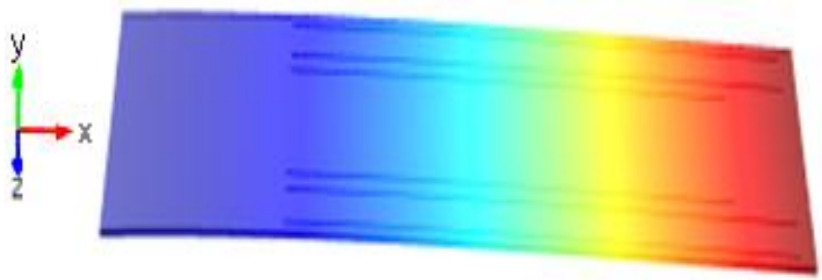

Figure 4.19: Total displacement of 1 GHz plate subjected to -1 *g* body force in *Y*-axis direction. (ψ_1 = 90°)

We can reduce the initial strains in the energy trapped area of the plate resonator by applying a potential to two pairs of edge electrodes shown in Figure 4.7. The edge electrodes on the plate bottom surface are grounded while the two top edge electrodes are subjected to opposite polarity electric potential, that is, when one top edge electrode is applied with a positive electric potential, the other top edge electrode on the opposite edge is applied with a negative potential. Figure 4.20 shows the upward bending resulting from the applied potentials.

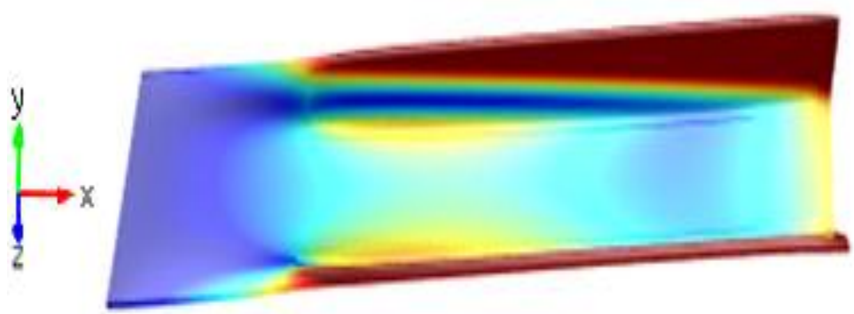

Figure 4.20: Total displacement of 1 GHz plate subjected to DC bias field in the edge electrodes. (ψ_1 = 90°)

Since deformation of the resonator caused by edge electrodes can bend the plate in the opposite direction to that caused by an out-of-plane body force, we can therefore use the edge electrodes to actively reduce the fractional change in frequency of the plate resonator. Figures 4.10 and 4.11 shown the linear relationship (green line) between the fractional frequency change and the body force in the *Y*-axis direction for the 1 GHz and 500 MHz plate resonator respectively. Figures 4.21 and 4.22 show the same linear relationship exists between the fractional frequency change and the electric potential of the edge electrodes for the 1 GHz and 500 MHz plate resonator respectively. The effect of a DC bias voltage applied to the edge electrodes on $\Delta f/f_0$ is presented for 1 GHz (Figure 4.21) and 500 MHz (Figure 4.22) plates respectively.

For the 1 GHz resonator, +/- 0.5 V changes $\Delta f/f_0$ by about +/- 15 ppb, while for the 500 MHz resonator, +/- 1.4 V changes $\Delta f/f_0$ by about +/- 20 ppb. Since the slope of the line in Figures 4.21 and 4.22 is positive while the slope of the green line in Figures 4.10 and 4.11 is negative, we could in principle actively reduce the acceleration sensitivity of the ψ_1 = 90 °, cantilever mounted *AT*-cut plate resonator.

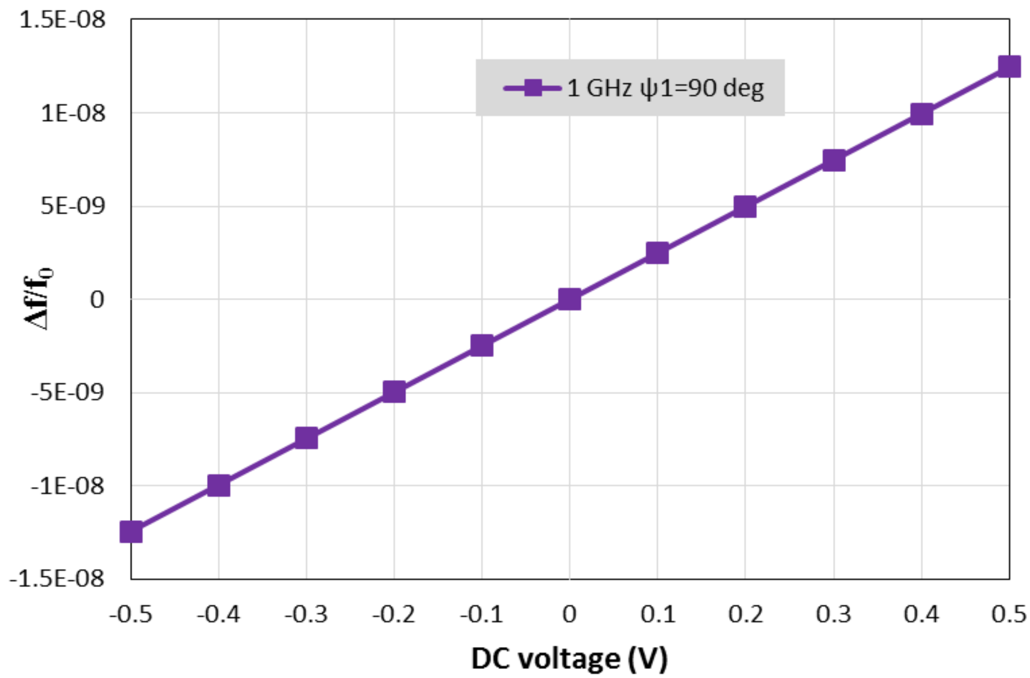

Figure 4.21: Effect of DC bias at edge electrodes on fractional frequency change of the 1 GHz *AT*-cut plate resonator. (ψ_1 = 90°)

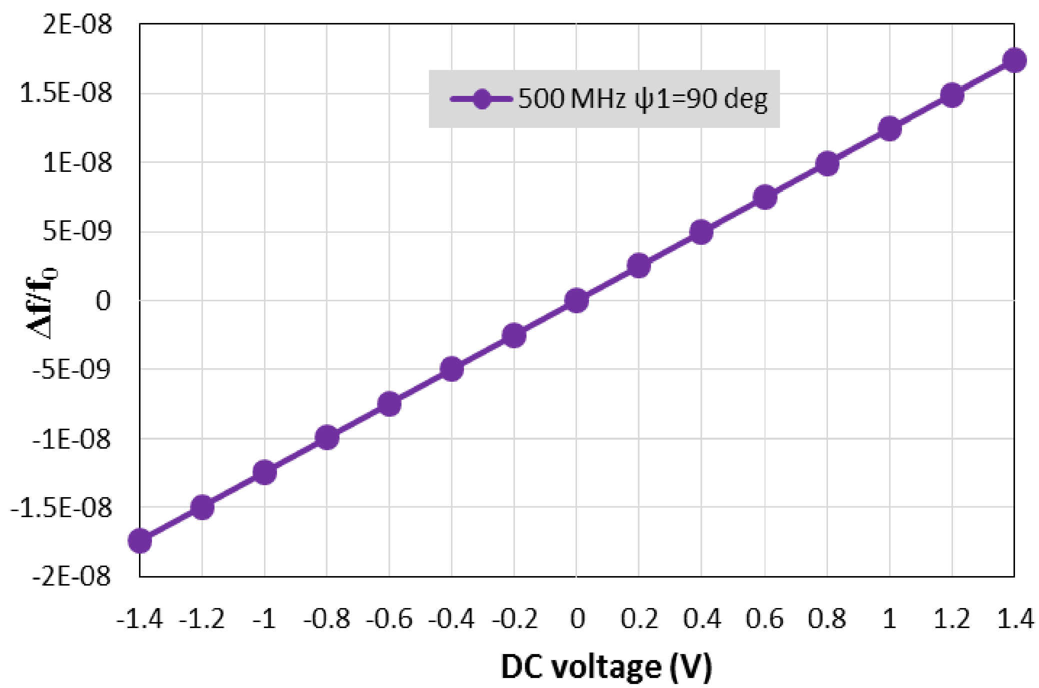

Figure 4.22: Effect of DC bias at edge electrodes on fractional frequency change of the 500 MHz *AT*-cut plate resonator. (ψ_1 = 90°)

4.8 Conclusions

Incremental piezoelectric equations for small vibrations superposed on initial deformations were presented. The equations were implemented in COMSOL finite element models. The model was validated by comparing simulated results for the force sensitivity coefficient K_f of a circular quartz plate subjected to a pair of diametrical forces, with measured data. The model results were found to be very accurate.

The effects of in-plane and out-of-plane body forces on the cantilever mounted, 1 GHz and 500 MHz *AT*-cut plate resonators as a function of the ψ_1 angle were studied. The ψ_1 angle was defined as the angle between crystal digonal *X*-axis and resonator plate *X*-axis. A summary of our findings are as follow:

1) The acceleration sensitivity due to in-plane body force is about 50 times smaller when $\psi_1 = 90°$ than when $\psi_1 = 0°$.

2) The acceleration sensitivity due to out-of-plane body force is independent of the sign of the body force when $\psi_1 = 0°$, that is, the acceleration sensitivity is 'rectified'. The rectification is due to the square of the initial bending strains in the *X*-*Y* plane.

3) The rectified acceleration sensitivity as a function of the magnitude of out-of-plane body force follows a nonlinear parabolic curve so that the sensitivity is small when body force is small but then grows nonlinearly for larger body forces.

4) Phase noise measurement of two resonators with $\psi_1 = 0°$ and $\psi_1 = 90°$ respectively showed the acceleration sensitivity was rectified for $\psi_1 = 0°$ and not rectified for $\psi_1 = 90°$. The measurements were consistent with the model results.

5) Active reduction of acceleration sensitivity could be employed for the plate resonator with $\psi_1 = 90°$ because

   a) the effects of in-plane body forces are negligible compared to the effects of the out-of-plane body forces,

   b) the fractional frequency change due to out-of-plane body force varies linearly with the magnitude of body force, and

   c) the fractional frequency change due to DC bias at two pairs of edge electrodes varies linearly with the magnitude of electric potential.

6) The FEA acceleration sensitivity due to +-1 *g* of body force in the *Y*-axis direction for the 1 GHz and 500 MHz resonator

   a) at $\psi_1 = 0°$, are 5.44e-12/*g* and 2.18e-11/*g* respectively, and

   b) at $\psi_1 = 90°$, are -+1.73e-10/*g* and -+3.47e-10/*g* respectively.

The body force in the *Y*-axis direction could be detected and measured using an accelerometer. The deflection of the cantilever plate resonator could also be measured by a change in capacitance by methods used in MEMS devices. The measured values of *Y*-axis acceleration or deflection could be calibrated with respect to the DC-bias voltage of the edge electrodes. In turn the fractional change in frequency of the resonator could be actively reduced by applying a DC-bias voltage at the edge electrodes.

Chapter 5 Effects of External Forces on the Fundamental and Third Overtone Frequency of Quartz Crystal Plates

5.1 Introduction

Frequency shift in quartz crystal resonators due to applied external forces or vibration have been studied extensively by various researchers such as Ballato, Mingins and Fletcher et al. [37, 26, 27, 38] to investigate methods leading to the design of quartz resonators that are stable with respect to mechanically induced vibration and acceleration. The study of vibrating crystal plate under the action the external forces is important. It provides means of understanding in the frequency deviations experience by vibration and acceleration. In the previous chapter, the acceleration sensitivity of 1 GHz resonator and 500 MHz resonator were studied using incremental piezoelectric equations for small vibration superposed on initial deformations. The initial strains in these acceleration sensitivity problems were computed using linear three-dimensional equations of elasticity.

In this chapter, effects of external forces on the fundamental and third overtone frequency of crystal plates are studied. Circular plates of quartz crystals are respectively subjected to compressional stress applied diametrically to the edges of plate and flexural bending in different configurations as function of azimuth angle ψ. Three types of bending arrangement have been used (a) a clamped cantilever, (b) a cantilever with displaced knife edges, and (c) a dual support symmetric bending. FEA results matched extremely well with experimental data for both the in-plane compressional stress on the edge of quartz plate and flexural bending of crystal plate in different configurations in fundamental thickness shear mode and the third overtone mode. We have found that the initial strains computed using linear equations of elasticity are accurate only for acceleration sensitivity in the case of in-plane forces or vibrations. For acceleration sensitivity in the case of out-of-plane forces or vibrations the linear equations of elasticity are not accurate. We have found that for accurate predictions of frequency deviation due to external forces, the nonlinear terms in the initial stresses/strains must be retained in order to fully capture the out-of-plane deformations in resonators.

5.2 Geometric Nonlinearity

Nonlinearity occurs in many practical applications of engineering. The underlying principle of nonlinear behavior is that cause and effect relationships are not proportional unlike the linear system. Nonlinear behavior can be grouped into two general behaviors: material nonlinearity and geometric nonlinearity. Material nonlinearity arises when the material exhibits nonlinear stress-strain relationship. Geometric nonlinearity arises when a system undergoes large deformation in which there are finite changes in the geometry of deforming body.

Normally it is small strains which define whether a problem is geometrically linear. However, there are geometric nonlinear problems that are small strains but with finite rotations and bending deflections. Geometric nonlinearity should be used whenever there is finite bending, where the linear strain tensor is replaced by the Green-Lagrange strain tensor, and the Cauchy stress tensor is replaced by the second Piola-Kirchhoff stress tensor. The strain-displacement equations for the linear strain tensor and Green-Lagrange strain tensor are:

Linear strain tensor:

$$S_{ij} = \tfrac{1}{2}(U_{i,j} + U_{j,i}), \qquad (5.1)$$

Green-Lagrange strain tensor:

$$S_{ij} = \frac{1}{2}(U_{i,j} + U_{j,i} + U_{k,i}U_{k,j}). \tag{5.2}$$

In the previous chapter, linear initial strains were used for the acceleration sensitivity of 1 GHz and 500 MHz resonators. We have found that the initial strains computed using linear equations of elasticity are accurate only for acceleration sensitivity in the case of in-plane forces or vibrations shown in Figure 5.1. In Figure 5.1, the solid blue line (linear model) and the dashed purple line (nonlinear model) match the measured data very well. For acceleration sensitivity in the case of out-of-plane forces or vibrations, the linear equations of elasticity are not accurate and they are shown in Figures 5.2. The linear model (blue line) overestimates the fractional frequency change as compared to the nonlinear mode (purple line) for large out-of-plane accelerations. However, our analyses of 1 GHz resonator and 500 MHz resonator due to 1 *g* of body force using the linear strains are adequate because for low accelerations of less than 5 *g*, the nonlinear model yields the same results as the linear model shown in Figure 5.3.

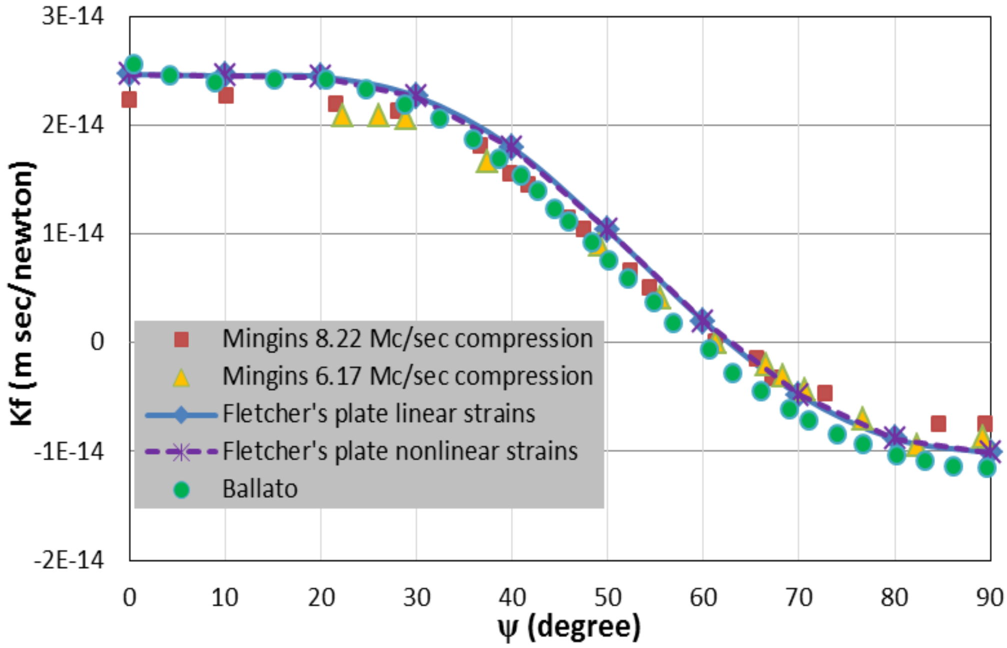

Figure 5.1: Force sensitivity coefficient K_f as a function of the azimuth angle ψ for the *AT*-cut crystals with measured data by Ballato [37] and Mingins [26].

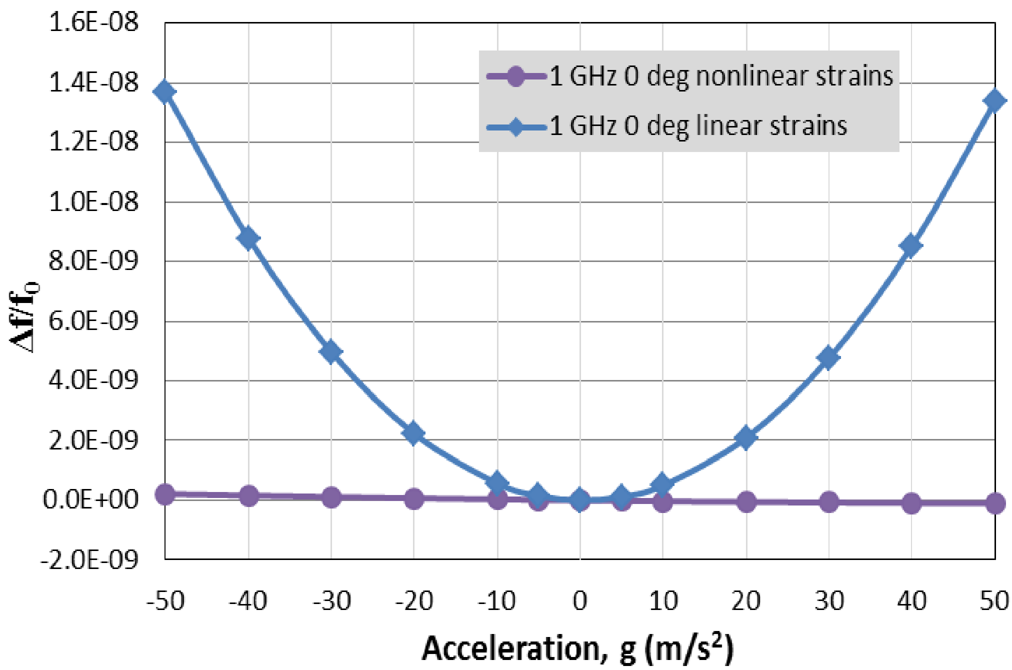

Figure 5.2: Fractional frequency change for the 1 GHz plate as a function of g acceleration for *AT*-cut rectangular plate at $\psi_1 = 0$.

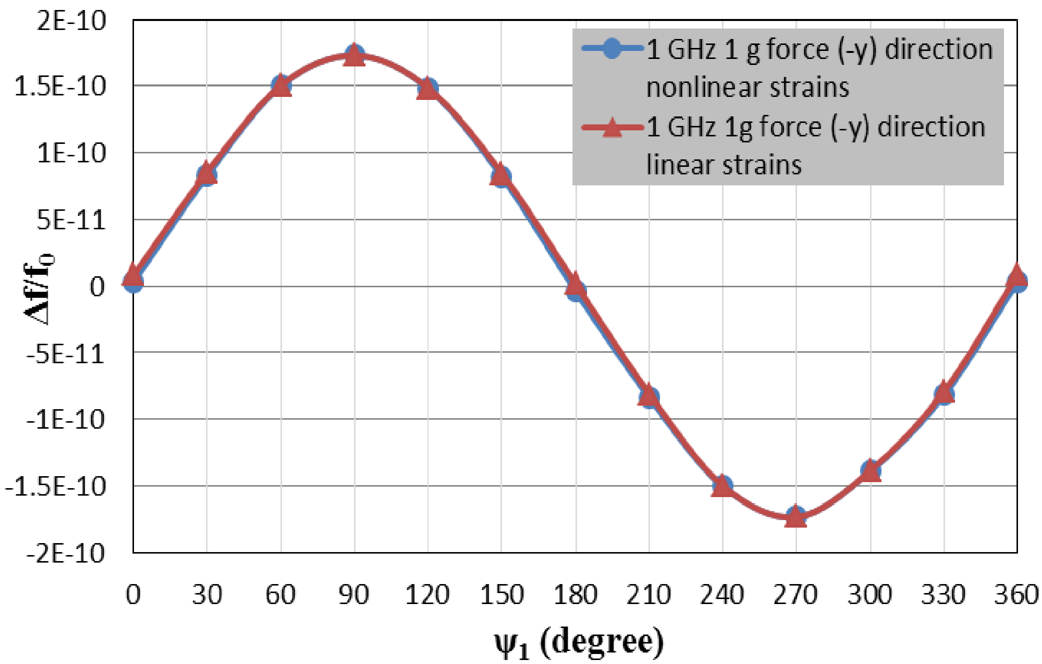

Figure 5.3: Frequency change as a function of azimuth angle ψ_1 for the 1 GHz *AT*-cut rectangular plates for 1 *g* out-of-plane body force.

5.3 Equations of Incremental Motion Superposed on Finite Deformations

For our study of acceleration sensitivity of quartz resonators we employ the Lagrangian three-dimensional equations of motion for incremental vibrations superposed on finite deformations [64]. The Lagrangian formulation is employed as the governing equations for fields at the initial state and the final state. By taking the difference between the final state and the initial state shown in Table 5.1, incremental field equations due to small amplitude of vibrations are obtained. For simplicity here we write only the mechanical equations of incremental motion superposed on finite deformations since the electro-mechanical coupling of quartz is small. Our COMSOL models and results have included the piezoelectric effects. These equations are employed to study the effects of external forces on the circular crystal resonator in the next section.

	Final (present state)	*Initial (initial state)*	*Incremental (difference)*
Displacement	$\bar{U}_i = z_i - x_i$	$U_i = y_i - x_i$	$u_i = \bar{U}_i - U_i$
Strain	$\bar{S}_{ij}$	S_{ij}	$s_{ij} = \bar{S}_{ij} - S_{ij}$
2nd PK. stress	$\bar{T}_{ij}$	T_{ij}	$t_{ij} = \bar{T}_{ij} - T_{ij}$
Body force	$\bar{B}_i$	B_i	$b_i = \bar{B}_i - B_i$

Table 5.1: Incremental field equations.

Incremental displacements:

$$u_i = \bar{U}_i - U_i, \tag{5.3}$$

Incremental strains:

$$s_{ij} = \tfrac{1}{2}(u_{i,j} + u_{j,i} + U_{k,i}u_{k,j} + U_{k,j}u_{k,i}), \tag{5.4}$$

Incremental stresses:

$$t_{ij} = \left(C^E_{ijkl} + C^E_{ijklmn}S_{mn}\right)s_{kl}, \tag{5.5}$$

Incremental stress equations of motion:

$$(t_{ij} + t_{jk}U_{i,k})_{,j} + \rho b_i = \rho \ddot{u}_i \quad in \ \ V, \tag{5.6}$$

$$p_i = n_j\left(t_{ij} + t_{jk}U_{i,k}\right) \ \ on \ \ S. \tag{5.7}$$

5.4 Effects of External Forces on the Fundamental Frequency

In this section the effect of external forces on the fundamental thickness shear mode is studied. Circular plates of quartz crystals are respectively subjected to compressional stress applied diametrically to the edges of plate and flexural bending in different configurations as function of azimuth angle ψ.

5.4.1 Circular Disk Subjected to Diametrical Forces (Fundamental Mode)

The effect of compressional stress applied diametrically to the edge of a circular quartz crystal was demonstrated by comparing 3-D finite element method results with those experiment results by Mingins [26]. An *AT*-cut quartz crystal of diameter *d* and thickness *2b*, subjected to a pair of diametrical forces *F* at an angle ψ (azimuth angle) with the X_1-axis as shown in Figure 5.4. The frequency change was measured as a function of the ψ angle. The crystal plate dimensions were diameter *d=0.5* inch, with gold electrode buttons of 0.25 inch in the center with thickness giving a relative frequency change due to mass loading of 0.5% and azimuth angle ψ varying from 0 °to 180. The results are shown in Figures 5.5 and 5.6.

Figures 5.5 and 5.6 showed the effects of compressive force (500 grams) on the fundamental thickness shear mode of an *AT*-cut plate as a function of the azimuth angle ψ at frequency of 6.17 Mc/s and 8.22 Mc/s respectively. In Figure 5.5, the solid red and the solid green curves are our FEA mode results using the linear initial strains and the nonlinear initial strains respectively. Both results showed good agreement with the measured results of Mingins et al. [26]. We concluded that the linear initial strains were sufficient for accurate prediction of plate resonator under compressional stresses and deformations. We observed that at ψ=65° and 115°, the applied compressional force produces no frequency change at these two angles and the maximum negative frequency shift occurs at ψ=90°. It was quite obvious that the frequency change curve is symmetric at ψ=90°, meaning that the axis of symmetry is about X_3-axis. In Figure 5.6, frequency change as function of ψ for the 8.22 Mc/s plate exhibits same behavior as in Figure 5.5.

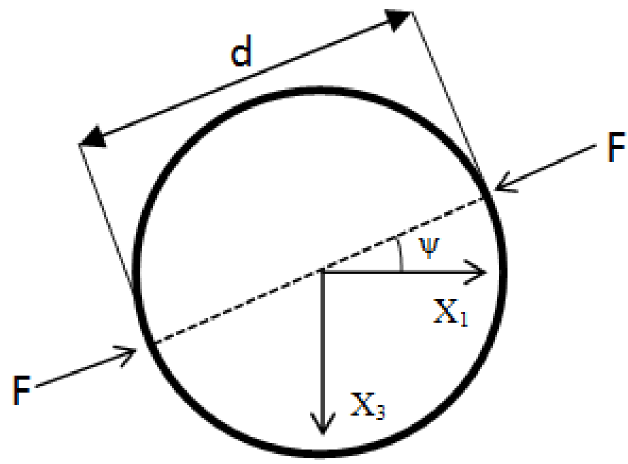

Figure 5.4: Circular disk subjected to diametrical forces [37].

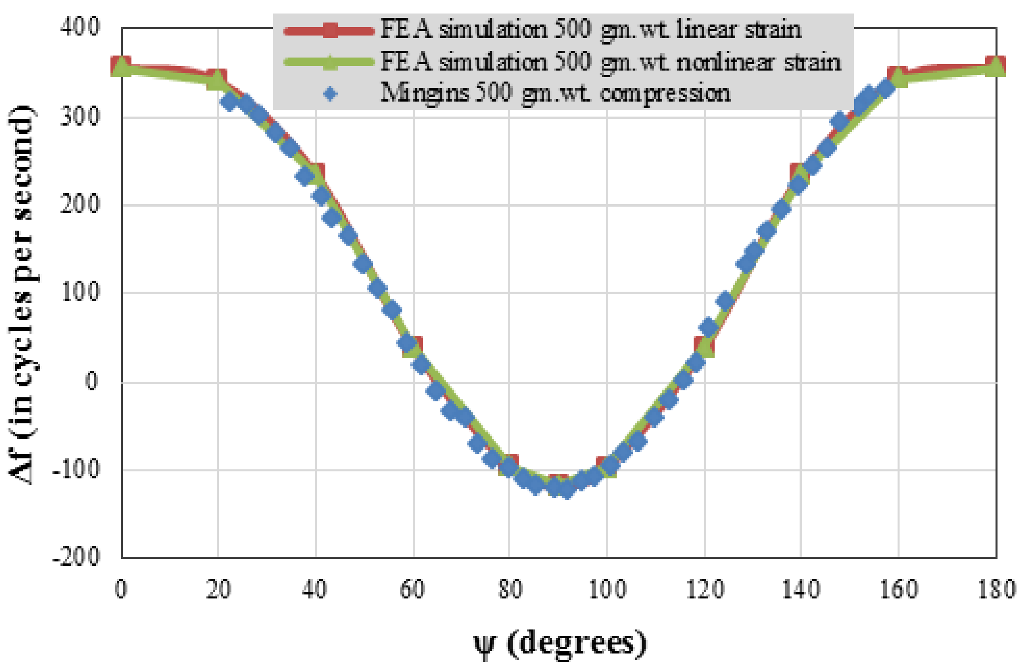

Figure 5.5: Frequency change as function of ψ for compression stress at fundamental frequency of 6.17 Mc/s for *AT*-cut circular plate.

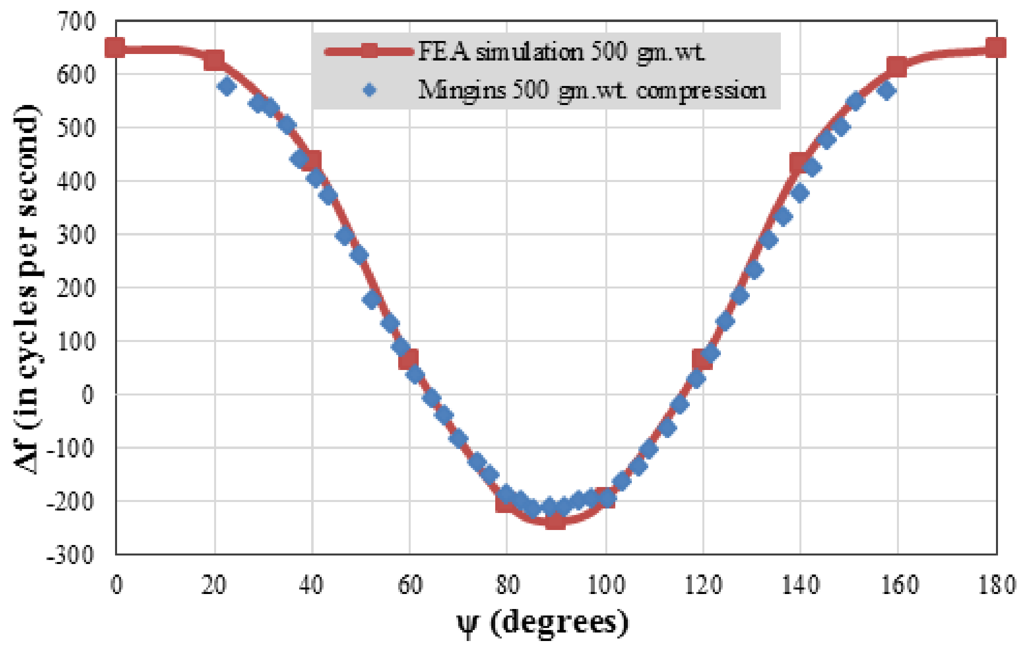

Figure 5.6: Frequency change as function of ψ for compression stress at fundamental frequency of 8.22 Mc/s for *AT*-cut circular plate.

5.4.2 Two Grams Force Cantilever Bending

The effects of bending moment on the fundamental frequency of the 10 MHz *AT*-cut and *SC*-cute circular plate resonators were studied. The crystal plate dimensions were *d*=12mm, silver electrodes of 4mm in the center with thickness giving a relative frequency change due to mass loading of 0.5%. The bending was applied on either the cantilever mounted plate or the symmetrically mounted plate. The experimental apparatus for applying bending forces and cantilever bending are shown in Figures 5.7 and 5.8.

In order to study the effects of bending force on the *AT*-cut plate mounted in the cantilever configuration, the crystal was clamp at one end, and 2 grams force was applied at the diametrically opposite end to create an upward bending of the crystal shown in Figure 5.9. The angle ψ was the angle between the *X*-axis of the clamped edge to the crystal *X′*-axis. The model results of frequency change due initial strains from either the linear strain equation (5.1) or the nonlinear strain equation (5.2) were compared to the Fletcher and Douglas [38] experimental results in Figure 5.10. The solid green curve is the frequency change due to linear initial strains while the solid red curve is the frequency change due to nonlinear initial strains. We observed that the solid red curve compared well with the experimental data while solid green curve did not compare well. Therefore, for out-of-plane bending the nonlinear initial strains must be used for accurate modeling. The frequency change due to linear initial strains was accurate only at two angles $\psi = 90°$ and $270°$.

The linearity of frequency change with the applied cantilever force is of fundamental interest because it determines whether the principle of superposition is applicable. Figure 5.11 shows the frequency change as a function of the applied cantilever force from 0 to 10 grams-force. Measured results from Fletcher and Douglas [38] showed that the frequency change with applied cantilever force was linear when the azimuth angle ψ was 270° and nonlinear when ψ was 220°. Our COMSOL model results using nonlinear initial strains matched well the experimental results for the azimuth angle $\psi = 270°$. For the azimuth angle $\psi = 220°$ the model results was good only for applied cantilever force up to 2 grams-force.

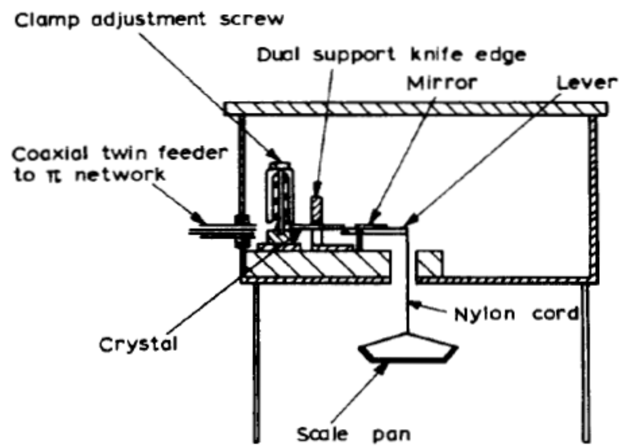

Figure 5.7: Apparatus for applying bending forces to a crystal Fletcher and Douglas [38].

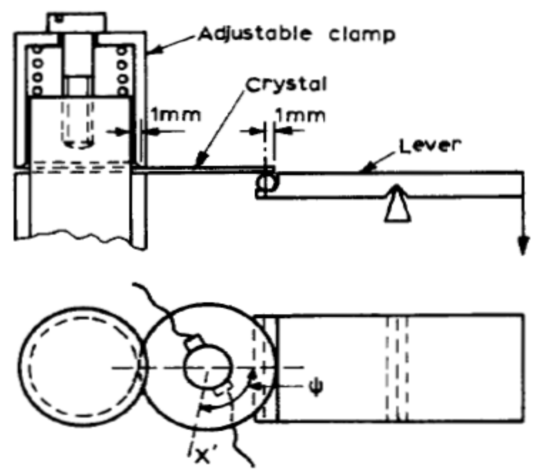

Figure 5.8: Cantilever bending by Fletcher and Douglas [38].

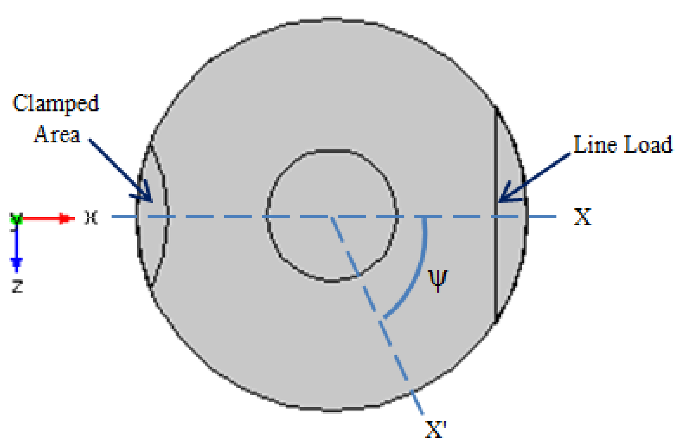

Figure 5.9: Cantilever bending of *AT*-cut circular plate.

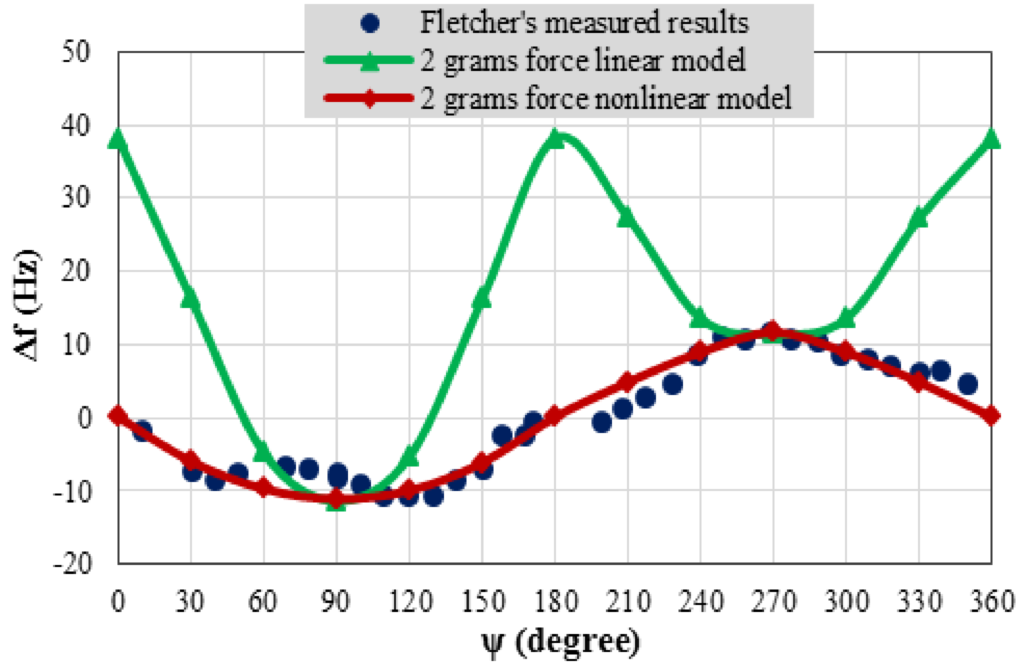

Figure 5.10: Frequency change as a function of azimuth angle ψ for the cantilever bending of *AT*-cut circular plate resonator.

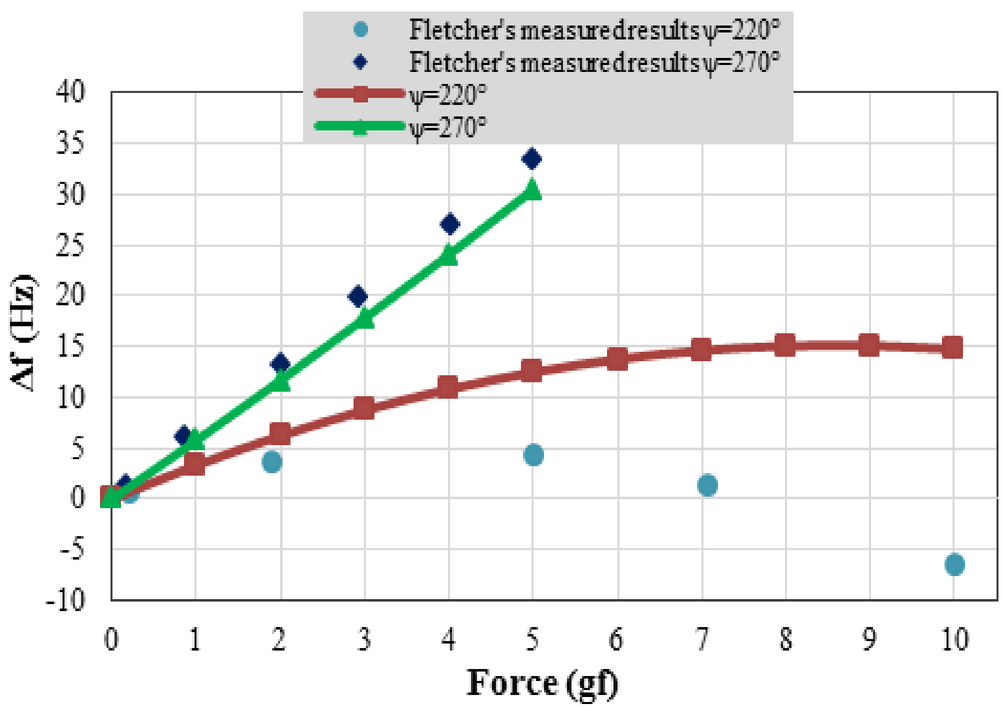

Figure 5.11: Frequency change as a function of applied cantilever force on the *AT*-cut circular plate resonator for two azimuth angles ψ = 220° and 270°.

The 10 MHz *SC*-cut plate was also studied in cantilever configuration, and good comparisons with the measured results could only be obtained when the nonlinear initial strains were used. The results of both the linear and the nonlinear initial strains models were compared with Fletcher and Douglas [38] measured data shown in Figure 5.12. We have found that our nonlinear model results (solid red curve) matched well with the measured data when our model's azimuth angle ψ was shifted +90°. Since the plate was circular, Fletcher and Douglas might have erred in starting their measured data at ψ = 90° instead of 0°. The frequency change using linear initial strains (solid green curve) was accurate only at ψ angles 0° and 180°, respectively.

The linearity of frequency change with applied cantilever force with respect to the *SC*-cut crystals was also studied. The results shown in Figure 5.13 for azimuth angle ψ = 40° are linear and the principle of superposition is therefore applicable. Our model results (solid red line) using nonlinear initial strains were also linear although the slope of the line was less than the measured results of Fletcher & Douglas.

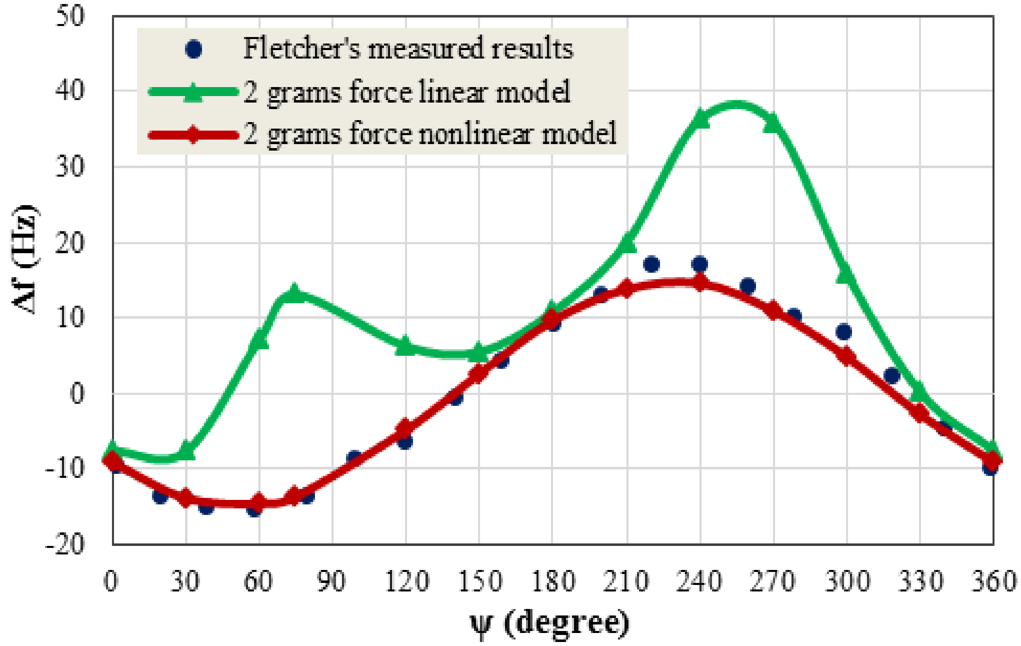

Figure 5.12: Frequency change as a function of azimuth angle ψ for cantilever bending of *SC*-cut crystal.

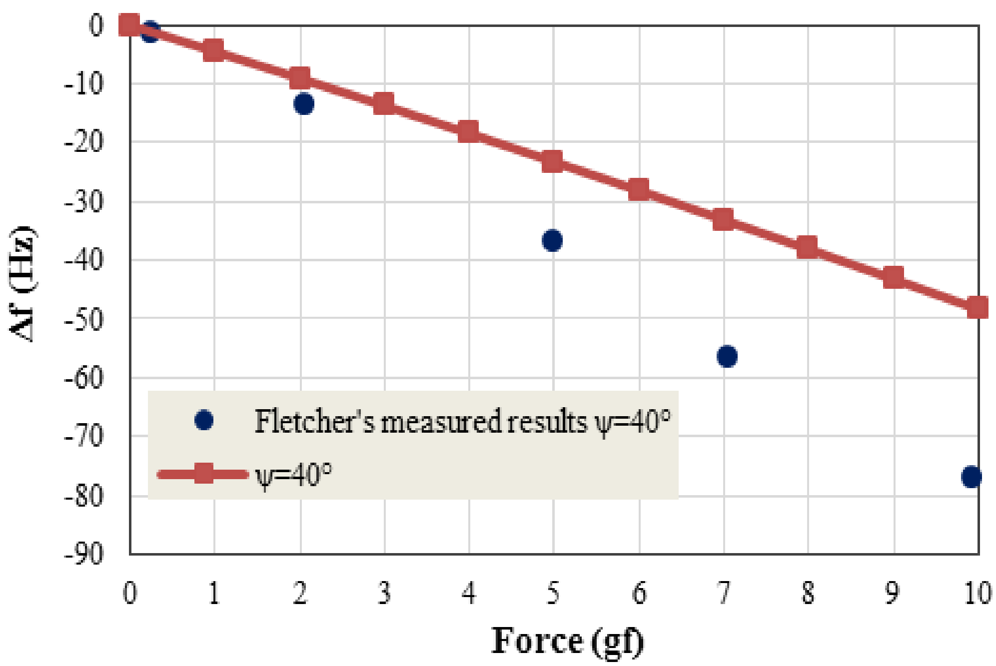

Figure 5.13: Frequency change as a function of applied cantilever force on the *SC*-cut circular plate resonator for azimuth angle ψ = 40°.

5.4.3 Five Grams Force Symmetrical Bending

Fletcher and Douglas also measured the effects of bending force in a symmetrical configuration shown in Figure.5.14. The crystal was clamped at one end, a knife edge placed over the top at the midway point to the opposite edge, and a line load of 5 grams force was applied at the opposite edge. Figure 5.15 shows our model of the symmetric bending configuration. Figure 5.16 shows our model results using nonlinear initial strains in comparison with the measured data by Fletcher and Douglas [38]. Our model results (red curve) showed a trend similar to the measured data (blue curve) although the magnitude of frequency changes were off at some azimuth angles ψ such as 105°, 150°, and 225°.

The linearity of frequency change with applied bending force for symmetrical bending at ψ = 90° was also studied. Figure 5.17 shows the measured data in comparison with our model results using nonlinear initial strains. Both measured data and model results have similar trends with slightly nonlinear curves although the slope of our model results (red line) was less than that of the measured.

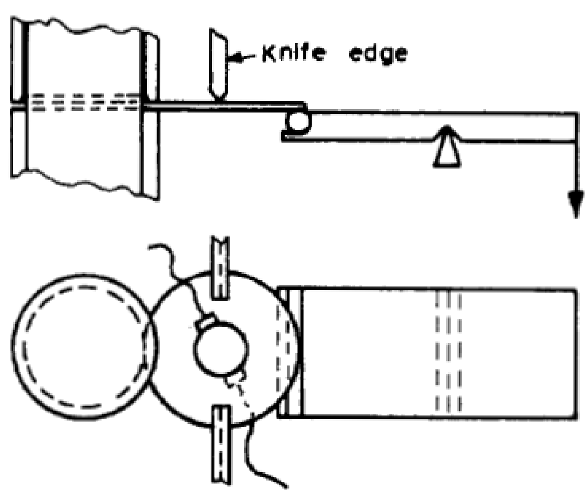

Figure 5.14: Symmetrical bending by Fletcher and Douglas [38].

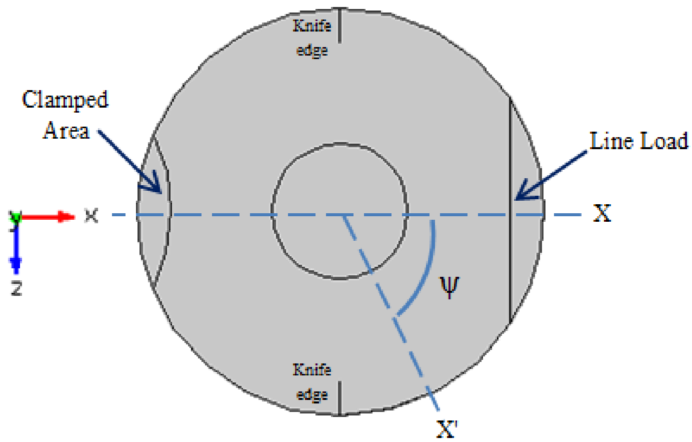

Figure 5.15: Symmetrical bending of *SC*-cut circular plate.

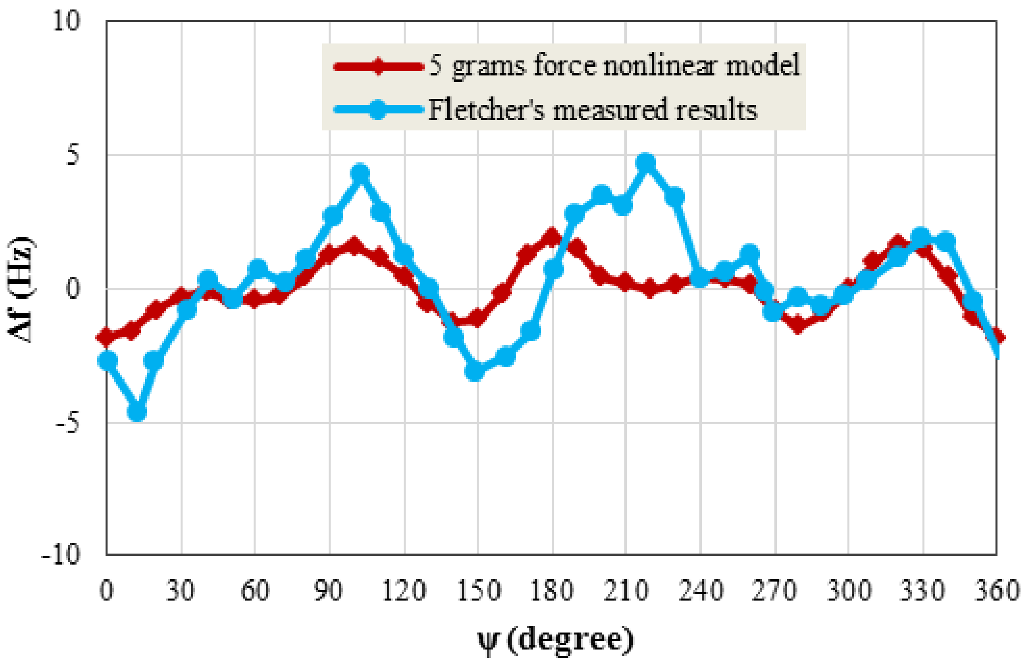

Figure 5.16: Frequency change as a function of azimuth angle ψ for symmetrical bending of *SC*-cut circular plate resonator.

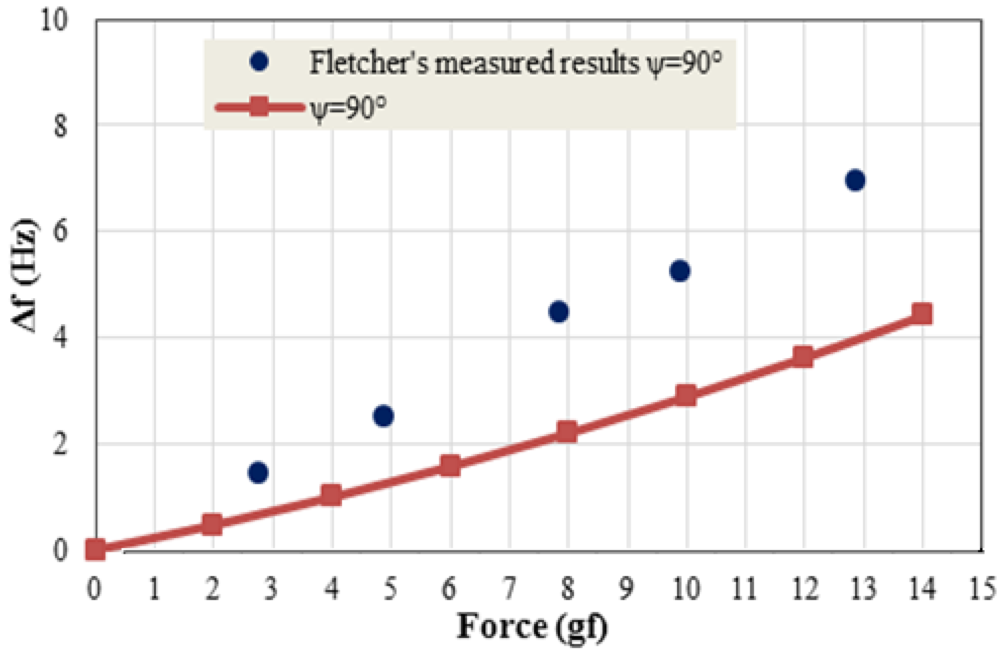

Figure 5.17: Frequency change as a function of applied force for symmetrical bending of *SC*-cut circular plate resonator for azimuth angle ψ = 90°.

5.5 Rectification in *AT*-cut and *SC*-cut Resonators in Cantilever Bending

The phenomenon of rectified acceleration sensitivity had been addressed in chapter 4 for the 1 GHz resonator in which the sign of frequency change Δf is independent of the sign of applied force or acceleration. For our study of cantilever plate bending in *AT*-cut and *SC*-cut circular plate resonators, the bending force was applied in both positive and negative *Y*-axis direction, and the results were shown in Figures 5.18 and 5.19 respectively. We found that for the *AT*-cut crystal, the frequency change was rectified at $\psi = 0^{o}$ and 180^{o}, while for the *SC*-cut crystal, the frequency change was rectified at ψ ~140^{o}, and ~320^{o}. (*Please note that although the red curve (+2 grams-force) and blue curve (-2 grams-force) appear to intersect at frequency change* $\Delta f = 0$, *they in fact intersect at small values of* $\Delta f \neq 0$.)

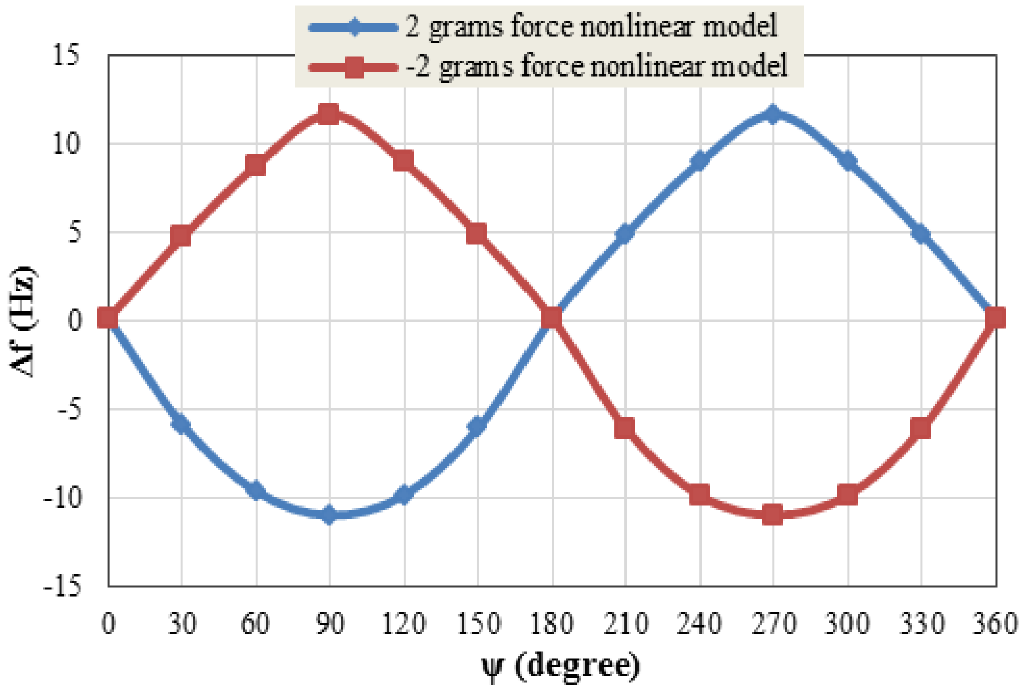

Figure 5.18: Frequency change as a function of azimuth angle ψ for cantilever bending of *AT*-cut circular plate resonator.

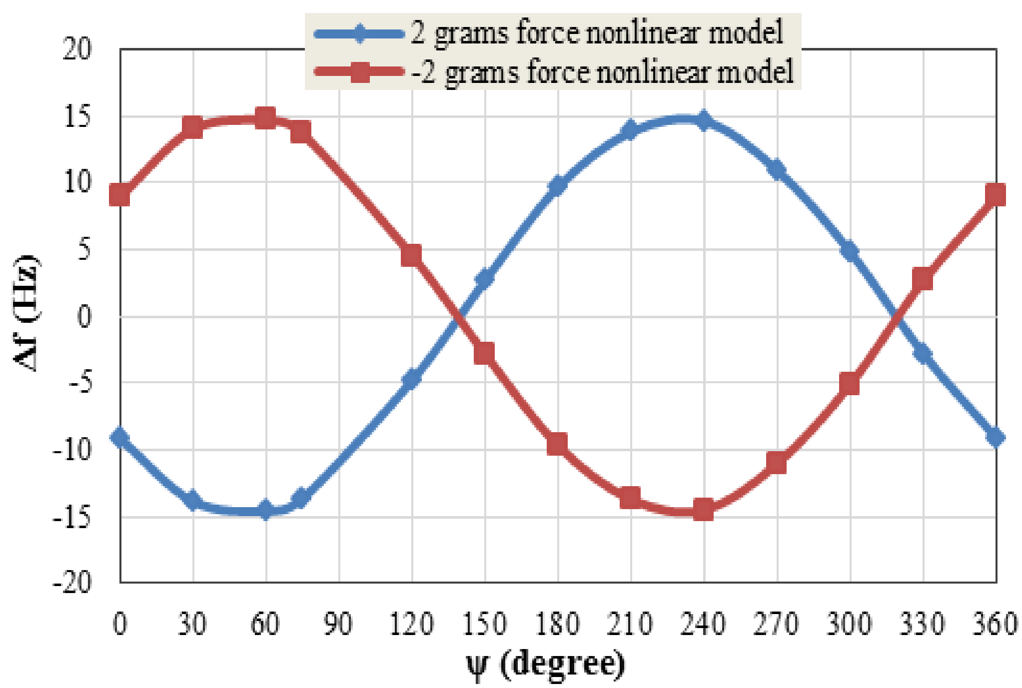

Figure 5.19: Frequency change as a function of azimuth angle ψ for cantilever bending of *SC*-cut circular plate resonator.

5.6 Effects of External Forces on the Third Overtone Frequency

In this section, the effect of external forces on the third overtone thickness shear mode is studied. Circular plates of quartz crystals are respectively subjected to compressional stress applied diametrically to the edges of plate and flexural force in different configurations as function of azimuth angle ψ.

5.6.1 Circular Disk Subjected to Diametrical Forces (Third Overtone Mode)

The experimental setup for circular disk subjected to diametrical forces was discussed in section 5.4, the diameter of plate and the electrodes diameters used in this section are kept the same as before. Here, we will skipped the general discussion and focus on the effects of compressional forces on the third overtone frequency in thickness shear mode.

Figure 5.20 shows the effect of a compressive force (500 grams) on the third overtone thickness shear mode of an *AT*-cut plate as a function of ψ at frequency of 12.36 Mc/s(fundamental f_0=4.12 Mc/s). We observed that the solid red curve compared well with the measured results of Mingins [26]. FEA simulations on the third overtone indicated that the total frequency change for a given force is proportional to overtone shown in Figure 5.21. The solid purple curve and the solid green curve were FEA simulations of frequency change as function of ψ for the third overtone (30.7 Mc/s) and the fundamental mode (10.22 Mc/s) respectively. The solid green curve seemed to match the measured results at the fundamental frequency, and the solid purple curve deviated from the measured results at overtone frequency.

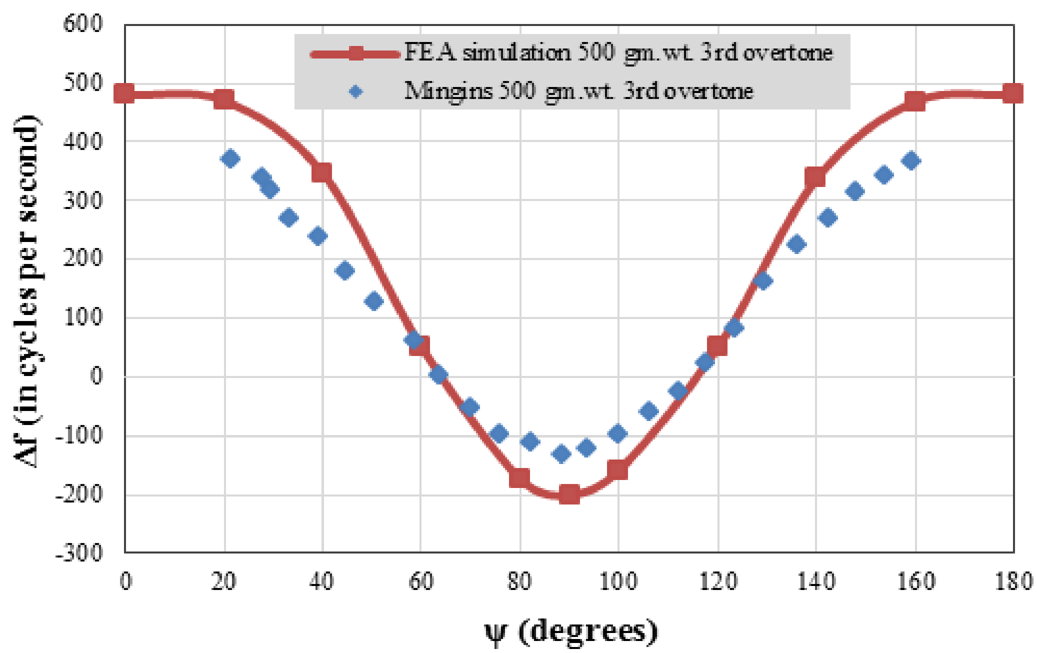

Figure 5.20: Frequency change as function of ψ for compression stress at 3rd overtone frequency of 12.36 Mc/s for *AT*-cut circular plate. (fundamental f_0=4.12 Mc/s).

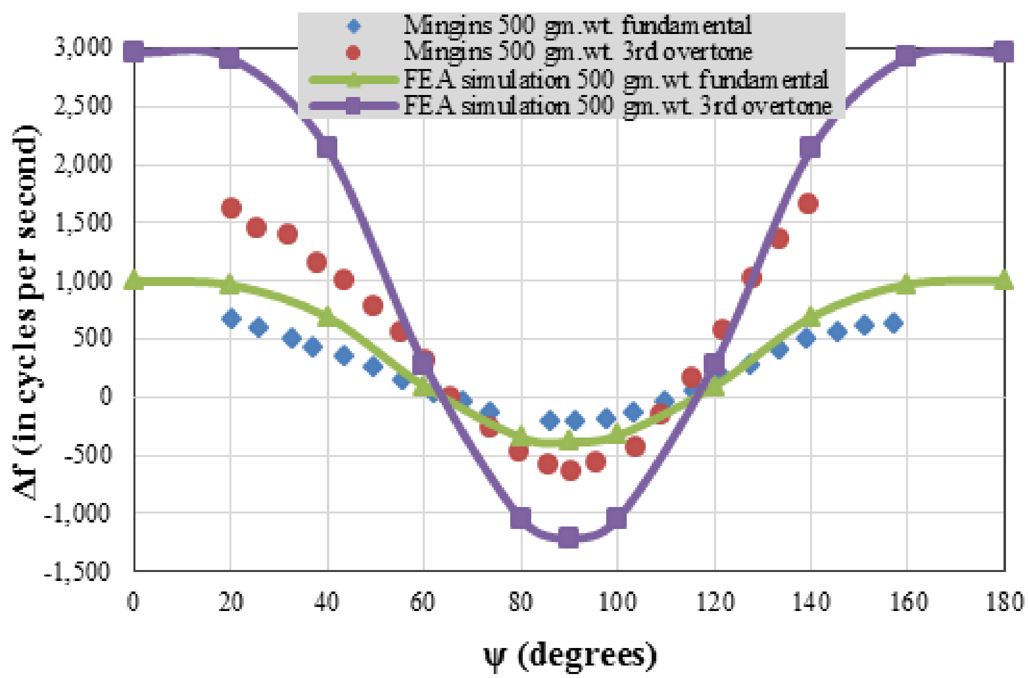

Figure 5.21: Frequency change as function of ψ for compression stress at fundamental frequency of 10.22 Mc/s and 3rd overtone frequency of 30.7 Mc/s for *AT*-cut circular plate.

5.6.2 Clamped Cantilever Bending

In clamped cantilever, the plate was flexed as cantilever clamped near the edge and stressed by a force diametrically opposite the support. The effect of flexural bending on the third overtone thickness shear mode was studied. The crystal plate dimensions were *d=0.5* inch, gold electrodes of 0.25 inch in the center. The plate was clamped at one end with a bending force of 50 grams of weight applied at a point near the opposite end shown in Figure 5.22. The fractional change in frequency ($\Delta f/f_0$) as function of ψ at 3rd overtone frequency of 25.2 Mc/s were compared with Mingins [27] measured results shown in Figure 5.23. Our model results (red curve) showed a trend similar to the experimental data (blue curve) although the magnitude of frequency change were slightly off at some azimuth angles such as 160°,180°,330° and 360°.

Next, we consider the case when the crystal was inverted so that the face which was underneath is now on the top. These results are shown in Figure 5.24 at third overtone frequency of 21.3 Mc/s; the blue curve and the green curve were the experimental measured results due to bending force of 50 grams of weight in the downward direction and 56 grams of weight in the upward direction respectively. The red curve and the purple curve were the FEM results of 50 grams of weight and 56 grams of weight in the downward and upward direction respectively. There is strong evident that an opposite effect exists on the frequency change as function of ψ, and it depends on the direction of applied bending force. The results of positive or negative bending forces showed that both of the negative Δf regions have the similar configuration and this is true for both of the positive Δf regions as well. We also found that for *AT*-cut crystal, it was rectified at ψ

= 0° and 180° meaning Δf was always positive regardless of the sign of the applied bending force.

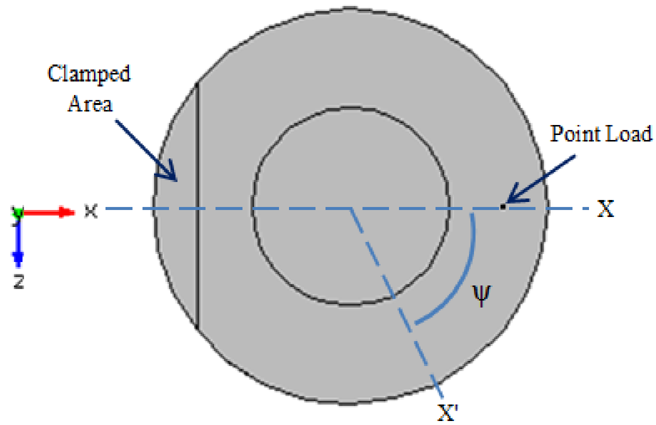

Figure 5.22: Clamped cantilever bending of *AT*-cut circular plate.

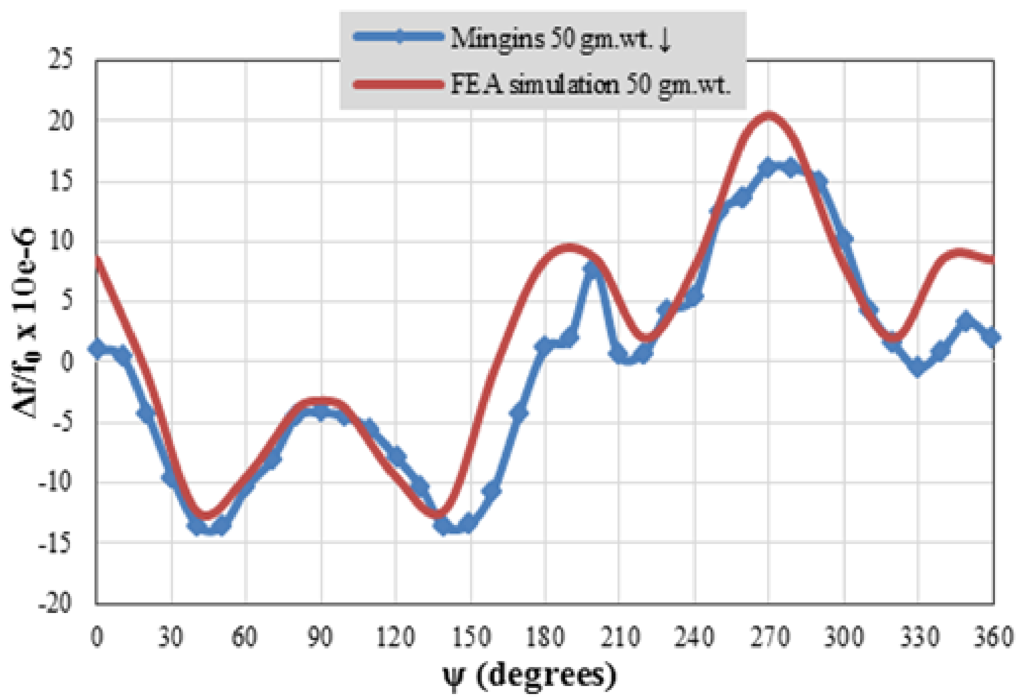

Figure 5.23: Frequency change as a function of azimuth angle ψ for cantilever bending at 3rd overtone frequency of 25.2 Mc/s for *AT*-cut circular plate. (d/h=60.5)

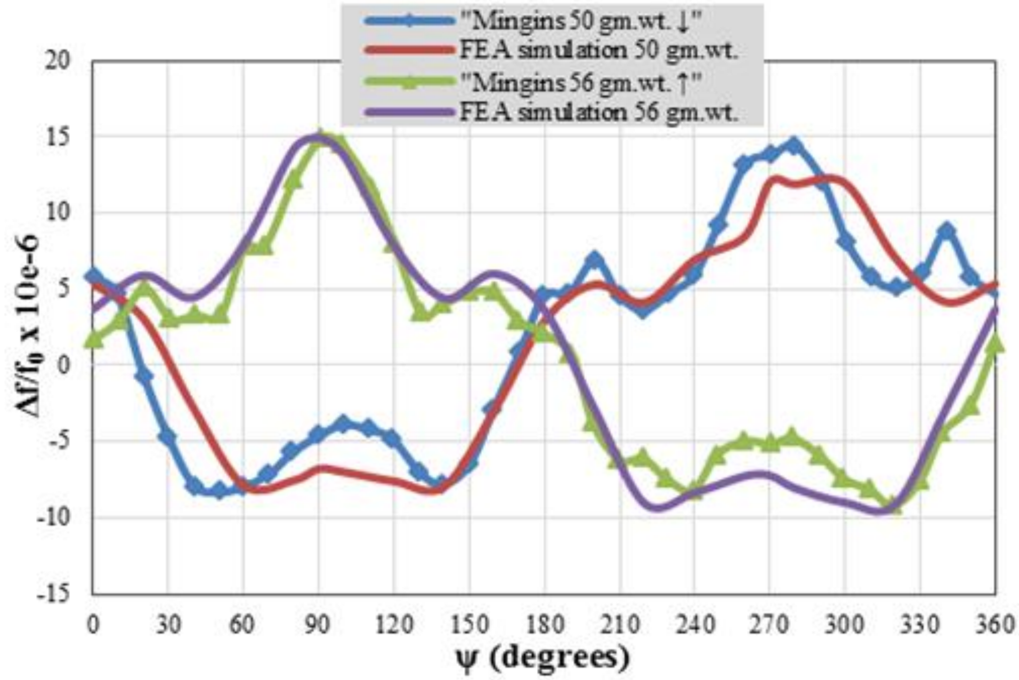

Figure 5.24: Frequency change as a function of azimuth angle ψ for cantilever bending at 3rd overtone frequency of 21.3 Mc/s for *AT*-cut circular plate. (d/h=54)

5.6.3 Knife Edge Cantilever Bending

In this section, we studied the effect of third overtone frequency change as function of ψ with knife edge cantilever support. The traditional clamped support was replaced with two knife edges one on the top and one on the bottom with bending force applied on the opposite end shown in Figure 5.25. The 21.3 Mc/s *AT*-cut plate with knife edge cantilever support and applied bending force of 85 grams of weight is studied and the result is shown in Figure 5.26. We have found that our FEA model (red curve) matched well with the measured results by Mingins (blue curve). The general shape of the frequency change curve was very similar to the frequency change curve of clamped cantilever support. The maximum frequency change occurred at ψ= 270°, same as the clamped cantilever configuration. Therefore, we believed that the knife edge supports produce similar bending effect as the clamped support.

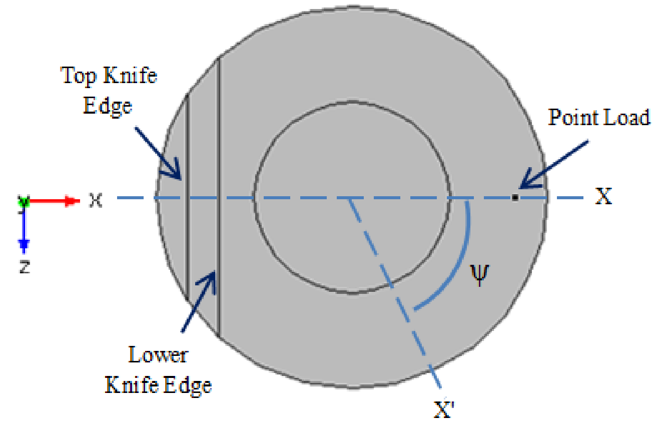

Figure 5.25: Knife edge cantilever bending of *AT*-cut circular plate.

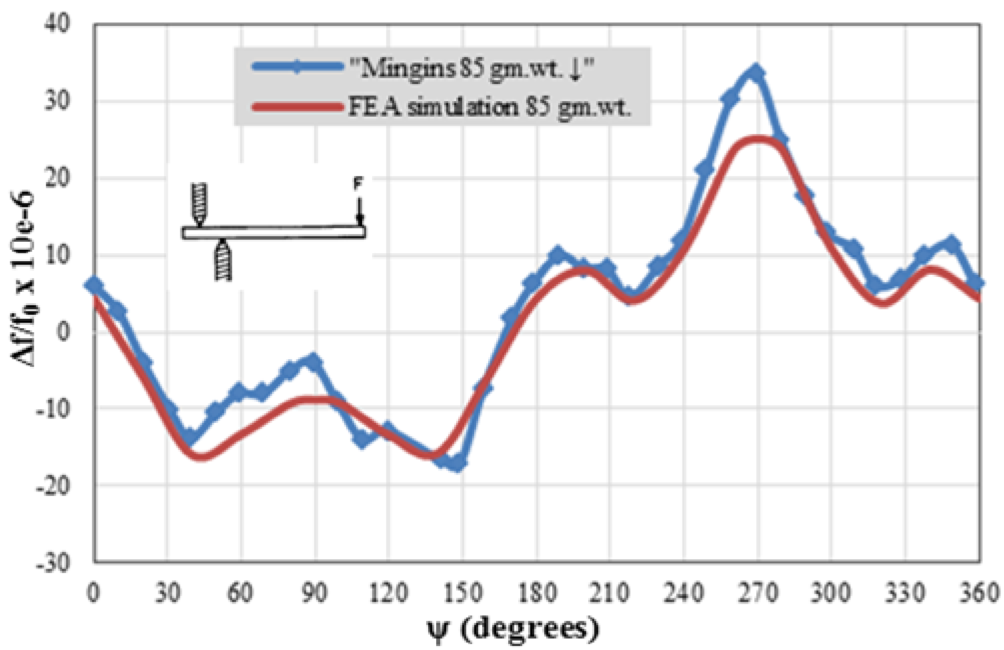

Figure 5.26: Frequency change as a function of azimuth angle ψ for knife edge cantilever bending at 3rd overtone frequency of 21.3 Mc/s for *AT*-cut circular plate. (d/h=54)

5.6.4 Dual Support (Symmetric) Bending

In dual support mounting, a bending force was applied so as to produce a maximum deflection in the middle while the plate was supported near the ends of diameter. In order to carry out symmetrical bending about a diameter of plate, the lower knife edge support was moved to a position under the center of the plate. The central section of the knife edge is ground away so that it does not touch the plated electrode area in the center of the plate. This should give a direct result on the effect of frequency change due to symmetric bending. Figure 5.27 shows our model of symmetric bending configuration. Initially the plate was subjected to bending force of 150 grams of weight on the top face (A side) then on the bottom face (B side) shown in Figure 5.28. The plate is turned over so that the face which was underneath is now on the top.

The results of 3rd overtone frequency change as function of ψ is shown in Figure 5.29 for an *AT*-cut circular plate. The blue curve and the green curve were experimental measured results due to bending force of 150 grams of weight on the A side and B side respectively. Our model results (red curve and the purple curve) showed a trend similar to the measured results although the magnitude of frequency changes were off at ψ= 180° and 270°. Note that only the purple curve could be seen in the graph because it overlapped the red curve. According to Mingins [27], this "turn over" should produce two identical curves because of the perfect symmetry in dual support mounting and such "turn over" must be a rotation about the *X*-axis. Our FEA simulation showed good agreement with his finding although actual experimental results shown variations due inaccurate measurement of ψ with respect to *X*-axis upon inversion of the plate.

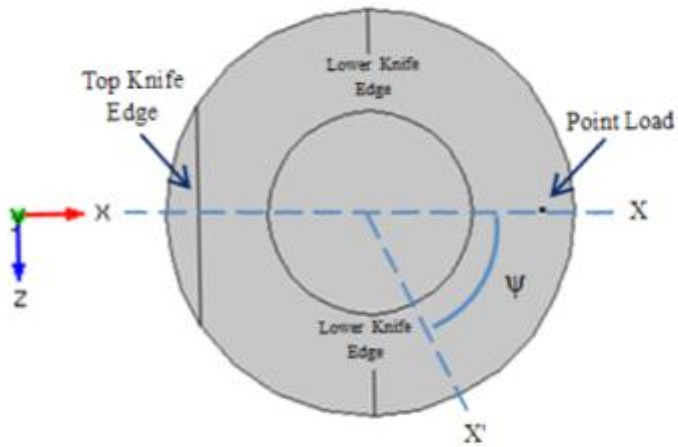

Figure 5.27: Symmetric bending of *AT*-cut circular plate.

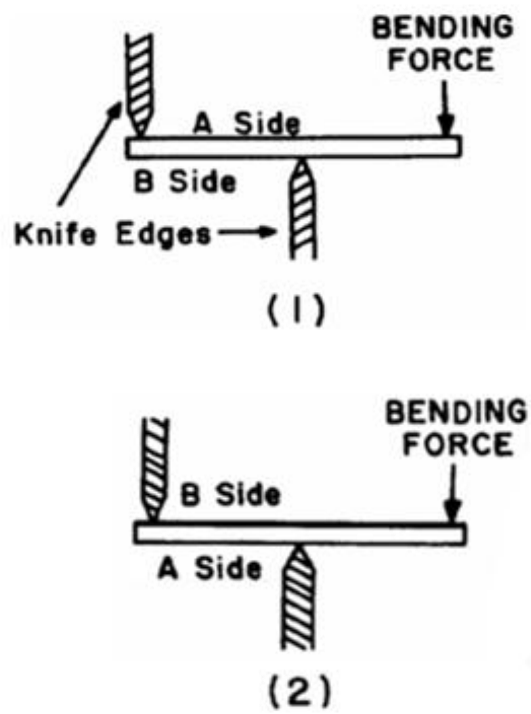

Figure 5.28: Symmetrical bending of circular plate by Mingins [27].

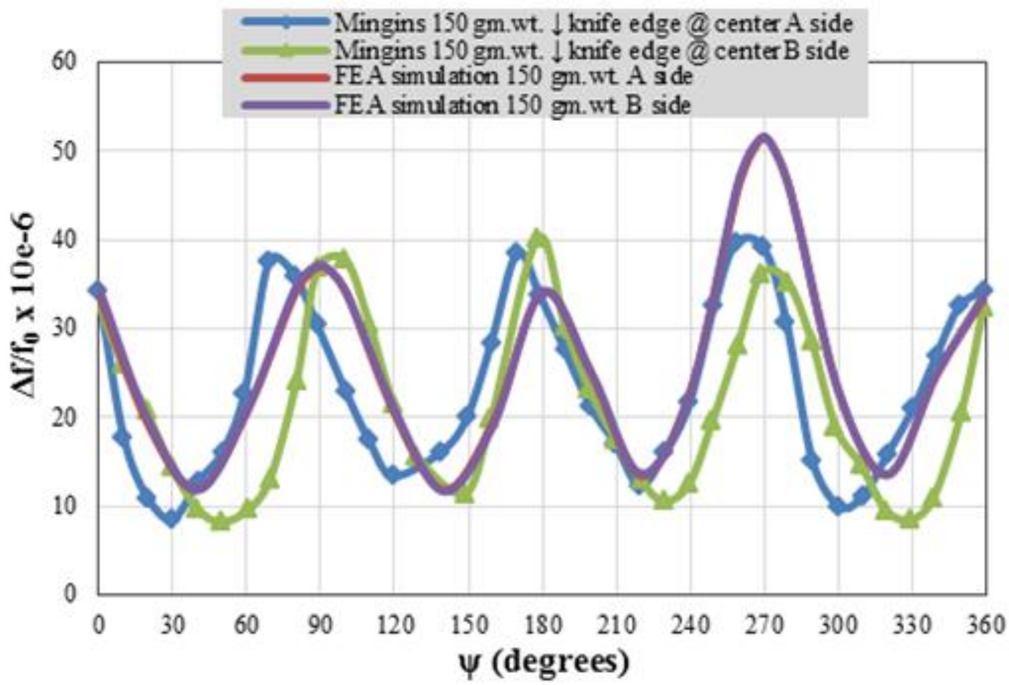

Figure 5.29: Frequency change as a function of azimuth angle ψ for symmetric bending at 3rd overtone frequency of 18.4 Mc/s for *AT*-cut circular plate. (d/h=46)

We also examined the scenario when the lower knife edge was progressively moved from the center of the plate to positions near the top of knife edge, where the mount would become more of the cantilever configuration shown in Figure 5.30. “X” is the distance between the two knife edges. It was reduced from the center 0.25 inch to 0.04 inch in several steps. Figures 5.31 and 5.32 shown the change in frequency as function of ψ at knife edge position X= 0.132 inch and X=0.097 inch respectively. In Figure 5.31, our model results (red curve) showed a trend similar to the measured results (blue curve) with some variation at azimuth angles such as 80° and 270˚. At knife edge position X=0.132 inch, the overall trends of the Δf curve has the same characteristics as the Δf curve of the symmetric bending in Figure 5.29. Figure 5.32 shows our model result at knife edge position X=0.097 inch (purple curve) with the measured results by Mingins (green curve). The two curves exhibit variation, with the measured Δf curve resembles the symmetric bending plot in Figure 5.29, while the FEA model results resemble the Δf curve of knife edge cantilever bending plot in Figure 5.26. This leads to the conclusion that as “X” diminishes, the shape of the frequency change curve tends toward a typical cantilever bending plot.

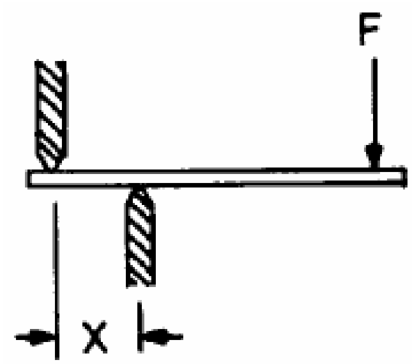

Figure 5.30: Transition from dual support to cantilever.

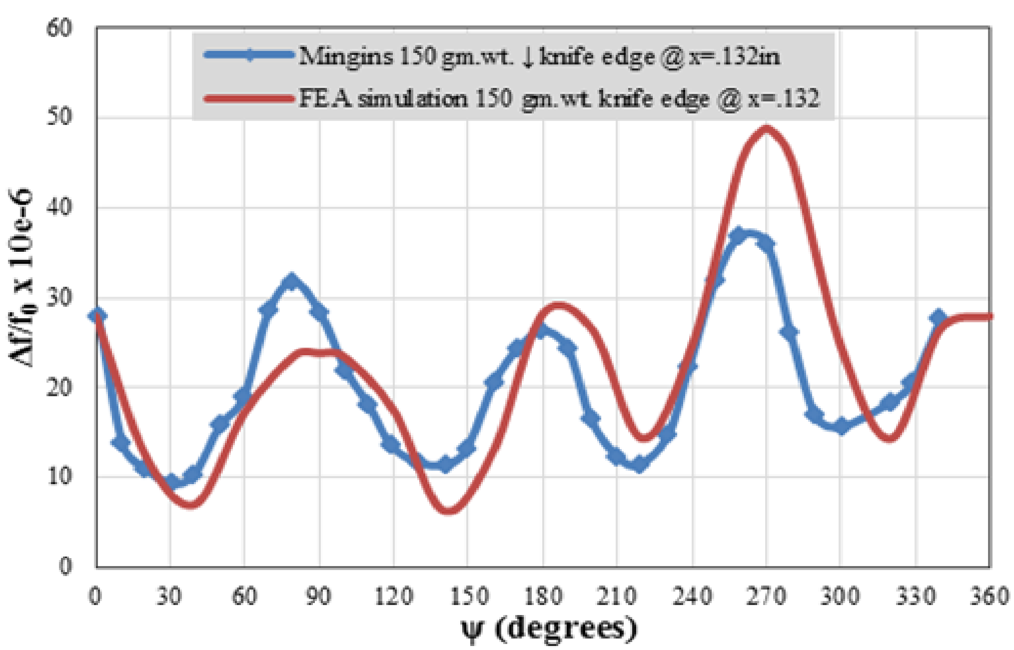

Figure 5.31: Frequency change as a function of azimuth angle ψ for knife edge position x=0.132 inch at 3rd overtone frequency of 18.4 Mc/s for *AT*-cut circular plate. (d/h=46)

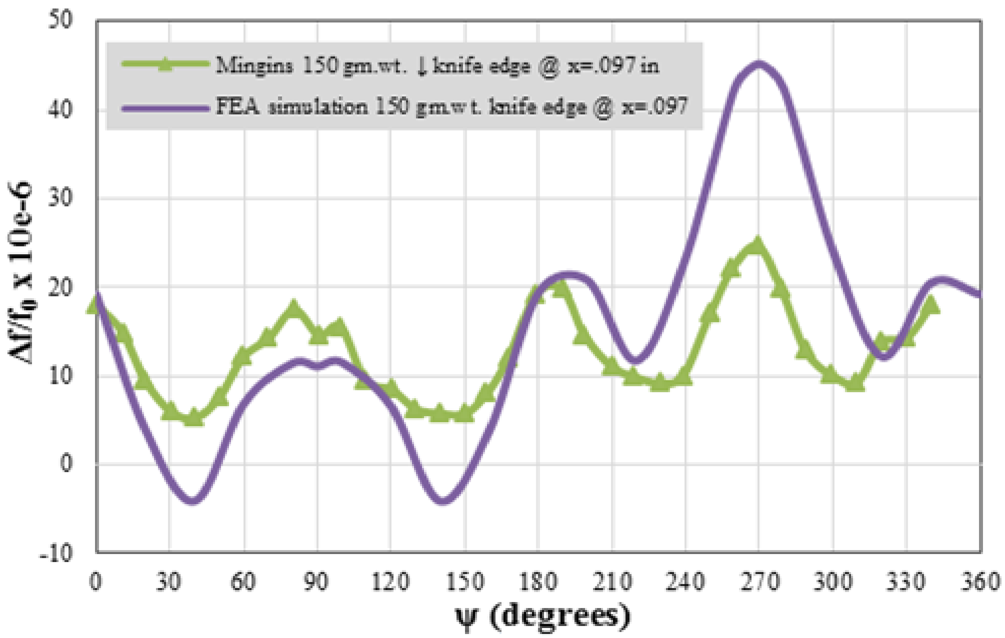

Figure 5.32: Frequency change as a function of azimuth angle ψ for knife edge position x=0.097 inch at 3rd overtone frequency of 18.4 Mc/s for *AT*-cut circular plate. (d/h=46)

5.7 Summary of Analysis

Incremental equations for small vibration superposed on initial deformation were implemented in COMSOL to study the effect of external forces on the frequency of circular plate subjected to compressional forces and bending moments. The model results using nonlinear initial strains showed good agreement with measured results of Mingins [26, 27] and Fletcher [38] when the plate is subjected to bending, while linear initial strains is only good for plate subjected to diametrical forces. We concluded that the present nonlinear model is effective and suitable for studying effect of external forces on the frequency of crystal plate.

A summary of our finding are as follow:

1) The assumptions of linear initial stresses/strains are only adequate for in-plane compressional forces while for out-of-plane bending the nonlinear initial stresses/strains are needed.

2) Rectified acceleration sensitivity for the *AT*-cut crystal was found at $\psi = 0^o$ and 180^o; while for the *SC*-cut crystal, the rectified acceleration sensitivity was found at $\psi \sim 140^o$, and $\sim 320^o$.

3) For *AT*-cut, the critical angles for frequency insensitive to compressional force have been found when azimuth angle ψ is around 65° and 115°. Also the total frequency change for a given force is proportional to overtone.

4) The “turn over test” of crystal plate in dual support bending showed that *X*-axis is an axis of symmetry for *AT*-cut plate.

5) By varying the position of the lower knife edge support, the transition from the dual support configuration to the cantilever is resulted.

Chapter 6 Effect of Thermal Stresses on the Frequency-Temperature Behavior of Quartz Resonators

6.1 Introduction

The temperature behavior of a quartz resonator is one of the most important technical parameters. Temperature change creates thermal strains which caused the resonant frequencies to change. There are two types of temperature effects. The first type is static frequency-temperature behavior in which heat exchange is slow enough so the resonator is in thermal equilibrium, the effects of temperature gradients is negligible (Isothermal changes). The static f vs. T characteristics of crystal are determined primarily by the angle of cut of the crystal plates with respect to the crystallographic axes of quartz. The second type is the dynamic frequency-temperature behavior in which the resonator is not in thermal equilibrium, the temperature surrounding produces thermal gradients where heat flows to or from active area of the resonator. This usually occurs during warm-up period where there is significant thermal transient effect in the resonator. In this dissertation, we will focus only the static f vs. T behavior of quartz resonator.

A quartz resonator usually consists of a quartz plate sandwiched between two electrode films. Currently, quartz resonators are analyzed and designed by assuming the electrode films as mass loading films. This assumption however is only valid for the lower frequency resonators in the high frequency (HF) and VHF ranges. For the ultra-high frequency (UHF) quartz resonators, the effect of electrode stress is quite significant. Electrode stresses on the surface of the quartz resonator causes shifts in the resonant frequencies through third order elastic constant effects in the quartz [65]. Stresses in thin films are a common occurrence for all metallization processes due to differences in thermal expansion coefficients between the electrode films and the quartz. The electrodes would expand/contract thermally at different rate as to quartz and thus would induce thermal stresses and strains.

Although temperature stable quartz resonators are made of quartz plates with cut angles known to have stable frequencies over a range of temperature, other factors such as mounting stresses, and thermal stresses and strains in the plate could cause the resonant frequency to change [66]. Since in many cases the electrodes are deposited on the quartz, the effects of thermal stresses are transmitted from the electrode films to the quartz plate, and then redistributed over the entire volume of the quartz plate. In this chapter, we present a new method in which the electrode stress can be used to improve the frequency-temperature behavior of UHF quartz resonator. We study the UHF thickness shear quartz resonator as a composite plate wherein not only the mass loading effect but the electrode films material properties such as linear, nonlinear elastic constants, temperature derivatives of elastic constants and thermal expansion coefficient are incorporated into our COMSOL model for the vibrations of a composite plate superposed on initial strains.

6.2 Equations of Incremental Motion Superposed on Thermally Induced Deformations

The governing equations for small vibrations superposed on initial stresses and strains were derived by Lee, Wang and Markenscoff [28] where the Piola-Kirchhoff stress tensor of the second kind was employed in a Lagrangian formulation. Past studies of acceleration sensitivity and force-frequency effects have employed these governing equations for small vibration superposed on initial stresses and strains without the temperature effects. The same set of equations (5.3-5.7) could be employed for the frequency-temperature effects since the thermal stresses and strains could be treated as initial stresses and strains in the resonator.

Incremental displacements:

$$u_i = \bar{U}_i - U_i, \tag{6.1}$$

Incremental strains:

$$s_{ij} = \tfrac{1}{2}(u_{i,j} + u_{j,i} + U_{k,i}u_{k,j} + U_{k,j}u_{k,i}), \tag{6.2}$$

Incremental stresses:

$$t_{ij} = \left(C^E_{ijkl} + C^E_{ijklmn}S_{mn}\right)s_{kl}, \tag{6.3}$$

Incremental stress equations of motion:

$$(t_{ij} + t_{jk}U_{i,k})_{,j} = \rho\ddot{u}_i \quad in \;\; V\,, \tag{6.4}$$

$$p_i = n_j\left(t_{ij} + t_{jk}U_{i,k}\right) \;\; on \;\; S, \tag{6.5}$$

where C^E_{ijkl} and C^E_{ijklmn} are the second and third order elastic stiffness of the crystal. The term $U_{i,k}$ and S_{mn} are respectively the initial displacement gradients and initial strains.

The governing equations for the static f-T model could be written in the same form as equations (6.1-6.5), when the resonator is allowed to freely expand with temperature.

Initial thermal strain:

$$S_{ij} = \alpha^\theta_{ij} + \frac{1}{2}\alpha^\theta_{ki}\alpha^\theta_{kj}, \tag{6.6}$$

$$\alpha^\theta_{ij} = \; \alpha^{(1)}_{ij}\,\theta + \; \alpha^{(2)}_{ij}\,\theta^2 + \; \alpha^{(3)}_{ij}\,\theta^3, \tag{6.7}$$

$$\theta = T - T_0, \tag{6.8}$$

where $\alpha^{(1)}_{ij}$, $\alpha^{(2)}_{ij}$, and $\alpha^{(3)}_{ij}$ are respectively the first, second and third order thermal expansion coefficient and θ is the temperature increment with respect to reference temperature $T_0 = 25$ ℃. The quadratic terms in equation (6.6) is neglected and we equate thermal strains to the mechanical strains for the stress-free temperature behavior

$$S_{ij} = \alpha_{ij}^{\theta} = U_{i,j}. \tag{6.9}$$

Hence incremental equations (6.2-6.5) can be written in terms of thermal strains for stress-free case.

Modified incremental strains:

$$s_{ij} = \frac{1}{2}\left(u_{j,i} + u_{i,j} + \alpha_{kj}^{\theta} u_{i,j} + \alpha_{ki}^{\theta} u_{j,i}\right), \tag{6.10}$$

Modified incremental stress:

$$t_{ij} = (C_{ijkl}^{\theta} + C_{ijklmn}^{E}\, \alpha_{mn}^{\theta}) s_{kl}, \tag{6.11}$$

$$C_{ijkl}^{\theta} = C_{ijkl} + C_{ijkl}^{(1)}\theta + {}^{1}/_{2}\tilde{C}_{ijkl}^{(2)}\theta^2 + {}^{1}/_{6}\tilde{C}_{ijkl}^{(3)}\theta^3, \tag{6.12}$$

Modified stress equation of motion:

$$(t_{ij} + t_{jk}\alpha_{ik}^{\theta})_{,j} = \rho \ddot{u}_i \quad in\ \ V, \tag{6.13}$$

$$p_i = n_j\left(t_{ij} + t_{jk}\alpha_{ik}^{\theta}\right) \ on\ \ S, \tag{6.14}$$

For resonator under thermal stress condition, incremental equation (6.2-6.5) can be written as follow:

Modified incremental strains:

$$s_{ij} = \frac{1}{2}\left(u_{j,i} + u_{i,j} + U_{k,i}u_{k,j} + U_{k,j}u_{k,i}\right), \tag{6.15}$$

Modified incremental stress:

$$t_{ij} = (C_{ijkl}^{\theta} + C_{ijklmn}^{E}\, S_{mn}) s_{kl}, \tag{6.16}$$

$$C_{ijkl}^{\theta} = C_{ijkl} + C_{ijkl}^{(1)}\theta + {}^{1}/_{2}\tilde{C}_{ijkl}^{(2)}\theta^2 + {}^{1}/_{6}\tilde{C}_{ijkl}^{(3)}\theta^3, \tag{6.17}$$

Modified stress equation of motion:

$$(t_{ij} + t_{jk}U_{i,k})_{,j} = \rho \ddot{u}_i \quad in\ \ V, \tag{6.18}$$

$$p_i = n_j\left(t_{ij} + t_{jk}U_{i,k}\right) \ on\ \ S, \tag{6.19}$$

where C^{θ}_{ijkl} is modified second order elastic constants, $C^{(1)}_{ijkl}$, $\tilde{C}^{(2)}_{ijkl}$, and $\tilde{C}^{(3)}_{ijkl}$ are respectively first, effective second and effective third temperature derivative of the elastic constants. Equations (6.15-6.19) containing temperature derivatives of elastic stiffness as well as the second and third order temperature derivative of piezoelectric and dielectric constants are used in the finite element model to study frequency-temperature behavior of quartz plates with mass loading and as composite plates with electrode films in the next section.

6.3 Comparison of Sekimoto Measured Data with 3-D FEM Results

Rectangular *AT*-cut quartz plate resonators have been widely used in frequency applications. The frequency stability of the resonators is sensitive to temperature change. We studied the frequency-temperature behavior of a rectangular *AT*-cut quartz plate with a length of 13.964mm, a thickness of 1.737mm, and a width of 7mm at 25 ℃ shown in Figure 6.1. The plate undergoes uniformed thermal expansion or contraction while resonant frequencies of certain modes are being measured. The accuracy of the Lagrangian formulation and the material constants of quartz are demonstrated by comparing some 3-D FEM results with measured results by Sekimoto [67].

The fundamental thickness shear frequency is about 0.956 MHz shown in Figure 6.2. Figures 6.3 shows a comparison of measured thickness shear f-T curve with f-T curve obtained using FEM and the comparison is quite good. The resonance at 1.003 MHz is the thickness flexural vibration strongly coupled with thickness shear mode shown in Figure 6.4. The f-T behavior of thickness flexural mode is shown in Figure 6.5. Overall, the f-T curves obtained using the static f-T model is in very good agreement with the measured results.

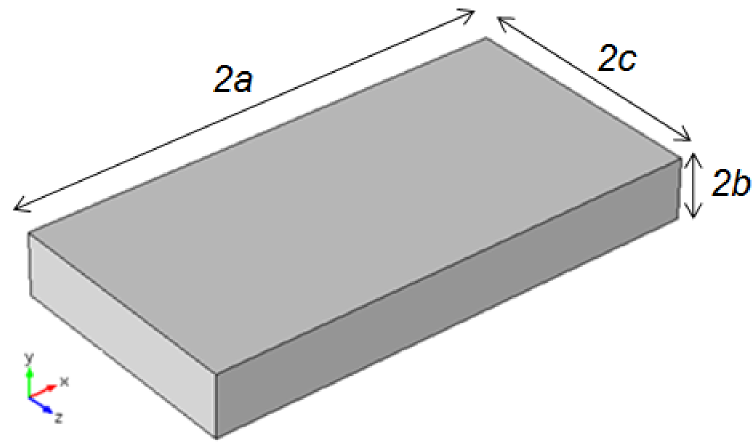

Figure 6.1: Sekimoto rectangular *AT*-cut quartz plate.

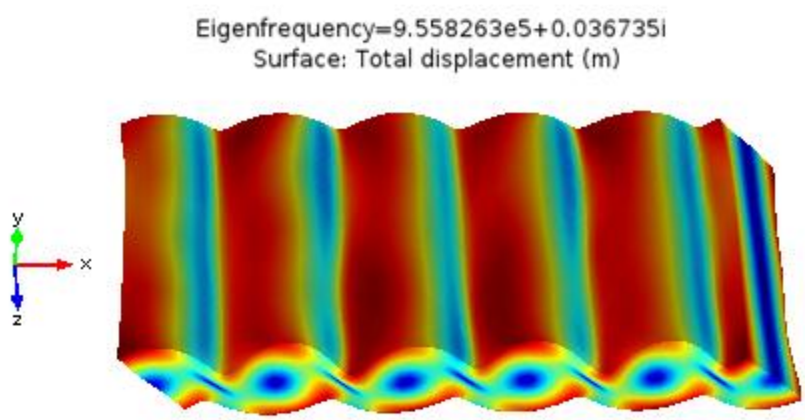

Figure 6.2: Thickness shear mode 0.956 MHz.

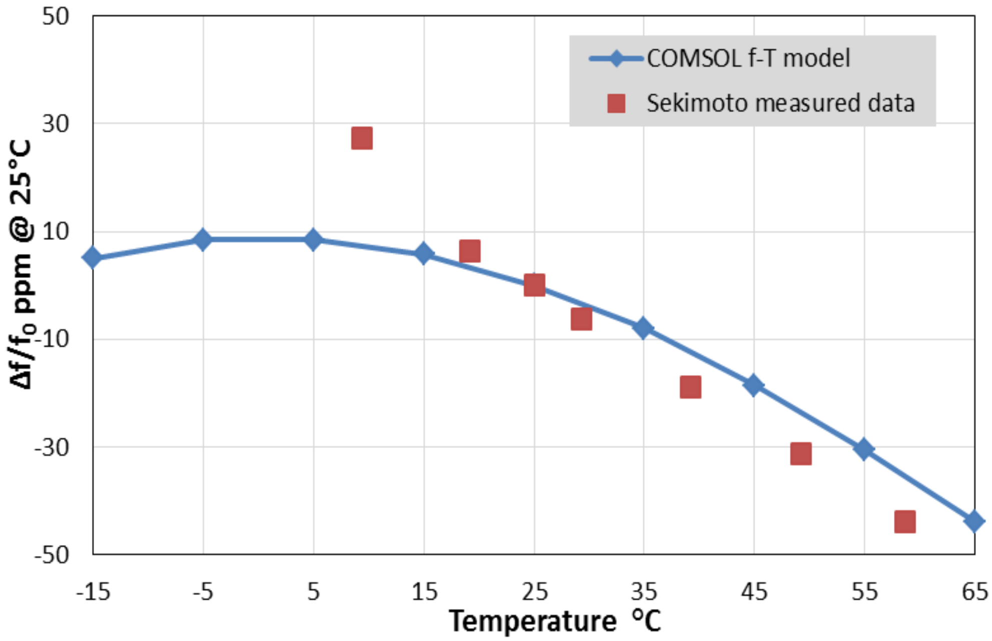

Figure 6.3: Thickness shear (0.956 MHz) frequency-temperature curve.

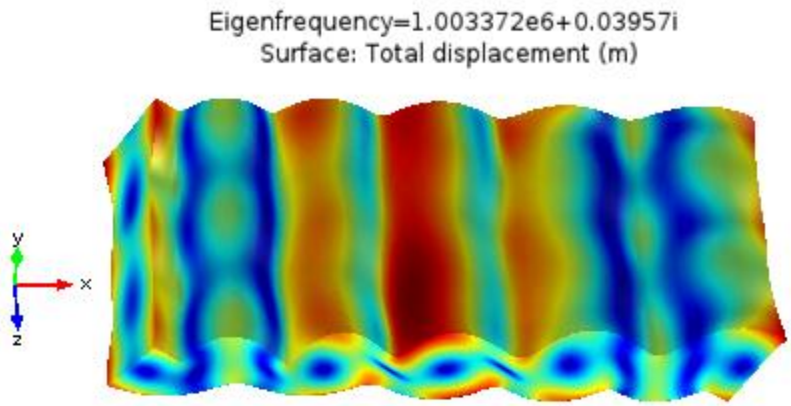

Figure 6.4: Thickness flexural mode 1.003 MHz.

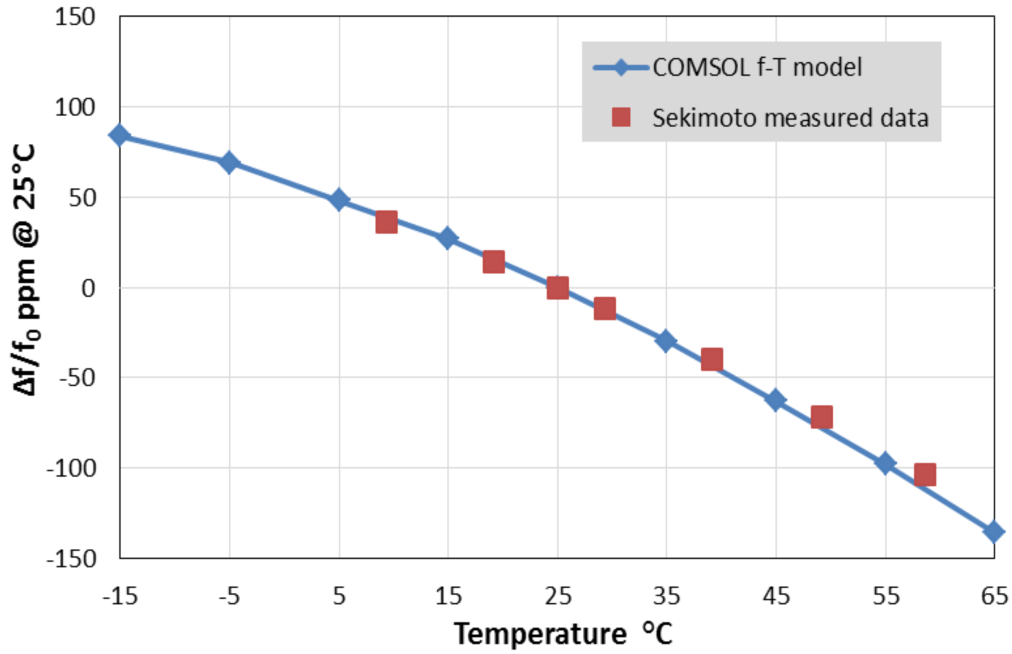

Figure 6.5: Thickness flexural (1.003 MHz) frequency-temperature curve.

6.4 The Origin of Electrode Film Stresses

There are intrinsic and extrinsic stresses in electrode films. Intrinsic stress comes from defects such as dislocations of atoms in the films during deposition. The origin of extrinsic stress in a thin film comes mainly from adhesion of electrodes to the quartz [68]. Thermal stresses and strains are induced due to differences in thermal expansion coefficients between the electrode films and the quartz.

Let us consider an aluminum film on a quartz substrate in order to illustrate the stresses and strains induced by differences in thermal expansion coefficients. The coefficient of thermal expansion of aluminum ($23.1\text{x}10^{-6}$/°C) is about twice that of quartz. When aluminum is deposited on to quartz at elevated temperature and then cooled to room temperature, the aluminum film will shrink more than quartz. The quartz substrate will restrict the aluminum film from doing so. Hence in cooling, the aluminum is under tension while the quartz is under compression. Assuming much of this stress relaxes after sitting in room temperature for several days, the stresses reverse upon heating up. The aluminum expands more than quartz, and again it is restricted by the quartz substrate. The aluminum is under compression while quartz is under tension. The stress due to differential thermal expansion experienced by the thin film is biaxial shown in Figure 6.6. The stresses act along the two principal axes in the plane of the film. There is negligible stress in the direction normal to the film free-surface but there is strain in the normal direction.

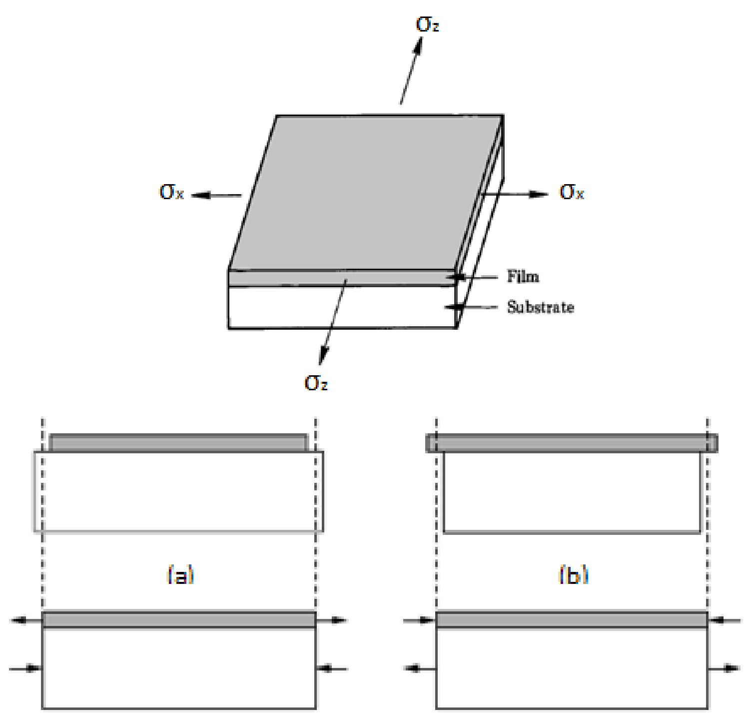

Figure 6.6: Stresses in thin film (a) tensile stress in film; (b) compressive stress in film.

6.5 Frequency-Temperature Behavior of High Frequency Resonators

A stable frequency-temperature behavior of a resonator is an important operational parameter in electronic devices. The stress effect has been a concern to many investigators in the MEMS community. We first demonstrate the effect of electrode stresses on frequency-temperature behavior of a circular 10 MHz fundamental mode *AT*-cut resonator. The resonator is 12mm in diameter with plate thickness of 0.1655mm, and aluminum electrodes of 4mm in diameter at the center as shown in Figure 6.7. The f-T curves were obtained by treating the electrode films as mass loading films and composite plate effects, respectively. The results are shown in Figure 6.8.

In Figure 6.8, the f-T curve for the case of mass loading (purple line) is one in which the plate resonator is initially stress-free and undergoes homogeneous thermal expansion/contraction with uniform temperature change. For the aluminum-quartz composite plate (blue line) and chromium-aluminum-quartz composite plate (red line), stresses occur in the plate resonator when the temperature is different from the reference temperature T_0=25 ℃. The f-T curves look very similar between the mass loading effect and the composite plate effect at temperature between 5 ℃ to 55 ℃. There are differences in the curves between the mass loading effect and composite effect near the two temperature extremes. The composite plate effect tends to rotate the f-T curve clockwise from the curve with mass loading effect. Since the ratio of electrode film thickness to quartz plate thickness is small, the mass loading assumption is valid. Overall, the f-T curve for the 10 MHz mass loading case and the composite plate case is within +-7 ppm.

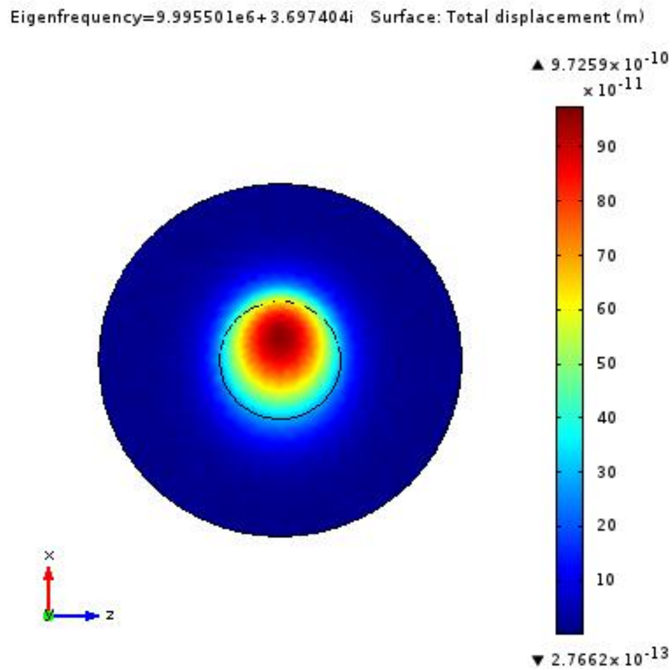

Figure 6.7: Thickness shear mode of 10 MHz *AT*-cut resonator.

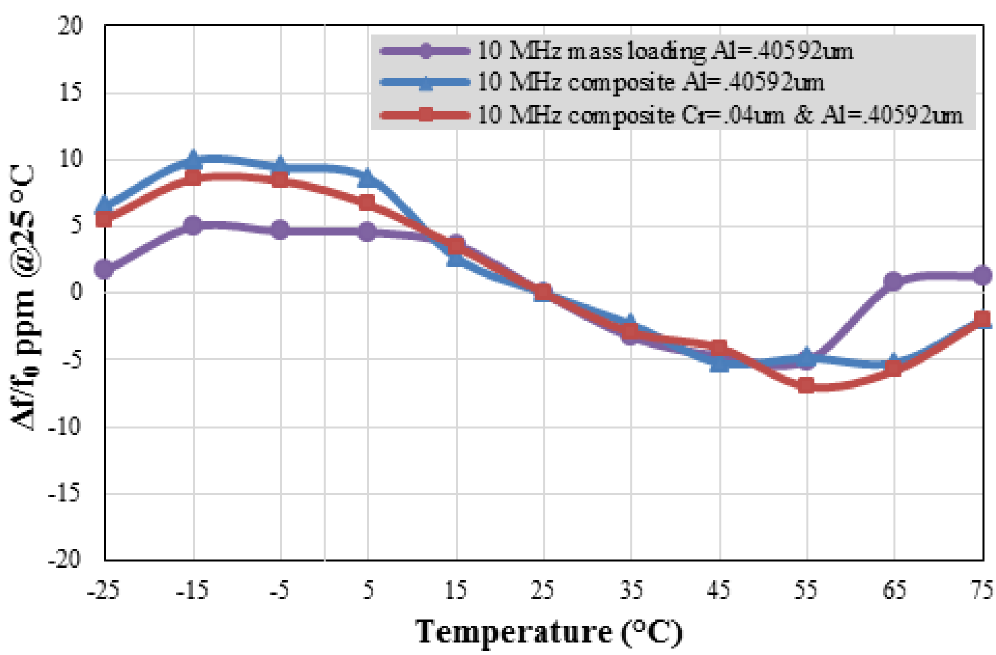

Figure 6.8: f-T curve for the 10 MHz *AT*-cut resonator (θ = 35.25°).

6.6 Frequency-Temperature Behavior of Ultra-High Frequency Resonators

For ultra-high frequency quartz resonator, the effect of electrode stress is quite significant. We consider a rectangular 1 GHz *AT*-cut quartz plate resonator (*l*=235µm, *w*=105µm, *t*=1.5µm) with aluminum electrodes (150x50x0.04µm). For simulation purposes, the resonator was cantilever mounted to an absorbing strip of silicon rubber shown in Figure 6.9.

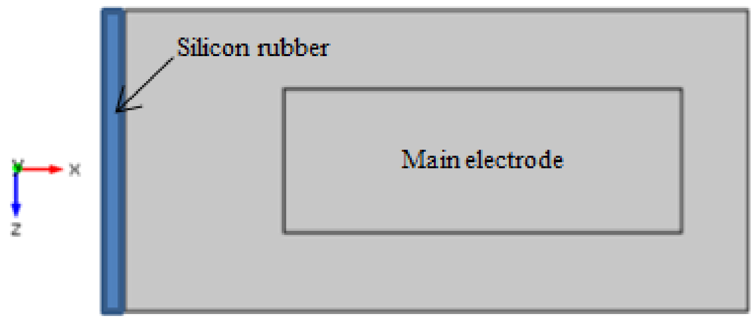

Figure 6.9: Rectangular 1 GHz *AT*-cut plate cantilever mounted.

Since the properties of quartz depend strongly on the cut angles of the crystal plate, frequency change as function of temperature for the 1 GHz *AT*-cut resonator (quartz-aluminum composite) with their cut angles differ slightly is shown in Figure 6.10. Figure 6.10 shows the angles at which the crystal are cut have large influence on the f-T behavior. As the cut angle increases, it tends to rotate the f-T curve in the clock-wise direction. When using the most appropriate cut angle, the f vs. T curve will stay within ±10 ppm over a temperature range of -35 ℃ to 85 ℃. Since quartz manufactures don't usually carry all angles for *AT*-cut, the cost of these specific crystals is relative high.

Thermally induced mounting stresses in the 1 GHz *AT*-cut quartz resonator (mass loading films) have been modeled and its effect on the f-T behavior is analyzed. Increasing the mounting stiffness of silicon rubber from E=2E8 Pa to E=2E12 Pa produces a slight counter-clockwise rotation of the f-T curve shown in Figures 6.11 and 6.12. In a properly mounted resonator, negligible amount of thermal stress is induced in the active region.

The effects of stresses in the electrode films on the frequency-temperature curve can be demonstrated. We can impose bi-axial stresses in the thin films by treating the film stresses as initial stresses in addition to the induced thermal stress. Figure 6.13 shows the 1 GHz *AT*-cut resonator subjected respectively to tensile and compressive stress in the electrode films. The blue line is the case without initial stress; the red line and the green line have initial tensile stress of 10 Mpa and -10 Mpa respectively. A positive tensile stress in the electrode film shifts the f-T curve upward while a negative tensile stress in the electrode film shifts the f-T curve downward.

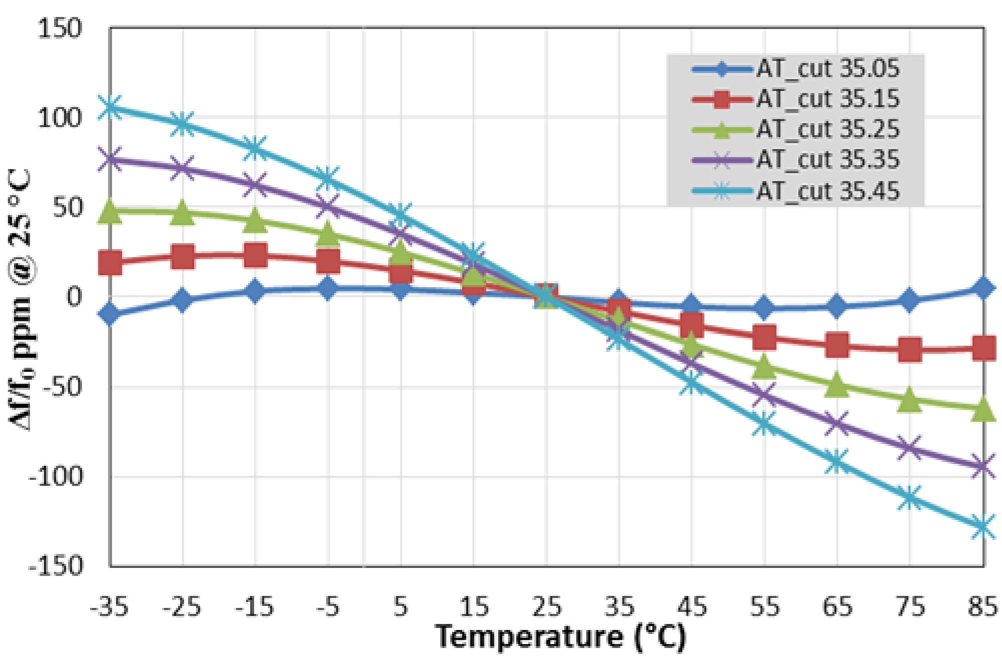

Figure 6.10: Family of frequency-temperature curves for 1 GHz *AT*-cut resonator.

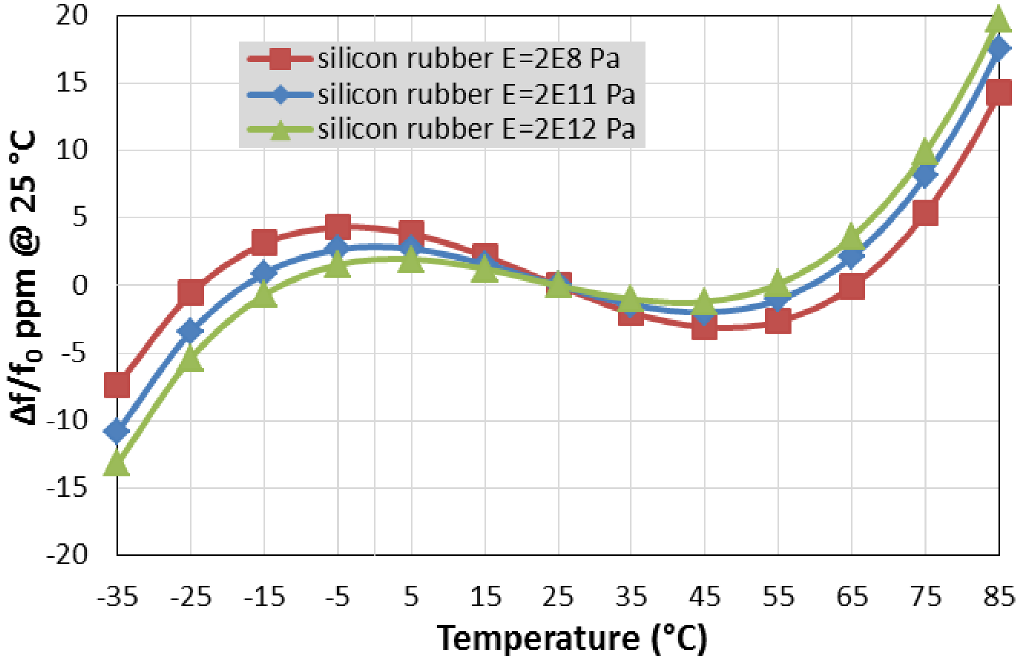

Figure 6.11: f-T characteristic of 1 GHz *AT*-cut resonator (θ = 35.25°) with different mounting stiffness. (Frequency deviation in ppm)

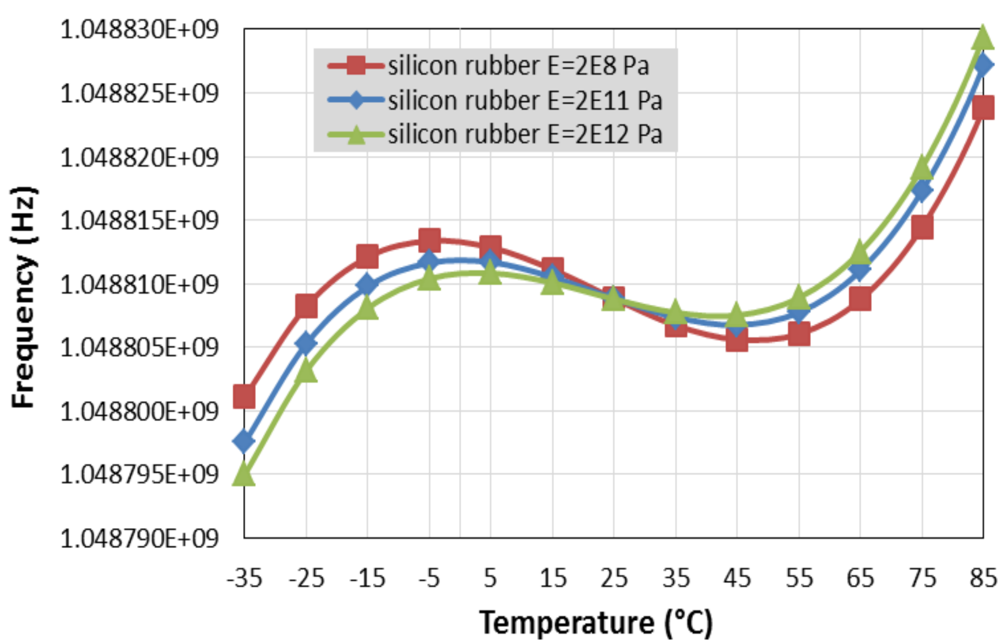

Figure 6.12: f-T characteristic of 1 GHz *AT*-cut resonator (θ = 35.25°) with different mounting stiffness. (Variation in Frequency)

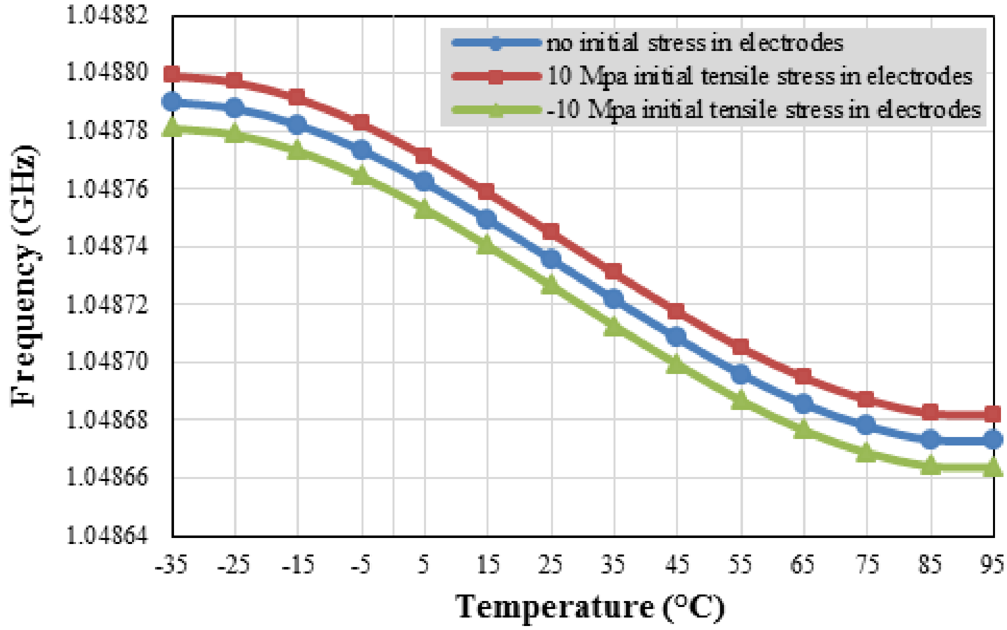

Figure 6.13: f-T curve for 1 GHz *AT*-cut resonator subjected to initial tensile and compressive stress in the electrode films.

The f-T curves for the 1 GHz *AT*-cut resonator with different electrode film metals are shown in Figures 6.14-6.16. We see in Figure 6.14 the plate with electrode mass loading yields a different f-T curve from the plate with composite layers of quartz plate and aluminum films. The composite plate with aluminum electrodes rotates the f-T curve clockwise from the f-T curve of the plate with aluminum mass loading. The f-T curve of the composite plate is more accurate since the UHF resonator is in effect a composite plate.

We see in Figure 6.15 the effect of chromium on the composite plate shows rotation of the f-T curve opposite to that of the quartz-aluminum composite plate. The quartz-chromium composite plate rotates the f-T curve counter-clockwise from the f-T curve of the plate with mass loading. This finding is in line with Shearman's study [69] of various metals that aluminum has the greatest positive shift while chromium has the greatest negative shift. Both aluminum and chromium bond aggressively to quartz. Although aluminum and chromium are chemically related, they have different mechanical properties. Aluminum has low elastic modulus and high thermal expansion coefficient while chromium has high modulus and low thermal expansion coefficients. The linear thermal expansion coefficient of aluminum is about twice of quartz and about four times of chromium. In Figure 6.16, the effect of quartz-titanium composite plate also rotates the f-T curve counter clockwise but not as much as the quartz-chromium composite plate. The small effect of the titanium electrode film shows that titanium is a good candidate as an electrode metal for quartz resonators.

Since the aluminum and chromium films have opposite effects on the f-T behavior of quartz resonators, we could use them to adjust and improve the f-T curves. For example, in Figure 6.17, we could improve the f-T curve of aluminum composite plate by adding a thin layer of chromium film that will rotate the f-T curve counter-clockwise to reduce the 1^{st} temperature coefficient of the f-T curve. The purple line is the aluminum mass loading case, the blue line is the quartz-aluminum composite plate, the green line is the quartz-chromium-aluminum composite plate, and the red line is the quartz-titanium-aluminum composite plate.

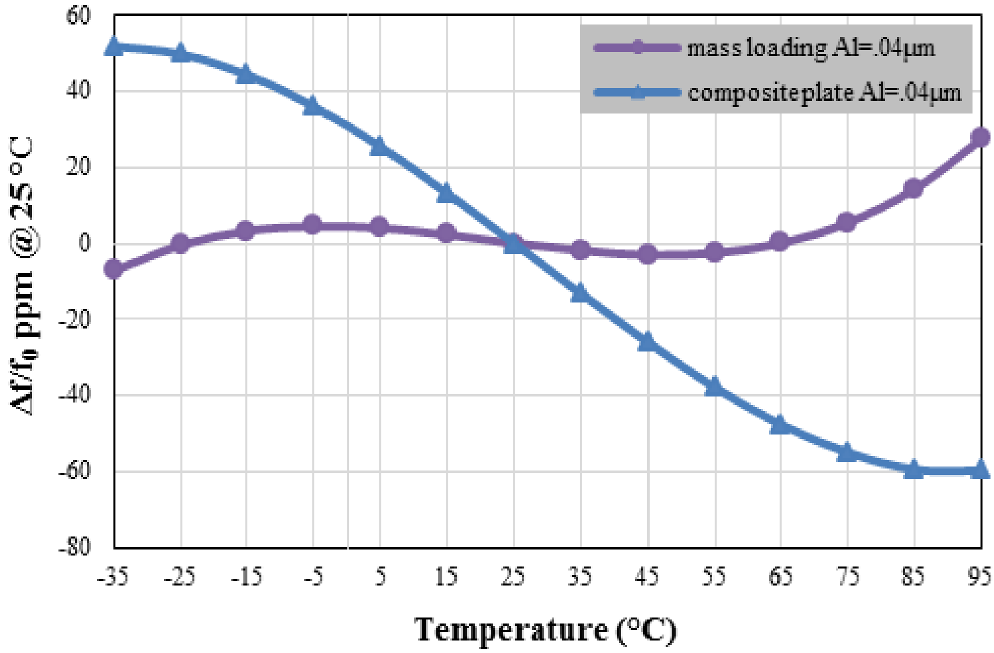

Figure 6.14: f-T curve for 1 GHz *AT*-cut resonator with aluminum electrodes.

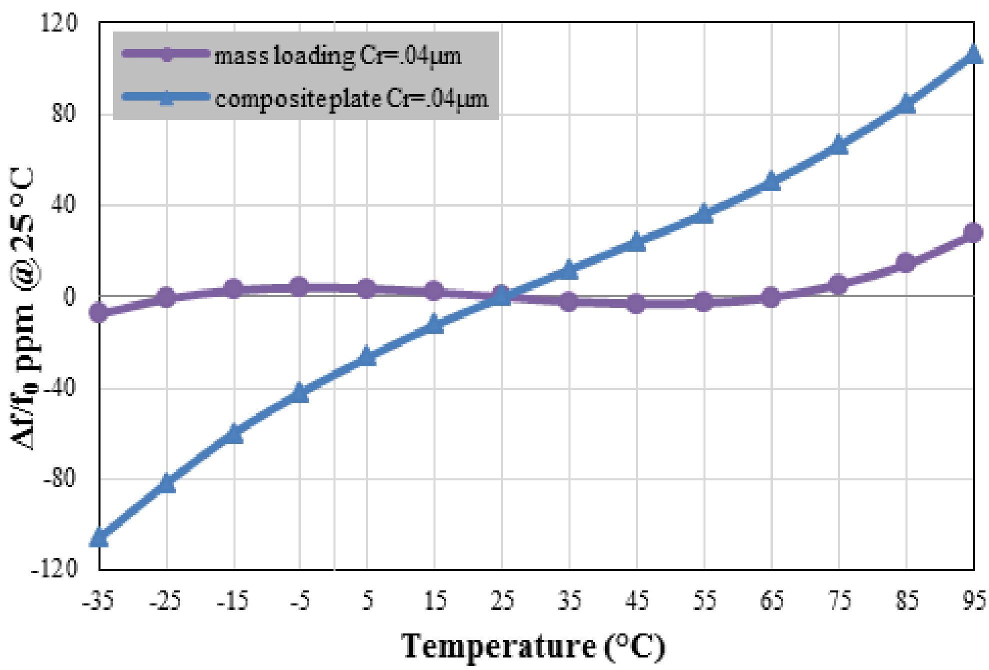

Figure 6.15: f-T curve for 1 GHz *AT*-cut resonator with chromium electrodes.

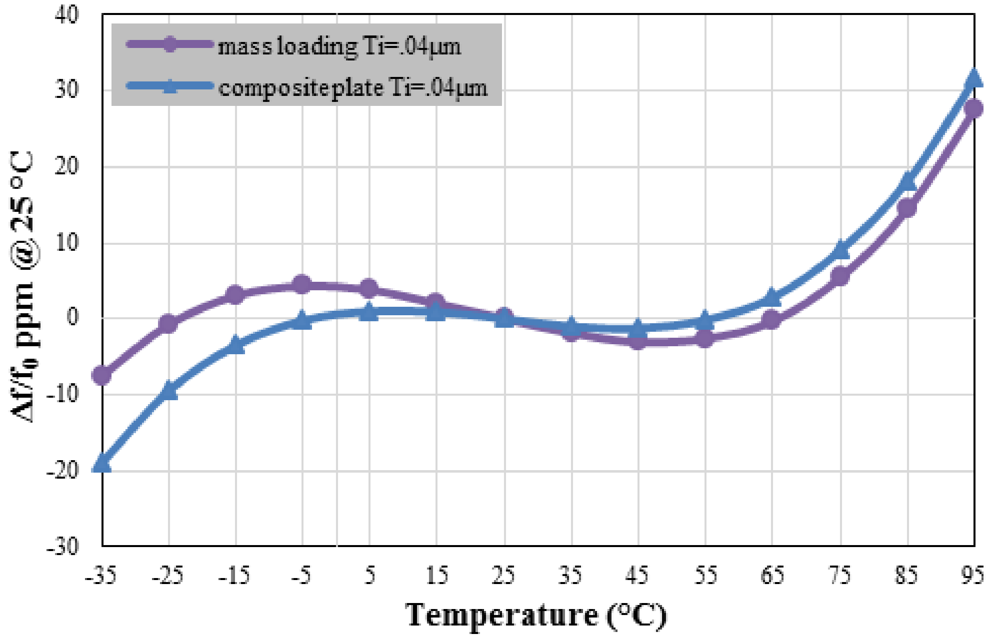

Figure 6.16: f-T curve for 1 GHz *AT*-cut resonator with titanium electrodes.

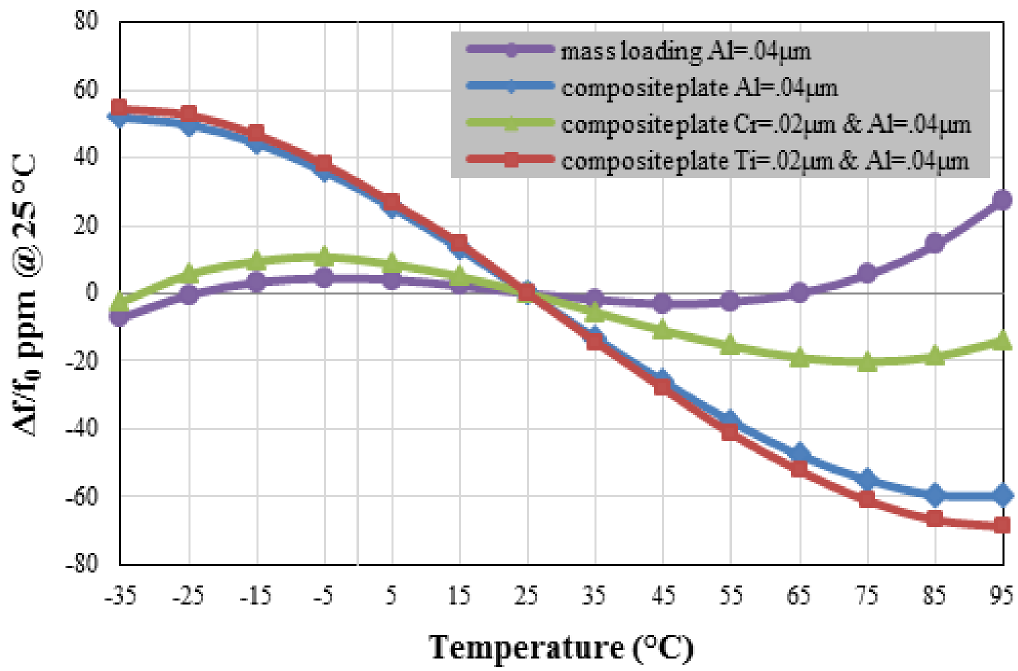

Figure 6.17: f-T curve for 1 GHz *AT*-cut resonator with different electrode metals.

6.7 Summary of Analysis

Our FEM model employing the equations for incremental vibrations superposed on thermally induced deformation was used to study the frequency-temperature behavior of composite plates with different electrode metals. (1) UHF quartz resonators must be treated as composite plates of quartz and electrode film since the ratio of electrode thickness to quartz plate thickness is significant. (2) The quartz-aluminum composite plate rotates the f-T curve clockwise while the quartz-chromium composite plate rotates the f-T curve counter-clockwise. (3) The titanium is an excellent electrode metal due to its small effect on the f-T curve. (4) The frequency-temperature behavior of quartz-aluminum composite plate can be improved by adding a thin layer of chromium film that will rotate the f-T curve counter-clockwise.

Chapter 7 Conclusions and Future Works

7.1 Conclusions

In this dissertation, we studied the nonlinear behaviors of quartz resonators using finite element method. The nonlinear behaviors that affect the stability of quartz resonators at high frequencies are:

(1) Acceleration Sensitivity

(2) Force-Frequency Effect and

(3) Frequency-Temperature Behavior.

In high frequency resonator, the effects of nonlinearities in quartz become more pronounced. Acceleration changes the resonance frequencies. The acceleration can be a form of vibration, external force or acoustic noise. The amount of frequency change depends on the magnitude and direction of acceleration. Temperature change creates thermal strains which caused the resonant frequencies to change. Factors that can affect the f vs. T characteristics of crystal include the stresses in the electrode, stains in the quart material, and stresses in the mounting structure. The conclusions of the work proposed in this thesis are summarized in the following for each chapter.

In chapter 1, we briefly presented the difference between BAW and SAW technologies as well as the applications of these devices. Literature reviews on acceleration sensitivity and temperature stability were presented. In chapter 2, piezoelectric governing equations and constitutive equations were derived using variation principle of virtual work. These equations are implemented in the succeeding chapters to study the frequency-temperature behavior and the acceleration sensitivity in quartz resonators. Next, quartz crystallography with system of notation for the orientation of crystalline plates and Butterworth Van Dyke (BVD) equivalent circuit model are introduced in chapter 3. The equivalent circuit relates the mechanical properties of the resonators to the electrical parameters C_1, L_1 and R_1 using eigenvalue analysis.

Chapter 4 presents the study of acceleration sensitivity of 1GHz resonator subjected to both in-plane and out-of-plane body forces using the newly derived incremental piezoelectric equations in Lagrangian formulation. When the crystal digonal *X*-axis is at 90^{o} to the plate *X*-axis ($\psi_1 = 90^{o}$), the in-plane acceleration sensitivity is negligible when compared to the out-of-plane acceleration sensitivity. The acceleration sensitivity is rectified for $\psi_1 = 0°$ and not rectified for $\psi_1 = 90°$. The acceleration sensitivity is predominantly due to out-of-plane body forces in the *Y*-axis direction when $\psi_1 = 90°$ and we proposed an active reduction of the acceleration sensitivity for out-of-plane vibration using pairs of edge electrodes with DC bias field to demonstrate the reduction of acceleration sensitivity.

In chapter 5, a circular plate subjected to diametrical compression forces and flexural bending of different configurations in both fundamental mode and third overtone mode to study force-frequency effects. Incremental field equations were implemented to calculate the change in the thickness shear frequency for different support configurations such as in-plane compression, cantilever bending and symmetric bending and compared with the measured results. The comparison showed a good agreement of the finite element model results with the measured results by Fletcher [38] and Mingins [26, 27]. The assumptions of linear initial stresses/strains are only adequate for in-plane compressional forces while for out-of-plane bending the nonlinear initial stresses/strains are needed. For *AT*-cut, the critical angles for frequency insensitive to compressional forces have been found when azimuth angle ψ is around 65° and 115°, and the total frequency change for a given force is proportional to overtone.

Static frequency-temperature model was used to accurately predict the f-T behavior of quartz resonator over a range of temperature in chapter 6. Lagrangian equations for small vibrational superposed on thermally induced stresses and strains were employed. FEM results were compared with the experimental measured results by Sekimoto [67] for 1 MHz rectangular *AT*-cut quartz plate. Good comparisons between the measured results and FEM numerical results were found. For UHF quartz resonator, the ratio of electrode thickness to quartz plate thickness is significant; the assumption of mass loading films is no longer valid, the quartz plate and the electrodes films must be treated as composite plate. The electrode film stresses in the composite plate can be used to improve the f-T behavior of UHF quartz resonator. The quartz-aluminum composite plate rotates the f-T curve clockwise while the quartz-chromium composite plate rotates the f-T curve counter-clockwise. The f-T behavior of quartz-aluminum composite plate can be improved by adding a thin layer of chromium film that will rotate the f-T curve counter-clockwise.

7.2 Future works

Finite element method developed for different nonlinear behaviors in quartz resonators showed good agreement with the measured results. The models developed can be used to predict new design of ultra-stable quartz resonators at high frequencies. Since the nonlinear elastic constants are the source for some of the nonlinear behaviors in quartz resonator, the fourth-order elastic constant of quartz (although not fully defined), the third-order piezoelectric constant, third-order dielectric constant and electrostrictive constants of quartz could be included in the FEM model. This will help to improve the model accuracy and extend its applications. Moreover, we should explore other types of crystal cut such as *AK*-cut, a double rotated cut with better frequency-temperature characteristics than *AT*-cut.

Bibliography

[1] R. Weigel, D. Morgan, J. Owens, A. Ballato, K.M.Lakin, K. Hashimoto and C.C.W.Ruppel, "Microwave Acoustic Material, Devices and Applications," *IEEE Transaction on Microwave Theory and Techniques*, vol. 50, pp. 738-748, March 2002.

[2] T. Kojim and H. Obara, "Two-Port Saw Resonator Using Series Connect IDTS," *IEEE Ultrasonic Symposium*, vol. 1, pp. 81-86, 1998.

[3] M. Ueda and Y. Satoh, "FBAR and SAW Technologies and Their Applications for Mobile Communications," in *Asia-Pacific Microwave Conference Workshops*, 2006.

[4] Y. Satoh, O. Ikata and T. Miyashita, "RF SAW Filters," in *International Symposium on Acoustic Devices for Future Mobile Communication Systems*, 2001.

[5] R. Aigner, "MEMS in RF Filter Applications: Thin-Film Bulk Acoustic Wave Technology," *Wiley InterScience: Sensorys Update*, vol. 12, pp. 175-210, 2003.

[6] J. Kaitila, "Review of Wave Propagation in BAW Thin Film Devices Progress and Prospects," *IEEE Ultrasonic Symposium*, pp. 120-129, 2007.

[7] K. Lakin, "Fundamental Properties of Thin Film Resonators," *IEEE 45th Annual Symposium on Frequency Control*, pp. 201-206, 1991.

[8] M. Hara, T. Yokoyama, M. Ueda and Y. Satoh, "X-Band Filters Utilizing AIN Thin Film Bulk Acoustic Resonators," *IEEE Ultrasonics Symposium*, pp. 1152-1155, 2007.

[9] T. Nishihara, T. Yokoyama, T. Miyashita and Y. Satoh, "High Performance and Miniature Thin Film Bulk Acoustic Wave Filters for 5 GHz," *IEEE Ultrasonics Symposium*, pp. 969-972, 2002.

[10] G. Fattinger, J. Kaitila, R. Aigner and W. Nessler, "Thin Film Bulk Acoustic Wave Devices for Applications at 5.2 GHz," *IEEE Ultrasonics Symposium*, pp. 174-177, 2003.

[11] G. Carlotti, F. Hickernell, H.M.Liaw, L. Palmieriri, G. Socino and E. Verona, "The Elastic Constant of Sputtered Aluminum Nitride Films," *IEEE Ultrasonics Symposium*, pp. 353-356, 1995.

[12] J. Rosenbaum, Bulk Acoustic Wave Theory and Devices, Artech House, 1988.

[13] R. Ruby, "Review and Comparsion of Bulk Acoustic Wave FBAR, SMR Technology," *IEEE Ultrasonics Symposium*, pp. 1029-1040, 2007.

[14] J. V. Tirado, Bulk Acoustic Wave Resonators and Their Application to Microwave Devices, Barcelona: Universitat Autonoma de Barcelona, 2010.

[15] F. Hicknernell, "The Piezoelectric Semiconductor and Acoustoelectronic Device Development in the Sixties," *IEEE Transactions on Ultransonics, Ferroelectrics and Frequency Control*, vol. 52, no. 5, pp. 737-745, 2005.

[16] R. Aigner, "SAW, BAW and the Future of Wireless," 6 May 2013. [Online]. Available: http://www.edn.com/design/wireless-networking/4413442/SAW--BAW-and-the-future-of-wireless.

[17] C. K. Campbell, "Applications of Surface Acoustic and Shallow Bulk Acoustic Wave Devices," *Proceedings of the IEEE*, pp. 1453-1484, 1989.

[18] V. Ferrari and R. Lucklum, "Oview of Acoustic-Wave Microsensors," in *Piezoelectric Transducers and Applications*, Berlin Heidelberg, Springer, 2008, p. 41.

[19] C. Acar and A. Shkel, MEMS Vibratory Gyroscopes Structure Approaches to Imporve Robustness, New York: Springer Verlag, 2009, pp. 4-5.

[20] A. Ballato and J. Vig, "Static and Dynamic Frequency-Temperature Behavior of Singly and Doubly Rotated Oven-Controlled Quartz Resonators," *Proceedings of the 32nd Annual Symposium on Frequency Control*, pp. 180-188, 1978.

[21] R. Bechmann, A. Ballato and T. Lukaszek, "Frequency-Temperature Behavior of Thickness Modes of Double-Rotated Quartz Plates," *Proceedings of the 15th Annual Symposium on Frequency Control*, pp. 22-48, 1961.

[22] R. Bechmann, A. Ballato and T. Lukaszek, "Higher-Order Temperature Coefficient of the Elastic Stiffness and Compliance of Alpha-Quartz," *Proceedings of The IRE*, pp. 1812-1822, 1962.

[23] B. Sinha and H. Tiersten, "First Temperature Derivatives of the Fundamental Elastic Constants of Quartz," *Journal of Applied Physics*, vol. 50, no. 4, pp. 2732-2739, 1979.

[24] R. Bechmann, A. Ballato and T. Lukaszek, "Frequency Temperature Characteristic of Quartz Resonators Derived from Temperature Behavior of the Elastic Constants," *Proceedings of the 16th Annual Symposium on Frequency Control*, pp. 77-109, 1962.

[25] V. Bottom, "Note on the Anomalous Thermal Effect in Quartz Oscillator," *Amer Mineralogist*, vol. 32, pp. 590-591, 1947.

[26] C. Mingins, L. Barcus and R. Perry, "Effect of External Forces on the Frequency of Vibrating Crystal Plates," *Proceedings of the 16th Annual Symposium on Frequency Control*, pp. 46-76, 1962.

[27] C. Mingins, L. Barcus and R. Perry, "Reactions of a Vibrating Piezoelectric Crystal Plate to Externally Applied Forces," *Proceedings of the 17th Annual Symposium on Frequency Control*, pp. 51-87, 1963.

[28] P. Lee, Y. Wang and X. Markenscoff, "High Frequency Vibrations of Crystal Plate Under Initial Stresses," *Journal Acoustic Society of America*, vol. 57, no. 1, pp. 95-105, 1975.

[29] P. Lee, Y. S. Wang and X. Markenscoff, "Elastic Waves and Vibrations in Deformed Crystal Plates," *Proceedings of the 27th Annual Symposium on Frequency Control*, pp. 1-6, 1973.

[30] D. Janiaud, L. Nissim and J. Gagnepain, "Analytical Calculation of Initial Stress Effects on Anisotropic Crystals Application to Quartz Resonator," *Proceedings of the 32nd Annual Symposium on Frequency Control*, pp. 169-179, 1978.

[31] P. Lee and K. M. Wu, "Effect of Acceleration on the Resonance Frequencies of Crystal Plates," *Proceedings of the 30th Annual Symposium on Frequency Control*, pp. 1-7, 1976.

[32] P. Lee and K. Wu, "The Influence of Support Configuration on the Acceleration Sensitivity of Quartz Resonator Plates," *Proceedings of the 31st Annual Symposium on Frequency Control*, pp. 29-34, 1977.

[33] P. Lee and K. Wu, "In-Plane Accelerations and Forces on Frequency Changes in Doubly Rotated Quartz Plates," *Journal Acoustical Society of America*, pp. 1105-1117, 1984.

[34] P. Lee and M. Tang, "Acceleration Effect on the Thickness Vibrations of Doubly Rotated Crystal Resonators," *Proceedings of the 41st Annual Symposium on Frequency Control*, pp. 277-281, 1987.

[35] P. Lee and M. Tang, "Acceleration Insensitivity of Thickness Frequencies of Doubly Rotated Quartz Crystal Disks," *Proceedings of the 42nd Annual Symposium on Frequency Control*, pp. 14-18, 1988.

[36] J. M. Ratajski, "The Force Sensitivity of AT-cut Quartz Crystals," *Proceedings of the 20th Annual Symposium on Frequency Control*, pp. 33-48, 1966.

[37] A. Ballato, "Effects of Initial Stress on Quartz Plates Vibrating in Thickness Modes," *Proceedings of the 14th Annual Symposium on Frequency Control,* pp. 89-114, 1960.

[38] E. Fletcher and A. Douglas, "A Comparsion of the Effects of Bending Moments on the Vibrations of AT and SC Cuts of Quartz," *Proceedings of the 33rd Annual Symposium on Frequency Control*, pp. 346-350, 1979.

[39] T. Lukaszek and A. Ballato, "Resonators for Severe Environments," *Proceedings of the 33rd Annual Symposium of Frequency Control*, pp. 311-321, 1979.

[40] R. Besson, J. Gagnepain, D. Janiaud and M. Valdois, "Design of a Bulk Wave Quartz Resonator Insensitive to Acceleration," *Proceedings of the 33rd Annual Symposium on Frequency Control*, pp. 37-345, 1979.

[41] J. Gagnepain and F. Walls, "Quartz Crystal Oscillators With Low Acceleration Sensitivity," *National Bureau of Standards,* pp. 77-885, 1977.

[42] J. Przyjemski, "Improvement in System Performance Using a Crystal Oscillator Compensated for Acceleration Sensitivity," *Proceedings of the 32nd Annual Symposium of Frequency Control*, pp. 426-431, 1978.

[43] D. Emmons, "Acceleration Sensitivity Compensation in High Performance Crystal Oscillators," in *10th PTTI Conference*, 1978.

[44] V. Rosati, "Suppression of Vibration Effects on Piezoelectric Crystals Resonators". United States Patent 4453141, 1984.

[45] P. Lee, N.H.Liu and A.Ballato, "Thickness Vibrations of Piezoelectric Plate with Dissipation," *IEEE Transactions UFFC*, vol. 51, pp. 52-62, January 2004.

[46] "IEEE Standard on Piezoelectricity," The Institude of Electrical and Electronics Engineers, New York, 1987.

[47] C. Desai, E. Krempl, G. Frantziskonis and H. Saadatmanesh, Constitutive Laws for Engineering Materials: Recent Advances and Industrial and Infrastructure Applications, New York: ASME, 1991, pp. 605-608.

[48] H. Tiersten, "Hamilton's Principle for Linear Piezoelectric Media," *Proceedings of IEEE*, vol. 55, no. 8, pp. 1523-1524, 1967.

[49] H.F.Tiersten, Linear Piezoelectric Plate Vibrations, New York: Plenum Press, 1969.

[50] S. P. Joshi, "Non-Linear Constitutive Relations for Piezoceramic Materials," *Smart Mater.Struct. 1*, pp. 80-83, 1992.

[51] Y. Cho and F. Matsuno, "The Relation Between the Constants of Electrostrictive Materials and Some Examples of Their Application to Piezoelectric Ceramics," *Trans. Inst. Electron. Info. & Comun. Eng.,* Vols. J75-A, pp. 875-882, 1992.

[52] R. E. Newnham, Properties of Materials, New York: Oxford University Press, 2005.

[53] J. Ransley, "COMSOL BLOG," 2 October 2014. [Online]. Available: https://www.comsol.com/blogs/piezoelectric-materials-understanding-standards/.

[54] M. Schmid, E. Benes, W. Burger and V. Kravchenko, "Motional Capacitance of Layered Piezoelectric Thickness-Mode Resonator," *IEEE Trans. Ultrasonics, Ferroelectric Frequency Control,* vol. 38, no. 3, pp. 199-206, 1991.

[55] J. R. Vig, "Introduction to Quartz Frequency Standards," U.S. Army Electronics Technology and Devices Laboratory, Fort Monmouth, 1992.

[56] R. Filler, "The Acceleration Sensitivity of Quartz Crystal Oscillators: A Review," *IEEE Transactions on Ultransonics, Ferroelectrics and Frequency Control,* vol. 35, pp. 297-305, 1988.

[57] V. Rosati and R. Filler, "Reduction of the Effect of Vibration on SC-cut Quartz Crystal Oscillators," *Proceedings of the 35th Annual Symposium on Frequency Control,* pp. 117-121, 1981.

[58] Y. Yong and M. Patel, "Application of a DC-bias to Reduce Acceleration Sensitivity in Quartz Resonators," *International Journal of Applied Electromagnetics and Mechanics,* vol. 22, pp. 69-82, 2005.

[59] M. Valdois, J. Besson and J. Gagnepain, "Influence of Enviroment Conditions on a Quartz Resonator," *Proceedings of the 28th Annual Symposium on Frequency Control,* pp. 19-32, 1978.

[60] J. Yang, Analysis of Piezoelectric Devices, Singapore: World Scientific, 2006.

[61] J. Ratajski, "Force Frequency Coefficient of Singly Rotated Vibrating Quartz Crystal," *IBM Journal of Research and Development,* vol. 12, no. 1, pp. 92-99, 1968.

[62] J. Kosinski, "Designing for Low Acceleration Sensitivity," *IEEE Transactions on Ultrasonics, Ferroelectrics and Frequency Control,* vol. 40, no. 5, pp. 532-537, 1993.

[63] P. Lee and M. Tang, "Thickness Vibrations of Doubly Rotated Crystal Plates Under Initial Deformations," *IEEE Transactions on Ultrasonics, Ferroelectrics, and Frequency Control,* vol. 34, no. 6, pp. 659-666, 1987.

[64] P. Lee, Y. Wang and X. Markenscoff, "Nonlinear Effect of Initial Bending on the Vibrations of Crystal Plates," *Journal Acoustic Society of America,* vol. 59, no. 1, pp. 90-96, 1976.

[65] E. ErNisse, "Quartz Resonator Frequency Shifts Arising from Electrode Stress," *Proceedings of the 29th Annual Symposium on Frequency Control,* pp. 1-4, 1975.

[66] J. Laconte, D. Flandre and J.-P. Raskin, "Micromachined Thin-Film Sensor for SOI-CMOS Co-Integration," Netherlands, Springer, 2006, pp. 53-56.

[67] H. Sekimoto, S. Goka, A. Ishizaki and Y. Watanabe, "Frequency-Temperature Behavior of Spurious Vibrations of Rectangular AT-cut Quartz Plate," *IEEE Transactions on Ultrasonics, Ferroelectrics and Frequency Control,* vol. 45, no. 4, pp. 1017-1021, 1998.

[68] Y. Yong, M. Patel and M. Tanaka, "Effect of Thermal Stresses on the Frequency-Temperature Behavior of Piezoelectric Resonators," *Journal of Thermal Stresses,* vol. 30, pp. 639-661, 2007.

[69] J. Sherman, "Temperature Coefficient of the Frequency Shift Arising from Electrode Film Stress," *IEEE Transaction on Sonics and Ultrasonics,* vol. 30, no. 2, pp. 104-110, 1983.

[70] R. Bechmann, "Elastic and Piezoelectric Constants of Alpha-Quartz," *Physical Review,* vol. 110, no. 5, pp. 1060-1061, 1958.

[71] R. Thurston, H. McSkimin and P. Andreatch, "Third Order Elastic Coefficients of Quartz," *Journal of Applied Physics,* vol. 37, no. 1, pp. 267-275, 1966.

[72] P. Lee and Y. Yong, "Frequency-Temperature Behavior of Thickness Vibrations of Doubly Rotated Quartz Plates Affected by Plate Dimensions and Orientations," *Journal of Applied Physics,* pp. 2327-2342, 1986.

[73] Y. Yong and W. Wei, "Lagrangian Temperature Coefficients of The Piezoelectric Stress Constants and Dielectric Permittivity of Quartz," *IEEE International Frequency Control Symposium,* pp. 364-372, 2000.

[74] J. Lamb and J. Richter, "Anisotropic Acoustic Attenuation with New Measurements for Quartz at Room Temperatures," *Proceedings of the Royal Society of London Series A, Mathematical and Physical,* vol. 293, pp. 479-492, 1966.

[75] J. Kosinski, J. Gualtieri and A. Ballato, "Thermal Expansion of Alpha Quartz," *Proceedings of the 45th Annual Symposium on Frequency Control,* pp. 22-28, 1991.

[76] C. Hruska and P. Ng, "Material Nonlinearities in Quartz Determined by the Transit-Time Method Using Direct Current Field Interactions," *Journal Acoustic Society of America,* vol. 93, pp. 1426-1430, 1993.

[77] J. Neighbours and G. Alers, "Elastic Constants of Silver and Gold," *Physical Review,* vol. 111, no. 3, pp. 707-712, 1958.

[78] Y. Chang and L. Himmel, "Temperature Dependence of the Elastic Constant of Cu, Ag and Au About Room Temperature," *Journal of Applied Physics,* vol. 37, no. 9, pp. 3567-3572, 1966.

[79] Y. Hiki and A. Granato, "Anharmonicity in Noble Metal Higher Order Elastic Constants," *Physical Review,* vol. 144, no. 2, pp. 411-419, 1966.

[80] F. Nix and D. MacNair, "The Thermal Expansion of Pure Metals: Copper, Aluminum, Nickel and Iron," *Physical Review,* vol. 60, pp. 597-605, 1941.

[81] International Critical Tables of Numberical Data Physics, Chemistry and Technology, New York: McGraw-Hill Book Company, 1929.

[82] R. Hearmon, "Temperature Dependence of the Elastic Constants of Aluminum," *Solid State Communications,* vol. 37, pp. 915-918, 1981.

[83] J. Thomas, "Third Order Elastic Constants of Aluminum," *Physicsl Review,* vol. 175, no. 3, pp. 955-962, 1968.

[84] D. Bolef and J. Klerk, "Anomalies in the Elastic Constants and Thermal Expansion of Chromium Single Crystals," *Physical Review,* vol. 129, no. 3, pp. 1063-1067, 1963.

[85] S. Palmer and E. Lee, "The Elastic Constants of Chromium," *Philosophical Magazine,* vol. 24, no. 188, pp. 311-318, 1971.

[86] S. Mathur and Y. Sharma, "Second and Third Order Elastic Constants of Cr, Mo, and W," *Physica Status Solidi B,* vol. 41, no. 1, pp. K51-5, 1970.

[87] E. Fisher and C. Renken, "Single-Crystal Elastic Moduli and the hcp to bcc Transformation in Ti, Zr, and Hf," *Physical Review,* vol. 135, pp. 482-494, 1964.

[88] R. Rao and C. Menon, "Lattice Dynamics, Third-Order Elastic Constants and Thermal Expansion of Titanium," *Physical Review* , vol. 7, no. 2, pp. 644-650, 1973.

[89] P. Hidnert, "Thermal Expansion of Titanium," *Journal of Research of the National Bureau of Standards,* vol. 30, pp. 101-105, 1943.

Appendix A. Constitutive Equations

A1. Alternative Forms of Linear Piezoelectric Constitutive Equations

	Stress $\left[\frac{\mathrm{N}}{\mathrm{m}^2}\right]$	*Strain* $\left[\frac{\mathrm{m}}{\mathrm{m}}\right]$	
"Charge" $\left[\frac{\mathrm{C}}{\mathrm{m}^2}\right]$	$\boldsymbol{T}, \boldsymbol{D} \xleftarrow{\boldsymbol{e}} (\boldsymbol{S}, \boldsymbol{E})$	$\boldsymbol{S}, \boldsymbol{D} \xleftarrow{\boldsymbol{d}} (\boldsymbol{T}, \boldsymbol{E})$	("voltage")
"Voltage" $\left[\frac{\mathrm{V}}{\mathrm{m}}\right]$	$\boldsymbol{T}, \boldsymbol{E} \xleftarrow{\boldsymbol{h}} (\boldsymbol{S}, \boldsymbol{D})$	$\boldsymbol{S}, \boldsymbol{E} \xleftarrow{\boldsymbol{g}} (\boldsymbol{T}, \boldsymbol{D})$	("charge")
	(strain)	(stress)	

Stress-Charge form

$$T_{ij} = C^{E}_{ijkl} S_{kl} - e_{kij} E_k$$

$$D_i = e_{ikl} S_{kl} + \varepsilon^{S}_{ik} E_k$$

Stress-Voltage form

$$T_{ij} = C^{D}_{ijkl} S_{kl} - h_{kij} D_k$$

$$E_i = -h_{ikl} S_{kl} + \beta^{S}_{ik} D_k$$

Strain-Charge form

$$S_{ij} = s^{E}_{ijkl} T_{kl} + d_{kij} E_k$$

$$D_i = d_{ikl} T_{kl} + \varepsilon^{T}_{ik} E_k$$

Strain-Voltage form

$$S_{ij} = s^{D}_{ijkl} T_{kl} + g_{kij} D_k$$

$$E_i = -g_{ikl} T_{kl} + \beta^{T}_{ik} D_k$$

A2. Alternative Forms of Nonlinear Piezoelectric Constitutive Equations

Stress-Charge form

$$T_{\boldsymbol{ij}} = C^{E}_{ijkl}S_{kl} - e_{kij}E_k + \frac{1}{2}C^{E}_{ijklmn}S_{kl}S_{mn} - \frac{1}{2}l_{klij}E_kE_l - e_{mijkl}E_mS_{kl}$$
$$D_i = e_{ikl}S_{kl} + \varepsilon^{S}_{ik}E_k + \frac{1}{2}e_{ijklm}S_{jk}S_{lm} + \frac{1}{2}\varepsilon^{S}_{ijk}E_jE_k + l_{ijkl}E_jS_{kl}$$

Stress-Voltage form

$$T_{\boldsymbol{ij}} = C^{D}_{ijkl}S_{kl} - h_{kij}D_k + \frac{1}{2}C^{D}_{ijklmn}S_{kl}S_{mn} - \frac{1}{2}\eta_{klij}D_kD_l - h_{mijkl}D_mS_{kl}$$
$$E_i = -h_{ikl}S_{kl} + \beta^{S}_{ik}D_k - \frac{1}{2}h_{ijklm}S_{jk}S_{lm} + \frac{1}{2}\beta^{S}_{ijk}D_jD_k - \eta_{ijkl}D_jS_{kl}$$

Strain-Charge form

$$S_{\boldsymbol{ij}} = S^{E}_{ijkl}T_{kl} + d_{kij}E_k + \frac{1}{2}S^{E}_{ijklmn}T_{kl}T_{mn} + \frac{1}{2}\gamma_{klij}E_kE_l + d_{mijkl}E_mT_{kl}$$
$$D_i = d_{ikl}T_{kl} + \varepsilon^{T}_{ik}E_k + \frac{1}{2}d_{ijklm}T_{jk}T_{lm} + \frac{1}{2}\varepsilon^{T}_{ijk}E_jE_k + \gamma_{ijkl}E_jT_{kl}$$

Strain-Voltage form

$$S_{\boldsymbol{ij}} = S^{D}_{ijkl}T_{kl} + g_{kij}D_k + \frac{1}{2}S^{D}_{ijklmn}T_{kl}T_{mn} + \frac{1}{2}\chi_{klij}D_kD_l + g_{mijkl}D_mT_{kl}$$

$$E_i = -g_{ikl}T_{kl} + \beta^{T}_{ik}D_k - \frac{1}{2}g_{ijklm}T_{jk}T_{lm} + \frac{1}{2}\beta^{T}_{ijk}D_jD_k - \chi_{ijkl}D_jT_{kl}$$

Appendix B. Quartz Material Properties

The mass density of Quartz is 2649 $^{kg}/_{m^3}$.

B1. Y-Cut Quartz

Y-cut quartz is a trigonal crystal with x_3 as the trigonal axis and x_1 as digonal axis. The thickness coordinate of a Y-cut quart plate is x_2. Values of material constants for left-handed Y-cut quartz (IRE 1949 standard) have been determined by R. Bechmann [70], R. Thurston, H. McSkimin and P. Andreatch [71], Y. Yong and P. Lee [72] [73], J. Lamb and J. Richter [74], J. Kosinski, J. Gualtieri, and A. Ballato [75], and C.K. Hruska and P. Ng [76].

Second-order elastic constants: (10^{10} N/m^2)

C_{pq}						
p \ q	**1**	**2**	**3**	**4**	**5**	**6**
1	8.674	0.698	1.191	-1.791	0	0
2	0.698	8.674	1.191	1.791	0	0
3	1.191	1.191	10.72	0	0	0
4	-1.791	1.791	0	5.794	0	0
5	0	0	0	0	5.794	-1.791
6	0	0	0	0	-1.791	3.998

Viscosity constants: (10^{-3} N-sec/m^2)

n_{pq}						
p \ q	**1**	**2**	**3**	**4**	**5**	**6**
1	1.37	0.73	0.71	0.01	0	0
2	0.73	1.37	0.71	-0.01	0	0
3	0.71	0.71	0.96	0	0	0
4	0.01	-0.01	0	0.36	0	0
5	0	0	0	0	0.36	0.01
6	0	0	0	0	0.01	0.32

First temperature derivatives of elastic constants: (10^6 N/(m^2* ℃))

$C^{(1)}_{pq}$						
p \ q	**1**	**2**	**3**	**4**	**5**	**6**
1	1.5976	-8.5518	-2.1983	0.91675	0	0
2	-8.5518	1.5976	-2.1983	-0.91675	0	0
3	-2.1983	-2.1983	-6.5255	0	0	0
4	0.91675	-0.91675	0	-5.378	0	0
5	0	0	0	0	-5.378	0.91675
6	0	0	0	0	0.91675	5.0747

Effective second temperature derivatives of elastic constants: (10^3 N/(m^2* (℃)^2))

$C^{(2)}_{pq}$						
p \ q	**1**	**2**	**3**	**4**	**5**	**6**
1	-12.989	-35.121	-18.806	4.2849	0	0
2	-35.121	-12.989	-18.806	-4.2849	0	0
3	-18.806	-18.806	-20.835	0	0	0
4	4.2849	-4.2849	0	-26.505	0	0
5	0	0	0	0	-26.505	4.2849
6	0	0	0	0	4.2849	11.066

Effective third temperature derivatives of elastic constants: (N/(m^2*(℃)^3))

$C^{(3)}_{pq}$						
p \ q	**1**	**2**	**3**	**4**	**5**	**6**
1	-38.145	73.503	-8.9302	85.773	0	0
2	73.503	-38.145	-8.9302	-85.773	0	0
3	-8.9302	-8.9302	46.255	0	0	0
4	85.773	-85.773	0	-20.468	0	0
5	0	0	0	0	-20.468	85.773
6	0	0	0	0	85.773	-55.824

Third-order elastic constants: (10^{10} N/m^2)

p =1	C_{pqr}					
q \ r	**1**	**2**	**3**	**4**	**5**	**6**
1	-21	-34.5	1.2	-16.3	0	0
2	-34.5	-22.3	-29.4	-1.5	0	0
3	1.2	-29.4	-31.2	0.2	0	0
4	-16.3	-1.5	0.2	-13.4	0	0
5	0	0	0	0	-20	-10.4
6	0	0	0	0	-10.4	-5.775

p =2			C_{pqr}			
q \ r	**1**	**2**	**3**	**4**	**5**	**6**
1	-34.5	-22.3	-29.4	-1.5	0	0
2	-22.3	-33.2	1.2	19.3	0	0
3	-29.4	1.2	-31.2	-0.2	0	0
4	-1.5	19.3	-0.2	-20	0	0
5	0	0	0	0	-13.4	-7.4
6	0	0	0	0	-7.4	6.425

p =3			C_{pqr}			
q \ r	**1**	**2**	**3**	**4**	**5**	**6**
1	1.2	-29.4	-31.2	0.2	0	0
2	-29.4	1.2	-31.2	-0.2	0	0
3	-31.2	-31.2	-81.5	0	0	0
4	0.2	-0.2	0	-11	0	0
5	0	0	0	0	-11	0.2
6	0	0	0	0	0.2	15.3

p =4			C_{pqr}			
q \ r	**1**	**2**	**3**	**4**	**5**	**6**
1	-16.3	-1.5	0.2	-13.4	0	0
2	-1.5	19.3	-0.2	-20	0	0
3	0.2	-0.2	0	-11	0	0
4	-13.4	-20	-11	-27.6	0	0
5	0	0	0	0	27.6	-3.3
6	0	0	0	0	-3.3	-1.5

p =5			C_{pqr}			
q \ r	**1**	**2**	**3**	**4**	**5**	**6**
1	0	0	0	0	-20	-10.4
2	0	0	0	0	-13.4	-7.4
3	0	0	0	0	-11	0.2
4	0	0	0	0	27.6	-3.3
5	-20	-13.4	-11	27.6	0	0
6	-10.4	-7.4	0.2	-3.3	0	0

p =6	C_{pqr}					
q \ r	1	2	3	4	5	6
1	0	0	0	0	-10.4	-5.775
2	0	0	0	0	-7.4	6.425
3	0	0	0	0	0.2	15.3
4	0	0	0	0	-3.3	-1.5
5	-10.4	-7.4	0.2	-3.3	0	0
6	-5.775	6.425	15.3	-1.5	0	0

Piezoelectric constants: (10^{-2} C/m^2)

e_{ij}						
i \ j	1	2	3	4	5	6
1	17.1	-17.1	0	-4.067	0	0
2	0	0	0	0	4.067	-17.1
3	0	0	0	0	0	0

First temperature derivatives of piezoelectric constants: (10^{-6} C/(m^2* ℃))

$e^{(1)}_{ij}$						
i \ j	1	2	3	4	5	6
1	-1.37002	1.37002	0	3.12403	0	0
2	0	0	0	0	-3.12403	1.37002
3	0	0	0	0	0	0

Second temperature derivatives of piezoelectric constants: (10^{-10} C/(m^2*(℃)^2))

$e^{(2)}_{ij}$						
i \ j	1	2	3	4	5	6
1	-7.48887	7.48887	0	26.0005	0	0
2	0	0	0	0	-26.0005	7.48887
3	0	0	0	0	0	0

Third temperature derivatives of piezoelectric constants: (10^{-12} C/(m^2*(℃)^3))

$e^{(3)}_{ij}$						
i \ j	1	2	3	4	5	6
1	1.955179	-1.955179	0	-4.69238	0	0
2	0	0	0	0	4.69238	-1.955179
3	0	0	0	0	0	0

Dielectric permittivity: (10^{-12} C/(V*m))

ε_{ip}			
i \ p	**1**	**2**	**3**
1	39.215	0	0
2	0	39.215	0
3	0	0	41.038

First temperature derivatives of dielectric permittivity: (10^{-15} C/(V*m* ℃))

$\varepsilon^{(1)}_{ip}$			
i \ p	**1**	**2**	**3**
1	`1.5902	0	0
2	0	1.5902	0
3	0	0	5.46123

Second temperature derivatives of dielectric permittivity: (10^{-18} C/(V*m*(℃)^2))

$\varepsilon^{(2)}_{ip}$			
i \ p	**1**	**2**	**3**
1	5.37723	0	0
2	0	5.37723	0
3	0	0	0.1894809

Third temperature derivatives of dielectric permittivity: (10^{-21} C/(V*m*(℃)^3))

$\varepsilon^{(3)}_{ip}$			
i \ p	**1**	**2**	**3**
1	5.105736	0	0
2	0	5.105736	0
3	0	0	-9.230945

First-order thermal expansion coefficients: (10^{-6} 1/ ℃)

$\alpha^{(1)}_{ij}$			
i \ j	**1**	**2**	**3**
1	13.71	0	0
2	0	13.71	0
3	0	0	7.48

Second-order thermal expansion coefficients: (10^{-9} 1/(℃)^2)

$\alpha^{(2)}_{ij}$			
i \ j	**1**	**2**	**3**
1	6.5	0	0
2	0	6.5	0
3	0	0	2.9

Third-order thermal expansion coefficients: (10^{-12} 1/(℃)^3)

$\alpha^{(3)}_{ij}$			
i \ j	**1**	**2**	**3**
1	-1.9	0	0
2	0	-1.9	0
3	0	0	-1.5

Electrostrictive constants: (10^{-11} C/(V*m)) (IEEE 1978 Standard right-handed quartz)

l_{pq}						
p \ q	**1**	**2**	**3**	**4**	**5**	**6**
1	4.27657	-7.3755	12.6084	-5.2151	0	0
2	-7.3755	4.27657	12.6084	5.2151	0	0
3	2.05417	2.05417	-2.9573	0	0	0
4	-1.275	1.275	0	-0.65521	0	0
5	0	0	0	0	-0.65521	-1.275
6	0	0	0	0	-5.2151	5.82606

Third-order piezoelectric constants: (C/m^2) (IEEE 1978 Standard right-handed quartz)

p =1	e_{pqr}					
q \ r	**1**	**2**	**3**	**4**	**5**	**6**
1	-2.14	0.51	0.54	-0.24	0	0
2	0.51	1.12	-0.54	-0.76	0	0
3	0.54	-0.54	0	-1.63	0	0
4	-0.24	-0.76	-1.63	-0.09	0	0
5	0	0	0	0	0.09	-0.26
6	0	0	0	0	-0.26	0.51

***p* =2**	***e$_{pqr}$***					
q* \ *r	**1**	**2**	**3**	**4**	**5**	**6**
1	0	0	0	0	0.76	0.305
2	0	0	0	0	0.24	1.325
3	0	0	0	0	1.63	-0.54
4	0	0	0	0	-0.09	0.26
5	0.76	0.24	1.63	-0.09	0	0
6	0.305	1.325	-0.54	0.26	0	0

***p* =3**	***e$_{pqr}$***					
q* \ *r	**1**	**2**	**3**	**4**	**5**	**6**
1	0	0	0	0	0.89	0
2	0	0	0	0	-0.89	0
3	0	0	0	0	0	0
4	0	0	0	0	0	-0.89
5	0.89	-0.89	0	0	0	0
6	0	0	0	-0.89	0	0

Third-order dielectric permittivity: $\varepsilon_{111}^{S} = 3.71e^{-20}(\frac{F}{V})$ **(IEEE 1978 Standard right-handed quartz)**

B2. *AT*-Cut Quartz

AT-cut of quartz is obtained by rotating *Y*-cut of quartz (YX*l*) 35.25˚. (IRE 1949 standard)

Second-order elastic constants: (10^{10} N/m^2)

C_{pq}						
p \ q	1	2	3	4	5	6
1	8.674	-0.826054	2.715054	-0.365487	0	0
2	-0.826054	12.97663	-0.741847	0.570042	0	0
3	2.715054	-0.741847	10.28306	0.992128	0	0
4	-0.365487	0.570042	0.992128	3.861153	0	0
5	0	0	0	0	6.880699	0.253357
6	0	0	0	0	0.253357	2.901301

Viscosity constants: (10^{-3} N-sec/m^2)

n_{pq}						
p \ q	1	2	3	4	5	6
1	1.37	0.732764	0.707235	0.006088	0	0
2	0.732764	1.338593	0.595410	-0.052711	0	0
3	0.707235	0.595410	1.220585	-0.143868	0	0
4	0.006088	-0.052711	-0.143868	0.245410	0	0
5	0	0	0	0	0.337249	0.022190
6	0	0	0	0	0.022190	0.342750

First temperature derivatives of elastic constants: (10^6 N/(m^2* ℃))

$C^{(1)}_{pq}$						
p \ q	1	2	3	4	5	6
1	1.5976	-5.571304	-5.178796	3.300554	0	0
2	-5.571304	-6.921529	2.750886	-3.361525	0	0
3	-5.178796	2.750886	-7.904742	-0.773078	0	0
4	3.300554	-3.361525	-0.773078	-0.428814	0	0
5	0	0	0	0	-2.760408	-4.620557
6	0	0	0	0	-4.620557	2.457108

Effective second temperature derivatives of elastic constants: (10^3 N/(m^2* (℃)^2))

$C^{(2)}_{pq}$						
p \ q	**1**	**2**	**3**	**4**	**5**	**6**
1	-12.989	-25.6474	-28.2796	9.119927	0	0
2	-25.6474	-45.38299	6.936393	-9.537211	0	0
3	-28.2796	6.936393	-39.92379	4.4089	0	0
4	9.119927	-9.537211	4.4089	-0.763607	0	0
5	0	0	0	0	-18.02935	-16.27766
6	0	0	0	0	-16.27766	2.590353

Effective third temperature derivatives of elastic constants: (N/(m^2 *(℃)^3))

$C^{(3)}_{pq}$						
p \ q	**1**	**2**	**3**	**4**	**5**	**6**
1	-38.145	126.898	-62.32517	-10.22086	0	0
2	126.898	-141.8306	42.01561	30.41957	0	0
3	-62.32517	42.01561	48.04903	-19.27172	0	0
4	-10.22086	30.41957	-19.27172	30.47781	0	0
5	0	0	0	0	-113.0982	45.29563
6	0	0	0	0	45.29563	36.80615

Third-order elastic constants: (10^{10} N/m^2)

p =1	C_{pqr}					
q \ r	**1**	**2**	**3**	**4**	**5**	**6**
1	-21	-37.97351	4.673509	11.3851	0	0
2	-37.97351	-40.10915	-15.78084	-6.287149	0	0
3	4.673509	-15.78084	-40.62917	1.658446	0	0
4	11.3851	-6.287149	1.658446	0.219159	0	0
5	0	0	0	0	-5.45823	-10.17613
6	0	0	0	0	-10.17613	-20.31677

p =2	C_{pqr}					
q \ r	**1**	**2**	**3**	**4**	**5**	**6**
1	-37.97351	-40.10915	-15.78084	-6.287149	0	0
2	-40.10915	-63.66979	19.94753	-25.98164	0	0
3	-15.78084	19.94753	-47.29024	-0.472669	0	0
4	-6.287149	-25.98164	-0.472669	-13.29065	0	0
5	0	0	0	0	19.12278	-0.095247
6	0	0	0	0	-0.095247	2.260826

p =3	C_{pqr}					
q \ r	1	2	3	4	5	6
1	4.673509	-15.78084	-40.62917	1.658446	0	0
2	-15.78084	19.94753	-47.29024	-0.472669	0	0
3	-40.62917	-47.29024	-59.00208	-4.799653	0	0
4	1.658446	-0.472669	-4.799653	-15.05206	0	0
5	0	0	0	0	-21.37168	-24.04783
6	0	0	0	0	-24.04783	-2.686924

p =4	C_{pqr}					
q \ *r*	1	2	3	4	5	6
1	11.3851	-6.287149	1.658446	0.219159	0	0
2	-6.287149	-25.98164	-0.472669	-13.29065	0	0
3	1.658446	-0.472669	-4.799653	-15.05206	0	0
4	0.219159	-13.29065	-15.05206	9.893701	0	0
5	0	0	0	0	5.786958	3.967928
6	0	0	0	0	3.967928	8.239542

p =5	C_{pqr}					
q \ r	1	2	3	4	5	6
1	0	0	0	0	-5.45823	-10.17613
2	0	0	0	0	19.12278	-0.095247
3	0	0	0	0	-21.37168	-24.04783
4	0	0	0	0	5.786958	3.967928
5	-5.45823	19.12278	-21.37168	5.786958	0	0
6	-10.17613	-0.095247	-24.04783	3.967928	0	0

p =6	C_{pqr}					
q \ r	1	2	3	4	5	6
1	0	0	0	0	-10.17613	-20.31677
2	0	0	0	0	-0.095247	2.260826
3	0	0	0	0	-24.04783	-2.686924
4	0	0	0	0	3.967928	8.239542
5	-10.17613	-0.095247	-24.04783	3.967928	0	0
6	-20.31677	2.260826	-2.686924	8.239542	0	0

Piezoelectric constants: (10^{-2} C/m^2)

e_{ij}						
i \ j	**1**	**2**	**3**	**4**	**5**	**6**
1	17.1	-15.23777	-1.862228	6.701992	0	0
2	0	0	0	0	10.77188	-9.487187
3	0	0	0	0	-7.612813	6.704881

First temperature derivatives of piezoelectric constants: (10^{-6} C/(m^2* °C))

$e^{(1)}_{ij}$						
i \ j	**1**	**2**	**3**	**4**	**5**	**6**
1	-1.37002	3.858511	-2.488491	0.397103	0	0
2	0	0	0	0	-2.729145	-0.558749
3	0	0	0	0	1.928769	0.394884

Second temperature derivatives of piezoelectric constants: (10^{-10} C/(m^2*(°C)^2))

$e^{(2)}_{ij}$						
i \ j	**1**	**2**	**3**	**4**	**5**	**6**
1	-7.48887	29.5035	-22.01463	5.149485	0	0
2	0	0	0	0	-20.86948	-7.260222
3	0	0	0	0	14.749	5.131018

Third temperature derivatives of piezoelectric constants: (10^{-12} C/(m^2*(°C)^3))

$e^{(3)}_{ij}$						
i \ j	**1**	**2**	**3**	**4**	**5**	**6**
1	1.955179	-5.727148	3.771969	-0.644832	0	0
2	0	0	0	0	4.050881	0.9177
3	0	0	0	0	-2.862879	-0.641499

Dielectric permittivity: (10^{-12} C/(V*m))

ε_{ip}			
i \ p	**1**	**2**	**3**
1	39.215003	0	0
2	0	39.822232	0.859217
3	0	0.859217	40.430762

First temperature derivatives of dielectric permittivity: (10^{-15} C/(V*m* ℃))

$\varepsilon^{(1)}_{ip}$			
i \ p	**1**	**2**	**3**
1	1.590199	0	0
2	0	2.879627	1.824496
3	0	1.824496	4.171802

Second temperature derivatives of dielectric permittivity: (10^{-18} C/(V*m*(℃)^2))

$\varepsilon^{(2)}_{ip}$			
i \ p	**1**	**2**	**3**
1	5.377229	0	0
2	0	3.649208	-2.445093
3	0	-2.445093	1.917502

Third temperature derivatives of dielectric permittivity: (10^{-21} C/(V*m*(℃)^3))

$\varepsilon^{(3)}_{ip}$			
i \ p	**1**	**2**	**3**
1	5.105736	0	0
2	0	0.330236	-6.757175
3	0	-6.757175	-4.455445

First-order thermal expansion coefficients: (10^{-6} 1/ ℃)

$\alpha^{(1)}_{ij}$			
i \ j	**1**	**2**	**3**
1	13.71	0	0
2	0	11.63481	-2.936328
3	0	-2.936328	9.555192

Second-order thermal expansion coefficients: (10^{-9} 1/(℃)^2)

$\alpha^{(2)}_{ij}$			
i \ j	**1**	**2**	**3**
1	6.5	0	0
2	0	5.300852	-1.696755
3	0	-1.696755	4.099148

Third-order thermal expansion coefficients: (10^{-12} 1/(℃)^3)

$\alpha^{(3)}_{ij}$			
i \ *j*	**1**	**2**	**3**
1	-1.9	0	0
2	0	-1.766761	0.188528
3	0	0.188528	-1.633239

B3. *BT*-Cut Quartz

BT-cut of quartz is obtained by rotating *Y*-cut of quartz (YX*l*) -49˚. (IRE 1949 standard)

Second-order elastic constants: (10^{10} N/m^2)

C_{pq}						
p \ *q*	**1**	**2**	**3**	**4**	**5**	**6**
1	8.674	2.752376	-0.863376	0.005157	0	0
2	2.752376	9.823789	-0.566985	-1.279583	0	0
3	-0.863376	-0.566985	13.08618	0.017279	0	0
4	0.005157	-1.279583	0.017279	4.036015	0	0
5	0	0	0	0	2.991757	-0.644953
6	0	0	0	0	-0.644953	6.790243

Viscosity constants: (10^{-3} N-sec/m^2)

n_{pq}						
p \ *q*	**1**	**2**	**3**	**4**	**5**	**6**
1	1.37	0.708705	0.731294	0.00851	0	0
2	0.708705	1.274928	0.581444	0.125265	0	0
3	0.731294	0.581444	1.312183	0.079131	0	0
4	0.00851	0.125265	0.079131	0.231444	0	0
5	0	0	0	0	0.347119	-0.02119
6	0	0	0	0	-0.02119	0.33288

First temperature derivatives of elastic constants: (10^6 N/(m^2* ℃))

$C^{(1)}_{pq}$						
p \ *q*	**1**	**2**	**3**	**4**	**5**	**6**
1	1.5976	-5.84076	-4.90934	-3.273421	0	0
2	-5.84076	-7.391306	3.071626	1.79254	0	0
3	-4.90934	3.071626	-8.076445	2.35707	0	0
4	-3.273421	1.79254	2.35707	-0.108074	0	0
5	0	0	0	0	1.483546	5.047901
6	0	0	0	0	5.047901	-1.786846

Effective second temperature derivatives of elastic constants: (10^3 N/(m^2 (℃)^2))

$C^{(2)}_{pq}$						
p \ q	1	2	3	4	5	6
1	-12.989	-30.0714	-23.8556	-8.674455	0	0
2	-30.0714	-40.72559	8.704817	0.516639	0	0
3	-23.8556	8.704817	-48.12004	3.964525	0	0
4	-8.674455	0.516639	3.964525	1.005817	0	0
5	0	0	0	0	-0.861864	18.00634
6	0	0	0	0	18.00634	-14.57714

Effective third temperature derivatives of elastic constants: (N/(m^2* (℃)^3))

$C^{(3)}_{pq}$						
p \ q	1	2	3	4	5	6
1	-38.145	-58.38811	122.9609	28.87819	0	0
2	-58.38811	56.60685	29.32932	22.58347	0	0
3	122.9609	29.32932	-125.0159	-52.43548	0	0
4	28.87819	22.58347	-52.43548	17.79152	0	0
5	0	0	0	0	44.33196	-29.4325
6	0	0	0	0	-29.4325	-120.624

Third-order elastic constants: (10^{10} N/m^2)

p =1	C_{pqr}					
q \ r	1	2	3	4	5	6
1	-21	1.975609	-35.27561	-15.40776	0	0
2	1.975609	-40.75605	-14.72592	1.081501	0	0
3	-35.27561	-14.72592	-42.09211	3.506117	0	0
4	-15.40776	1.081501	3.506117	1.274081	0	0
5	0	0	0	0	-22.19642	8.490682
6	0	0	0	0	8.490682	-3.578581

p =2	C_{pqr}					
q \ r	1	2	3	4	5	6
1	1.975609	-40.75605	-14.72592	1.081501	0	0
2	-40.75605	-57.68343	-45.97307	-0.515213	0	0
3	-14.72592	-45.97307	22.94787	8.548442	0	0
4	1.081501	-0.515213	8.548442	-16.45884	0	0
5	0	0	0	0	-9.363171	25.88292
6	0	0	0	0	25.88292	-17.03574

p =3	C_{pqr}					
q \ r	**1**	**2**	**3**	**4**	**5**	**6**
1	-35.27561	-14.72592	-42.09211	3.506117	0	0
2	-14.72592	-45.97307	22.94787	8.548442	0	0
3	-42.09211	22.94787	-77.94096	20.74527	0	0
4	3.506117	8.548442	20.74527	-7.566363	0	0
5	0	0	0	0	4.105421	-2.042817
6	0	0	0	0	-2.042817	19.61849

p =4	C_{pqr}					
q \ *r*	**1**	**2**	**3**	**4**	**5**	**6**
1	-15.40776	1.081501	3.506117	1.274081	0	0
2	1.081501	-0.515213	8.548442	-16.45884	0	0
3	3.506117	8.548442	20.74527	-7.566363	0	0
4	1.274081	-16.45884	-7.566363	-8.136764	0	0
5	0	0	0	0	-7.820395	0.877658
6	0	0	0	0	0.877658	-1.394659

p =5	C_{pqr}					
q \ r	**1**	**2**	**3**	**4**	**5**	**6**
1	0	0	0	0	-22.19642	8.490682
2	0	0	0	0	-9.363171	25.88292
3	0	0	0	0	4.105421	-2.042817
4	0	0	0	0	-7.820395	0.877658
5	-22.19642	-9.363171	4.105421	-7.820395	0	0
6	8.490682	25.88292	-2.042817	0.877658	0	0

p =6	C_{pqr}					
q \ r	**1**	**2**	**3**	**4**	**5**	**6**
1	0	0	0	0	8.490682	-3.578581
2	0	0	0	0	25.88292	-17.03574
3	0	0	0	0	-2.042817	19.61849
4	0	0	0	0	0.877658	-1.394659
5	8.490682	25.88292	-2.042817	0.877658	0	0
6	-3.578581	-17.03574	19.61849	-1.394659	0	0

Piezoelectric constants: (10^{-2} C/m^2)

e_{ij}						
i \ j	**1**	**2**	**3**	**4**	**5**	**6**
1	17.1	-3.33265	-13.76735	-7.900775	0	0
2	0	0	0	0	-6.7163	-9.37378
3	0	0	0	0	-7.72622	-10.7833

First temperature derivatives of piezoelectric constants: (10^{-6} C/(m^2* ℃))

$e^{(1)}_{ij}$						
i \ j	**1**	**2**	**3**	**4**	**5**	**6**
1	-1.37002	-2.503952	3.873972	0.243562	0	0
2	0	0	0	0	-0.666281	2.136489
3	0	0	0	0	-0.766468	2.457749

Second temperature derivatives of piezoelectric constants: (10^{-10} C/(m^2*(℃)^2))

$e^{(2)}_{ij}$						
i \ j	**1**	**2**	**3**	**4**	**5**	**6**
1	-7.48887	-22.52415	30.01302	0.089424	0	0
2	0	0	0	0	-7.48297	16.09704
3	0	0	0	0	-8.608173	18.51753

Third temperature derivatives of piezoelectric constants: (10^{-12} C/(m^2*(℃)^3))

$e^{(3)}_{ij}$						
i \ j	**1**	**2**	**3**	**4**	**5**	**6**
1	1.955179	3.805179	-5.760358	-0.315022	0	0
2	0	0	0	0	1.051588	-3.164892
3	0	0	0	0	1.209713	-3.640792

Dielectric permittivity: (10^{-12} C/(V*m))

ε_{ip}			
i \ p	**1**	**2**	**3**
1	39.215	0	0
2	0	40.25336	-0.902629
3	0	-0.902629	39.99964

First temperature derivatives of dielectric permittivity: (10^{-15} C/(V*m* ℃))

$\varepsilon^{(1)}_{ip}$			
i \ p	**1**	**2**	**3**
1	1.5902	0	0
2	0	3.795086	-1.916678
3	0	-1.916678	3.256344

Second temperature derivatives of dielectric permittivity: (10^{-18} C/(V*m*(℃)^2))

$\varepsilon^{(2)}_{ip}$			
i \ p	**1**	**2**	**3**
1	5.37723	0	0
2	0	2.422358	2.568631
3	0	2.568631	3.144353

Third temperature derivatives of dielectric permittivity: (10^{-21} C/(V*m*(℃)^3))

$\varepsilon^{(3)}_{ip}$			
i \ p	**1**	**2**	**3**
1	5.105736	0	0
2	0	-3.060245	7.098579
3	0	7.098579	-1.064964

First-order thermal expansion coefficients: (10^{-6} 1/ ℃)

$\alpha^{(1)}_{ij}$			
i \ j	**1**	**2**	**3**
1	13.71	0	0
2	0	10.16148	3.084685
3	0	3.084685	11.02852

Second-order thermal expansion coefficients: (10^{-9} 1/(℃)^2)

$\alpha^{(2)}_{ij}$			
i \ j	**1**	**2**	**3**
1	6.5	0	0
2	0	4.449488	1.782483
3	0	1.782483	4.950512

Third-order thermal expansion coefficients: (10^{-12} 1/(℃)^3)

$\alpha^{(3)}_{ij}$			
i \ j	**1**	**2**	**3**
1	-1.9	0	0
2	0	-1.672165	-0.198053
3	0	-0.198053	-1.727835

B4. *SC*-Cut Quartz

SC-cut of quartz is obtained by rotating *Y*-cut of quartz (YX*wl*) 21.9˚/ 33.9˚. (IRE 1949 standard)

Second-order elastic constants: (10^{10} N/m^2)

C_{pq}						
p \ q	1	2	3	4	5	6
1	8.674	0.168975	1.720025	-0.050249	-1.354848	-0.91042
2	0.168975	11.57169	-0.387834	0.88862	0.090451	1.881621
3	1.720025	-0.387834	10.97998	0.337021	1.264397	-0.971201
4	-0.050249	0.88862	0.337021	4.215165	-0.971201	0.090451
5	-1.354848	0.090451	1.264397	-0.971201	5.914577	0.557584
6	-0.91042	1.881621	-0.971201	0.090451	0.557584	3.867423

Viscosity constants: (10^{-3} N-sec/m^2)

n_{pq}						
p \ q	1	2	3	4	5	6
1	1.37	0.727588	0.712411	-0.007703	0.007564	0.005083
2	0.727588	1.350791	0.597855	-0.047856	-0.000505	-0.010505
3	0.712411	0.597855	1.203497	-0.143501	-0.007059	0.005422
4	-0.007703	-0.047856	-0.143501	0.247855	0.005422	-0.000505
5	0.007564	-0.000505	-0.007059	0.005422	0.343746	0.020072
6	0.005083	-0.010505	0.005422	-0.000505	0.020072	0.336253

First temperature derivatives of elastic constants: (10^6 N/(m^2* ℃))

$C^{(1)}_{pq}$						
p \ q	1	2	3	4	5	6
1	1.5976	-6.226066	-4.524034	3.083802	0.693499	0.466012
2	-6.226066	-5.906951	2.430031	-3.651665	-0.046298	0.963135
3	-4.524034	2.430031	-8.27761	-0.251347	-0.6472	0.497123
4	3.083802	-3.651665	-0.251347	-0.749669	0.497123	-0.04629
5	0.693499	-0.046298	-0.6472	0.497123	-2.475668	-4.696381
6	0.466012	0.963135	0.497123	-0.04629	-4.696381	2.172368

Effective second temperature derivatives of elastic constants: (10^3 N/(m^2* (℃)^2))

$C^{(2)}_{pq}$						
p \ *q*	**1**	**2**	**3**	**4**	**5**	**6**
1	-12.989	-28.41315	-25.51385	8.219035	3.241424	2.178146
2	-28.41315	-41.21203	5.343709	-11.12288	-0.216401	-4.501708
3	-25.51385	5.343709	-40.91139	6.824447	-3.025022	2.323562
4	8.219035	-11.12288	6.824447	-2.355291	2.323562	-0.216401
5	3.241424	-0.216401	-3.025022	2.323562	-16.45	-16.7267
6	2.178146	-4.501708	2.323562	-0.216401	-16.7267	1.011014

Effective third temperature derivatives of elastic constants: (N/(m^2* (℃)^3))

$C^{(3)}_{pq}$						
p \ *q*	**1**	**2**	**3**	**4**	**5**	**6**
1	-38.145	80.54	-15.9672	-24.82466	64.88521	43.60105
2	80.54	-80.02972	26.52935	16.04522	-4.331813	-90.11296
3	-15.9672	26.52935	17.22062	9.689945	-60.5534	46.51191
4	-24.82466	16.04522	9.689945	14.99155	46.51191	-4.331813
5	64.88521	-4.331813	-60.5534	46.51191	-64.14682	29.70412
6	43.60105	-90.11296	46.51191	-4.331813	29.70412	-12.14518

Third-order elastic constants: (10^{10} N/m^2)

p =1	C_{pqr}					
q \ *r*	**1**	**2**	**3**	**4**	**5**	**6**
1	-31.134	-22.62338	-0.542613	9.300966	-12.04792	-13.60865
2	-22.62338	-43.2447	-18.70427	-3.830494	-4.412174	8.356306
3	-0.542613	-18.70427	-41.78429	4.199624	3.146121	-3.694275
4	9.300966	-3.830494	4.199624	-2.70427	-0.695123	0.051034
5	-12.04792	-4.412174	3.146121	-0.695123	-8.459917	-12.89371
6	-13.60865	8.356306	-3.694275	0.051034	-12.89371	-7.181081

p =2	C_{pqr}					
q \ *r*	**1**	**2**	**3**	**4**	**5**	**6**
1	-22.62338	-43.24117	-18.70427	-3.830494	-4.412174	8.356306
2	-43.24117	-58.58039	7.84314	-18.79839	-17.58501	0.008722
3	-18.70427	7.84314	-30.02743	-7.918034	22.88604	10.1255
4	-3.830494	-18.79839	-7.918034	-10.91781	-11.1316	-7.76404
5	-4.412174	-17.58501	22.88604	-11.1316	3.782885	-3.682876
6	8.356306	0.008722	10.1255	-7.76404	-3.682876	-4.287647

p =3			C_{pqr}			
q \ **r**	**1**	**2**	**3**	**4**	**5**	**6**
1	-0.542613	-18.70427	-41.78429	4.199624	3.146121	-3.694275
2	-18.70427	7.84314	-30.02743	-7.918034	22.88604	10.1255
3	-41.78429	-30.02743	-69.43275	-4.4771	-13.60705	-15.97513
4	4.199624	-7.918034	-4.4771	-12.26647	2.282819	8.601863
5	3.146121	22.88604	-13.60705	2.282819	-14.24355	-14.09813
6	-3.694275	10.1255	-15.97513	8.601863	-14.09813	1.939314

p =4			C_{pqr}			
q \ *r*	**1**	**2**	**3**	**4**	**5**	**6**
1	9.300966	-3.830494	4.199624	-2.70427	-0.695123	0.051034
2	-3.830494	-18.79839	-7.918034	-10.91781	-11.1316	-7.76404
3	4.199624	-7.918034	-4.4771	-12.26647	2.282819	8.601863
4	-2.70427	-10.91781	-12.26647	6.987146	2.158604	-3.802761
5	-0.695123	-11.1316	2.282819	2.158604	6.200746	-1.3889
6	0.051034	-7.76404	8.601863	-3.802761	-1.3889	7.768445

p =5			C_{pqr}			
q \ *r*	**1**	**2**	**3**	**4**	**5**	**6**
1	-12.04792	-4.412174	3.146121	-0.695123	-8.459917	-12.89371
2	-4.412174	-17.58501	22.88604	-11.1316	3.782885	-3.682876
3	3.146121	22.88604	-13.60705	2.282819	-14.24355	-14.09813
4	-0.695123	-11.1316	2.282819	2.158604	6.200746	-1.3889
5	-8.459917	3.782885	-14.24355	6.200746	14.64885	10.03354
6	-12.89371	-3.682876	-14.09813	-1.3889	10.03354	4.812536

p =6			C_{pqr}			
q \ **r**	**1**	**2**	**3**	**4**	**5**	**6**
1	-13.60865	8.356306	-3.694275	0.051034	-12.89371	-7.181081
2	8.356306	0.008722	10.1255	-7.76404	-3.682876	-4.287647
3	-3.694275	10.1255	-15.97513	8.601863	-14.09813	1.939314
4	0.051034	-7.76404	8.601863	-3.802761	-1.3889	7.768445
5	-12.89371	-3.682876	-14.09813	-1.3889	10.03354	4.812536
6	-7.181081	-4.287647	1.939314	7.768445	4.812536	8.556751

Piezoelectric constants: (10^{-2} C/m^2)

e_{ij}						
i \ j	1	2	3	4	5	6
1	7.036896	-8.613377	1.576481	1.720949	8.692455	-12.93574
2	-12.93574	8.911694	4.024044	-5.98841	6.059467	-2.965103
3	8.692455	-5.98841	-2.704046	4.024044	-4.071793	1.992467

First temperature derivatives of piezoelectric constants: (10^{-6} C/(m^2* ℃))

$e^{(1)}_{ij}$						
i \ j	1	2	3	4	5	6
1	-0.563782	3.280849	-2.717066	0.919391	-0.696423	1.036387
2	1.036387	-0.713988	-0.322398	0.47978	-2.413203	-1.057822
3	-0.696423	0.47978	0.216643	-0.322398	1.621605	0.710827

Second temperature derivatives of piezoelectric constants: (10^{-10} C/(m^2*(℃)^2))

$e^{(2)}_{ij}$						
i \ j	1	2	3	4	5	6
1	-3.081778	26.1962	-23.11442	8.397386	-3.806823	5.66515
2	5.66515	-3.902837	-1.762313	2.622598	-19.33894	-9.91345
3	-3.806823	2.622598	1.184225	-1.762313	12.99523	6.661562

Third temperature derivatives of piezoelectric constants: (10^{-12} C/(m^2*(℃)^3))

$e^{(3)}_{ij}$						
i \ j	1	2	3	4	5	6
1	0.804584	-4.898831	4.094247	-1.400502	0.993877	-1.479046
2	-1.479046	1.018945	0.460101	-0.684702	3.605147	1.617974
3	0.993877	-0.684702	-0.309175	0.460101	-2.422558	-1.087233

Dielectric permittivity: (10^{-12} C/(V*m))

ε_{ip}			
i \ p	1	2	3
1	39.215	0	0
2	0	39.7821	0.843931
3	0	0.843931	40.4709

First temperature derivatives of dielectric permittivity: (10^{-15} C/(V*m* ℃))

$\varepsilon^{(1)}_{ip}$			
i \ p	**1**	**2**	**3**
1	1.5902	0	0
2	0	2.7944	1.79204
3	0	1.79204	4.25703

Second temperature derivatives of dielectric permittivity: (10^{-18} C/(V*m*(℃)^2))

$\varepsilon^{(2)}_{ip}$			
i \ p	**1**	**2**	**3**
1	5.37723	0	0
2	0	3.76343	-2.40159
3	0	-2.40159	1.80328

Third temperature derivatives of dielectric permittivity: (10^{-21} C/(V*m*(℃)^3))

$\varepsilon^{(3)}_{ip}$			
i \ p	**1**	**2**	**3**
1	5.10574	0	0
2	0	0.645887	-6.63696
3	0	-6.63696	-4.7711

First-order thermal expansion coefficients: (10^{-6} 1/ ℃)

$\alpha^{(1)}_{ij}$			
i \ j	**1**	**2**	**3**
1	13.71	0	0
2	0	11.77197	-2.884087
3	0	-2.884087	9.418026

Second-order thermal expansion coefficients: (10^{-9} 1/(℃)^2)

$\alpha^{(2)}_{ij}$			
i \ j	**1**	**2**	**3**
1	6.5	0	0
2	0	5.380113	-1.666567
3	0	-1.666567	4.019887

Third-order thermal expansion coefficients: (10^{-12} 1/(℃)^3)

$\alpha^{(3)}_{ij}$			
i \ *j*	**1**	**2**	**3**
1	-1.9	0	0
2	0	-1.775568	0.185174
3	0	0.185174	-1.624432

Appendix C. Electrodes Material Properties

C1. Gold

The mass density of gold is 19300 ${kg}/{m^3}$.

Values of material constants for gold have been determined by J.Neighbours and G. Alers [77], Y. Chang and L. Himmel [78], Y. Hiki and A. Granato [79], and F. Nix and D. MacNair [80].

Second-order elastic constants: (10^{10} N/m^2)

C_{pq}						
p \ q	**1**	**2**	**3**	**4**	**5**	**6**
1	19.25	16.311	16.311	0	0	0
2	16.311	19.25	16.311	0	0	0
3	16.311	16.311	19.25	0	0	0
4	0	0	0	4.2073	0	0
5	0	0	0	0	4.2073	0
6	0	0	0	0	0	4.2073

Viscosity constants: (10^{-8} N-sec/m^2) [81]**.**

n_{pq}						
p \ q	**1**	**2**	**3**	**4**	**5**	**6**
1	12.39	8.925	8.925	0	0	0
2	8.925	12.39	8.925	0	0	0
3	8.925	8.925	12.39	0	0	0
4	0	0	0	1.7	0	0
5	0	0	0	0	1.7	0
6	0	0	0	0	0	1.7

First temperature coefficients of elastic constants: (10^7 N/m^2/ ℃)

$C^{(1)}_{pq}$						
p \ q	**1**	**2**	**3**	**4**	**5**	**6**
1	-3.4354	-2.6674	-2.6674	0	0	0
2	-2.6674	-3.4354	-2.6674	0	0	0
3	-2.6674	-2.6674	-3.4354	0	0	0
4	0	0	0	-1.0991	0	0
5	0	0	0	0	-1.0991	0
6	0	0	0	0	0	-1.0991

Second temperature coefficients of elastic constants: (10^3 N/m^2/ (℃)^2)

$C^{(2)}_{pq}$						
p \ q	**1**	**2**	**3**	**4**	**5**	**6**
1	0.63567	-1.4816	-1.4816	0	0	0
2	-1.4816	0.63567	-1.4816	0	0	0
3	-1.4816	-1.4816	0.63567	0	0	0
4	0	0	0	1.9374	0	0
5	0	0	0	0	1.9374	0
6	0	0	0	0	0	1.9374

Third temperature coefficients of elastic constants: (N/m^2/ (℃)^3)

$C^{(3)}_{pq}$						
p \ q	**1**	**2**	**3**	**4**	**5**	**6**
1	-6.8639	20.282	20.282	0	0	0
2	20.282	-6.8639	20.282	0	0	0
3	20.282	20.282	-6.8639	0	0	0
4	0	0	0	-24.268	0	0
5	0	0	0	0	-24.268	0
6	0	0	0	0	0	-24.268

Third-order elastic constants: (10^{11} N/m^2)

p =1	C_{pqr}					
q \ r	**1**	**2**	**3**	**4**	**5**	**6**
1	-17.29	-9.22	-9.22	0	0	0
2	-9.22	-9.22	-2.33	0	0	0
3	-9.22	-2.33	-9.22	0	0	0
4	0	0	0	-0.13	0	0
5	0	0	0	0	-6.48	0
6	0	0	0	0	0	-6.48

p =2	C_{pqr}					
q \ r	**1**	**2**	**3**	**4**	**5**	**6**
1	-9.22	-9.22	-2.33	0	0	0
2	-9.22	-17.29	-9.22	0	0	0
3	-2.33	-9.22	-9.22	0	0	0
4	0	0	0	-6.48	0	0
5	0	0	0	0	-0.13	0
6	0	0	0	0	0	6.48

p =3	C_{pqr}					
q \ r	**1**	**2**	**3**	**4**	**5**	**6**
1	-9.22	-2.33	-9.22	0	0	0
2	-2.33	-9.22	-9.22	0	0	0
3	-9.22	-9.22	-17.29	0	0	0
4	0	0	0	-6.48	0	0
5	0	0	0	0	-6.48	0
6	0	0	0	0	0	-0.13

p =4	C_{pqr}					
q \ r	**1**	**2**	**3**	**4**	**5**	**6**
1	0	0	0	-0.13	0	0
2	0	0	0	-6.48	0	0
3	0	0	0	-6.48	0	0
4	-0.13	-6.48	-6.48	0	0	0
5	0	0	0	0	0	-0.12
6	0	0	0	0	-0.12	0

p =5	C_{pqr}					
q \ r	**1**	**2**	**3**	**4**	**5**	**6**
1	0	0	0	0	-6.48	0
2	0	0	0	0	-0.13	0
3	0	0	0	0	-6.48	0
4	0	0	0	0	0	-0.12
5	-6.48	-0.13	-6.48	0	0	0
6	0	0	0	-0.12	0	0

p =6	C_{pqr}					
q \ r	1	2	3	4	5	6
1	0	0	0	0	0	-6.48
2	0	0	0	0	0	-6.48
3	0	0	0	0	0	-0.13
4	0	0	0	0	-0.12	0
5	0	0	0	-0.12	0	0
6	-6.48	-6.48	-0.13	0	0	0

First-order thermal expansion coefficients: (10^{-5} 1/ ℃)

$\alpha^{(1)}_{ij}$			
i \ j	1	2	3
1	1.4027	0	0
2	0	1.4027	0
3	0	0	1.4027

Second-order thermal expansion coefficients: (10^{-9} 1/(℃)^2)

$\alpha^{(2)}_{ij}$			
i \ j	1	2	3
1	5.1324	0	0
2	0	5.1324	0
3	0	0	5.1324

Third-order thermal expansion coefficients: (10^{-12} 1/(℃)^3)

$\alpha^{(3)}_{ij}$			
i \ j	1	2	3
1	-1.3196	0	0
2	0	-1.3196	0
3	0	0	-1.3196

C2. Aluminum

The mass density of gold is 2700 $^{kg}/_{m^3}$.

Values of material constants for aluminum have been determined by R. Hearmon [82], J. Thomas [83], and F. Nix and D. MacNair [80].

Second-order elastic constants: (10^{10} N/m^2)

C_{pq}						
p \ q	**1**	**2**	**3**	**4**	**5**	**6**
1	11.218	6.5697	6.5697	0	0	0
2	6.5697	11.218	6.5697	0	0	0
3	6.5697	6.5697	11.218	0	0	0
4	0	0	0	2.7836	0	0
5	0	0	0	0	2.7836	0
6	0	0	0	0	0	2.7836

Viscosity constants: (10^{-8} N-sec/m^2) [81]**.**

n_{pq}						
p \ q	**1**	**2**	**3**	**4**	**5**	**6**
1	9.852	4.853	4.853	0	0	0
2	4.853	9.852	4.853	0	0	0
3	4.853	4.853	9.852	0	0	0
4	0	0	0	2.55	0	0
5	0	0	0	0	2.55	0
6	0	0	0	0	0	2.55

First temperature coefficients of elastic constants: (10^7 N/m^2/ ℃)

$C^{(1)}_{pq}$						
p \ q	**1**	**2**	**3**	**4**	**5**	**6**
1	-5.5568	-2.771	-2.771	0	0	0
2	-2.771	-5.5568	-2.771	0	0	0
3	-2.771	-2.771	-5.5568	0	0	0
4	0	0	0	-1.3131	0	0
5	0	0	0	0	-1.3131	0
6	0	0	0	0	0	-1.3131

Second temperature coefficients of elastic constants: (10^3 N/m^2/ (℃)^2)

$C^{(2)}_{pq}$						
p \ q	**1**	**2**	**3**	**4**	**5**	**6**
1	-41.252	-24.93	-24.93	0	0	0
2	-24.93	-41.252	-24.93	0	0	0
3	-24.93	-24.93	-41.252	0	0	0
4	0	0	0	-5.5849	0	0
5	0	0	0	0	-5.5849	0
6	0	0	0	0	0	-5.5849

Third temperature coefficients of elastic constants: (N/m^2/ (℃)^3)

$C^{(3)}_{pq}$						
p \ q	**1**	**2**	**3**	**4**	**5**	**6**
1	27.052	11.467	11.467	0	0	0
2	11.467	27.052	11.467	0	0	0
3	11.467	11.467	27.052	0	0	0
4	0	0	0	3.7558	0	0
5	0	0	0	0	3.7558	0
6	0	0	0	0	0	3.7558

Third-order elastic constants: (10^{11} N/m^2)

p =1	C_{pqr}					
q \ r	**1**	**2**	**3**	**4**	**5**	**6**
1	-10.8	-3.15	-3.15	0	0	0
2	-3.15	-3.15	0.36	0	0	0
3	-3.15	0.36	-3.15	0	0	0
4	0	0	0	-0.23	0	0
5	0	0	0	0	-3.4	0
6	0	0	0	0	0	-3.4

p =2	C_{pqr}					
q \ r	**1**	**2**	**3**	**4**	**5**	**6**
1	-3.15	-3.15	0.36	0	0	0
2	-3.15	-10.8	-3.15	0	0	0
3	0.36	-3.15	-3.15	0	0	0
4	0	0	0	-3.4	0	0
5	0	0	0	0	-0.23	0
6	0	0	0	0	0	-3.4

p =3	C_{pqr}					
q \ r	**1**	**2**	**3**	**4**	**5**	**6**
1	-3.15	0.36	-3.15	0	0	0
2	0.36	-3.15	-3.15	0	0	0
3	-3.15	-3.15	-10.8	0	0	0
4	0	0	0	-3.4	0	0
5	0	0	0	0	-3.4	0
6	0	0	0	0	0	-0.23

p =4	C_{pqr}					
q \ *r*	**1**	**2**	**3**	**4**	**5**	**6**
1	0	0	0	-0.23	0	0
2	0	0	0	-3.4	0	0
3	0	0	0	-3.4	0	0
4	-0.23	-3.4	-3.4	0	0	0
5	0	0	0	0	0	-0.3
6	0	0	0	0	-0.3	0

p =5	C_{pqr}					
q \ *r*	**1**	**2**	**3**	**4**	**5**	**6**
1	0	0	0	0	-3.4	0
2	0	0	0	0	-0.23	0
3	0	0	0	0	-3.4	0
4	0	0	0	0	0	-0.3
5	-3.4	-0.23	-3.4	0	0	0
6	0	0	0	-0.3	0	0

p =6	C_{pqr}					
q \ r	**1**	**2**	**3**	**4**	**5**	**6**
1	0	0	0	0	0	-3.4
2	0	0	0	0	0	-3.4
3	0	0	0	0	0	-0.23
4	0	0	0	0	-0.3	0
5	0	0	0	-0.3	0	0
6	-3.4	-3.4	-0.23	0	0	0

First-order thermal expansion coefficients: (10^{-5} 1/℃)

	$\alpha^{(1)}_{ij}$		
i \ *j*	**1**	**2**	**3**
1	2.314	0	0
2	0	2.314	0
3	0	0	2.314

Second-order thermal expansion coefficients: (10^{-9} 1/(℃)^2)

$\alpha^{(2)}_{ij}$			
i \ *j*	**1**	**2**	**3**
1	25.2	0	0
2	0	25.2	0
3	0	0	25.2

Third-order thermal expansion coefficients: (10^{-12} 1/(℃)^3)

$\alpha^{(3)}_{ij}$			
i \ *j*	**1**	**2**	**3**
1	-30.87	0	0
2	0	-30.87	0
3	0	0	-30.87

C3. Chromium

The mass density of gold is 7190 $^{kg}/_{m^3}$.

Values of material constants for chromium have been determined by D. Bolef and J. Klerk [84], S. Palmer and E. Lee [85], and S. Mathur and Y. Sharma [86].

Second-order elastic constants: (10^{10} N/m^2)

C_{pq}						
p \ q	**1**	**2**	**3**	**4**	**5**	**6**
1	35.554	7.3753	7.3753	0	0	0
2	7.3753	35.554	7.3753	0	0	0
3	7.3753	7.3753	35.554	0	0	0
4	0	0	0	10.083	0	0
5	0	0	0	0	10.083	0
6	0	0	0	0	0	10.083

First temperature coefficients of elastic constants: (10^7 N/m^2/ ℃)

$C^{(1)}_{pq}$						
p \ q	**1**	**2**	**3**	**4**	**5**	**6**
1	-5.0244	0.1859	0.1859	0	0	0
2	0.1859	-5.0244	0.1859	0	0	0
3	0.1859	0.1859	-5.0244	0	0	0
4	0	0	0	-0.81286	0	0
5	0	0	0	0	-0.81286	0
6	0	0	0	0	0	-0.81286

Second temperature coefficients of elastic constants: (10^3 N/m^2/ (℃)^2)

$C^{(2)}_{pq}$						
p \ q	**1**	**2**	**3**	**4**	**5**	**6**
1	1301.7	1321.6	1321.6	0	0	0
2	1321.6	1301.7	1321.6	0	0	0
3	1321.6	1321.6	1301.7	0	0	0
4	0	0	0	7.6702	0	0
5	0	0	0	0	7.6702	0
6	0	0	0	0	0	7.6702

Third temperature coefficients of elastic constants: (10^2 N/m^2/ (℃)^3)

$C^{(3)}_{pq}$						
p \ q	**1**	**2**	**3**	**4**	**5**	**6**
1	-118.84	-105.48	-105.48	0	0	0
2	-105.48	-118.84	-105.48	0	0	0
3	-105.48	-105.48	-118.84	0	0	0
4	0	0	0	-2.7236	0	0
5	0	0	0	0	-2.7236	0
6	0	0	0	0	0	-2.7236

Third-order elastic constants: (10^{11} N/m^2)

p =1	C_{pqr}					
q \ r	**1**	**2**	**3**	**4**	**5**	**6**
1	-8.036	-1.399	-1.399	0	0	0
2	-1.399	-1.399	-1.836	0	0	0
3	-1.399	-1.836	-1.399	0	0	0
4	0	0	0	-1.836	0	0
5	0	0	0	0	-1.399	0
6	0	0	0	0	0	-1.399

p =2	C_{pqr}					
q \ r	**1**	**2**	**3**	**4**	**5**	**6**
1	-1.399	-1.399	-1.836	0	0	0
2	-1.399	-8.036	-1.399	0	0	0
3	-1.836	-1.399	-1.399	0	0	0
4	0	0	0	-1.399	0	0
5	0	0	0	0	-1.836	0
6	0	0	0	0	0	-1.399

p =3	C_{pqr}					
q \ r	**1**	**2**	**3**	**4**	**5**	**6**
1	-1.399	-1.836	-1.399	0	0	0
2	-1.836	-1.399	-1.399	0	0	0
3	-1.399	-1.399	-8.036	0	0	0
4	0	0	0	-1.399	0	0
5	0	0	0	0	-1.399	0
6	0	0	0	0	0	-1.836

p =4	C_{pqr}					
q \ r	1	2	3	4	5	6
1	0	0	0	-1.836	0	0
2	0	0	0	-1.399	0	0
3	0	0	0	-1.399	0	0
4	-1.836	-1.399	-1.399	0	0	0
5	0	0	0	0	0	-1.836
6	0	0	0	0	-1.836	0

p =5	C_{pqr}					
q \ r	1	2	3	4	5	6
1	0	0	0	0	-1.399	0
2	0	0	0	0	-1.836	0
3	0	0	0	0	-1.399	0
4	0	0	0	0	0	-1.836
5	-1.399	-1.836	-1.399	0	0	0
6	0	0	0	-1.836	0	0

p =6	C_{pqr}					
q \ r	1	2	3	4	5	6
1	0	0	0	0	0	-1.399
2	0	0	0	0	0	-1.399
3	0	0	0	0	0	-1.836
4	0	0	0	0	-1.836	0
5	0	0	0	-1.836	0	0
6	-1.399	-1.399	-1.836	0	0	0

First-order thermal expansion coefficients: (10^{-5} 1/ ℃)

	$\alpha^{(1)}_{ij}$		
i \ j	1	2	3
1	0.8039	0	0
2	0	0.8039	0
3	0	0	0.8039

Second-order thermal expansion coefficients: (10^{-9} 1/(℃)^2)

	$\alpha^{(2)}_{ij}$		
i \ j	1	2	3
1	18.49	0	0
2	0	18.49	0
3	0	0	18.49

Third-order thermal expansion coefficients: (10^{-12} 1/(℃)^3)

$\alpha^{(3)}_{ij}$			
i \ ***j***	**1**	**2**	**3**
1	6.5	0	0
2	0	6.5	0
3	0	0	6.5

C4. Titanium

The mass density of gold is 4506 $^{kg}/_{m^3}$.

Values of material constants for titanium have been determined by E. Fisher and C. Renken [87], R. Rao and C. Menon [88], and P. Hidnert [89].

Second-order elastic constants: (10^{10} N/m^2)

C_{pq}						
p \ q	**1**	**2**	**3**	**4**	**5**	**6**
1	16.24	9.194	6.9	0	0	0
2	9.194	16.24	6.9	0	0	0
3	6.9	6.9	18.06	0	0	0
4	0	0	0	4.67	0	0
5	0	0	0	0	4.67	0
6	0	0	0	0	0	3.523

First temperature coefficients of elastic constants: (10^7 N/m^2/ ℃)

$C^{(1)}_{pq}$						
p \ q	**1**	**2**	**3**	**4**	**5**	**6**
1	-6.04	2.204	0.523	0	0	0
2	2.204	-6.04	0.523	0	0	0
3	0.523	0.523	-4.24	0	0	0
4	0	0	0	-1.917	0	0
5	0	0	0	0	-1.917	0
6	0	0	0	0	0	-4.122

Second temperature coefficients of elastic constants: (10^3 N/m^2/ (℃)^2)

$C^{(2)}_{pq}$						
p \ q	**1**	**2**	**3**	**4**	**5**	**6**
1	-8.973	-32.33	7.23	0	0	0
2	-32.33	-8.973	7.23	0	0	0
3	7.23	7.23	-10.73	0	0	0
4	0	0	0	-1.74	0	0
5	0	0	0	0	-1.74	0
6	0	0	0	0	0	11.68

Third temperature coefficients of elastic constants: (N/m^2/ (℃)^3)

$C^{(3)}_{pq}$						
p \ *q*	**1**	**2**	**3**	**4**	**5**	**6**
1	197.6	50.08	-134	0	0	0
2	50.08	197.6	-134	0	0	0
3	-134	-134	81.22	0	0	0
4	0	0	0	63.62	0	0
5	0	0	0	0	63.62	0
6	0	0	0	0	0	73.77

Third-order elastic constants: (10^{11} N/m^2)

***p* =1**	C_{pqr}					
q \ *r*	**1**	**2**	**3**	**4**	**5**	**6**
1	-16.66	-8.87	1.03	0	0	0
2	-8.87	-3.43	-1.93	0	0	0
3	1.03	-1.93	-4.36	0	0	0
4	0	0	0	-1.67	0	0
5	0	0	0	0	0.78	0
6	0	0	0	0	0	-6.0275

***p* =2**	C_{pqr}					
q \ *r*	**1**	**2**	**3**	**4**	**5**	**6**
1	-8.87	-3.43	-1.93	0	0	0
2	-3.43	-22.1	1.03	0	0	0
3	-1.93	1.03	-4.36	0	0	0
4	0	0	0	0.78	0	0
5	0	0	0	0	-1.67	0
6	0	0	0	0	0	-0.5875

***p* =3**	C_{pqr}					
q \ **r**	**1**	**2**	**3**	**4**	**5**	**6**
1	1.03	-1.93	-4.36	0	0	0
2	-1.93	1.03	-4.36	0	0	0
3	-4.36	-4.36	-15.14	0	0	0
4	0	0	0	-4.36	0	0
5	0	0	0	0	-4.36	0
6	0	0	0	0	0	1.48

p =4	C_{pqr}					
q \ r	1	2	3	4	5	6
1	0	0	0	-1.67	0	0
2	0	0	0	0.78	0	0
3	0	0	0	-4.36	0	0
4	-1.67	0.78	-4.36	0	0	0
5	0	0	0	0	0	1.225
6	0	0	0	0	1.225	0

p =5	C_{pqr}					
q \ r	1	2	3	4	5	6
1	0	0	0	0	0.78	0
2	0	0	0	0	-1.67	0
3	0	0	0	0	-4.36	0
4	0	0	0	0	0	1.225
5	0.78	-1.67	-4.36	0	0	0
6	0	0	0	1.225	0	0

p =6	C_{pqr}					
q \ r	1	2	3	4	5	6
1	0	0	0	0	0	-6.0275
2	0	0	0	0	0	-0.5875
3	0	0	0	0	0	1.48
4	0	0	0	0	1.225	0
5	0	0	0	1.225	0	0
6	-6.0275	-0.5875	1.48	0	0	0

First-order thermal expansion coefficients: (10^{-5} 1/ ℃)

	$\alpha^{(1)}_{ij}$		
i \ j	1	2	3
1	0.8591	0	0
2	0	0.8591	0
3	0	0	0.8591

Second-order thermal expansion coefficients: (10^{-9} 1/(℃)^2)

	$\alpha^{(2)}_{ij}$		
i \ j	1	2	3
1	11.09	0	0
2	0	11.09	0
3	0	0	11.09

Third-order thermal expansion coefficients: (10^{-12} 1/(℃)^3)

$\alpha^{(3)}_{ij}$			
i \ *j*	**1**	**2**	**3**
1	-33.29	0	0
2	0	-33.29	0
3	0	0	-33.29